FABRICATION OF SOLID SOLUTION TUNGSTEN-RHENIUM ALLOYS BY HIGH

ENERGY BALL MILLING AND SPARK PLASMA SINTERING

by

Cory C. Sparks

A thesis

submitted in partial fulfillment

of the requirements for the degree of

Master of Science in Materials Science and Engineering

Boise State University

December 2012

BOISE STATE UNIVERSITY GRADUATE COLLEGE

DEFENSE COMMITTEE AND FINAL READING APPROVALS

of the thesis submitted by

Cory C. Sparks

Thesis Title: Fabrication of Solid Solution Tungsten-Rhenium Alloys by High-Energy Ball Milling and Spark Plasma Sintering

Date of Final Oral Examination: 31 March 2012

The following individuals read and discussed the thesis submitted by student Cory C. Sparks, and they evaluated his presentation and response to questions during the final oral examination. They found that the student passed the final oral examination.

Darryl P. Butt, Ph.D.   Chair, Supervisory Committee

Megan E. Frary, Ph.D.   Member, Supervisory Committee

Indrajit Charit, Ph.D.   Member, Supervisory Committee

The final reading approval of the thesis was granted by Darryl P. Butt, Ph.D., Chair of the Supervisory Committee. The thesis was approved for the Graduate College by John R. Pelton, Ph.D., Dean of the Graduate College.

ACKNOWLEDGEMENTS

ABSTRACT

Tungsten-rhenium powders of varying compositions were fabricated by spark plasma sintering (SPS). In initial exploration of the parameter space, W-25 at% Re powders were blended and consolidated by SPS at 1500 to 1900°C with sintering dwell times of 0 to 60 minutes. In addition, the influence of milling was investigated. W-25 at% Re powders were high-energy ball milled at 200 to 400 rpm for 5 hours and consolidated at 1700°C with sintering dwell times of 0 to 60 minutes. The sample densities, grain sizes, porosities, contamination level, and hardness values were measured. The intermetallic content, specifically the fraction of σ-phase, of each sample was determined by scanning electron microscopy (SEM) in the backscatter mode and X-ray diffraction (XRD).

Processing parameters were optimized to yield high density and hardness values, with corresponding minimal grain growth, porosity, contamination, and minimal σ-phase content. The optimized process that was developed involved ball milling at 400 rpm for 30 hrs, followed by consolidation at 1800°C and hold times of 30 minutes. This process resulted in a complete solid solution between tungsten and rhenium, and no detectable σ-phase based on TEM/EDS characterization.

The optimized ball milling and sintering parameters were extended to W-Re compositions of W-3 at% Re, W-6 at% Re, W-10 at% Re, and these samples were similarly characterized. For each composition, W-Re solid solutions were produced with

no detectable σ-phase though the higher rhenium concentrations required longer hold

times. Decreasing the rhenium content in the alloys resulted in larger grains, decreased

hardness values, higher porosity, and lower densities.

TABLE OF CONTENTS

LIST OF TABLES

LIST OF FIGURES

xiv

xv

LIST OF ABBREVIATIONS

BSE – Backscatter electron

CAES – Center for Advanced Energy Studies

DBTT – Ductile to Brittle Transition Temperature

EBSD – Electron backscatter diffraction

EDS – Energy Dispersive Spectroscopy

FWHM – Full Width Half Maximum

HEBM – High Energy Ball Milling

HRTEM – High Resolution Transmission Electron Microscopy

LED – Light Emitting Diode

P/M – Powder Metallurgy

PSA – Particle Size Analyzer

PSD – Particle Size Distribution

SEM – Scanning Electron Microscope

SPS – Spark Plasma Sintering

STEM – Scanning Transmission Electron Microscope

TEM – Transmission Electron Microscope

XPS – X-Ray Photoelectron Spectroscopy

XRD – X-Ray Diffraction

LIST OF SYMBOLS

σ – W_2Re_3 intermetallic phase

χ – WRe_3 intermetallic phase

γ = surface energy

η = viscosity

ρ = theoretical density

δ = grain boundary width

Ω = atomic volume

CHAPTER ONE: INTRODUCTION

1.1 - Motivation for Research and Objectives

Sintering tungsten or tungsten-rhenium alloys typically requires very high temperatures and long hold times due to their high melting temperatures. Spark plasma sintering (SPS), on the other hand, is a powder metallurgical technique that has produced samples of superior quality at lower temperatures and hold times compared to traditional consolidation techniques such as hot pressing and pressureless sintering. The process is unique in its ability to use rapid temperature ramp rates while also applying uniaxial pressure to powders, consolidating samples to almost theoretical densities.

While previous work at Boise State has shown the SPS technique capable of sintering tungsten powders at low temperatures and short hold times, the consolidation of W-Re powders is complicated by issues of alloy homogenization. The tungsten-rhenium system is only partially miscible and has two intermetallic phases, σ and χ. Both of these phases are detrimental to the mechanical properties of the alloy and will form when localized concentrations of rhenium above the solubility limit are present in the tungsten matrix.

High energy ball milling is a well-known powder processing technique that has been reported to be effective at mechanically alloying powders. Employing high energy ball milling prior to sintering has the potential to minimize the temperature and time required for alloy homogenization and decrease the intermetallic content in the

microstructure. Unfortunately, extensive milling can also result in a high amount of contamination in the processed powders.

Consequently, the objectives of this research were to determine an optimized process for both ball milling and sintering to produce W-Re samples in the composition range 3 to 25 at% Re with little to no intermetallic phase, while maintaining acceptable grain size, density, and contamination levels. This was to be accomplished by assessing the effects of milling energies, sintering times, and temperature during SPS on the microstructure and the fraction of σ-phase. An additional objective of this study was to understand the effects of milling energy, using a high-energy planetary ball mill, on the morphology, homogeneity, and particle size of the tungsten-rhenium alloyed powders, and, subsequently, to assess the role that the particle characteristics play in obtaining a homogeneous alloy with desirable microstructure.

CHAPTER TWO: BACKGROUND INFORMATION

2.1 - W-Re Alloys

Tungsten has the highest melting temperature of all metals, high corrosion resistance, high thermal conductivity, high creep resistance, and the lowest vapor pressure of metals.[13; 35] With these properties, tungsten-based alloys are candidates for many high temperature applications such as structural materials, aerospace, friction stir-welding, nuclear reactor cladding, thermocouples, and thermionic emitters.[32; 36; 59] However, tungsten has a high ductile-to-brittle-transition temperature (DBTT) and its poor ductility at room temperature makes fabrication difficult.[41] These problems can be alleviated by alloying tungsten with rhenium.

First reported by Geach and Hughes, rhenium has been shown to be an ideal element to alloy with tungsten.[18] Rhenium has a melting point of 3177°C, the second highest of metals.[47] Alloying with rhenium can substantially lower tungsten's DBTT, while increasing its high temperature strength, corrosion resistance, creep resistance, ductility, fabricability, recrystallization temperature, and fracture toughness.[8; 9; 16; 18; 21; 30; 35; 48; 49] This increase in strength and plasticity is an oddity for solid solution alloying and is generally referred to as "the rhenium effect" and it also extends to alloying with Mo and Cr.[9] Research by Klopp *et al.* on tungsten's DBTT and hardness values can be seen in Figure 1 and the change to tungsten's creep resistance and high temperature strength can be seen in Figure 2 and Figure 3, respectively.[30; 33]
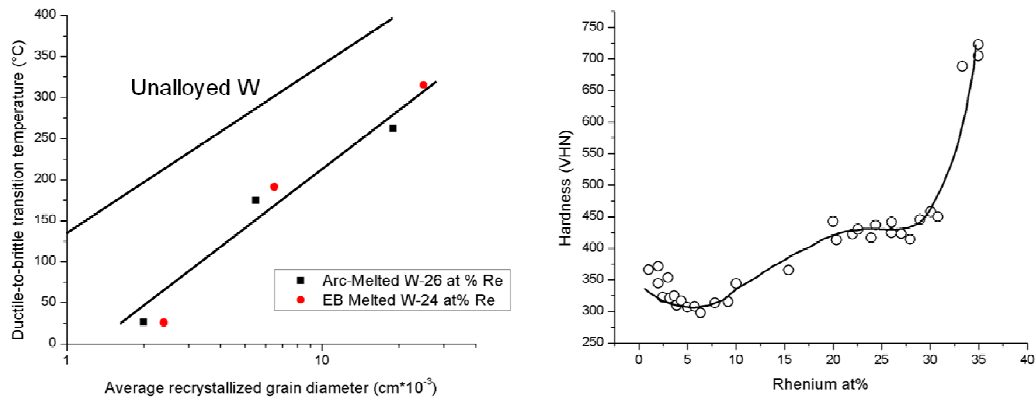
Figure 1. Plots of DBTT as a function of average recrystallized grain diameter for pure tungsten and W-24Re/W-26Re (left) and hardness (VHN) as a function of rhenium content (right). Adapted from Klopp.[30]
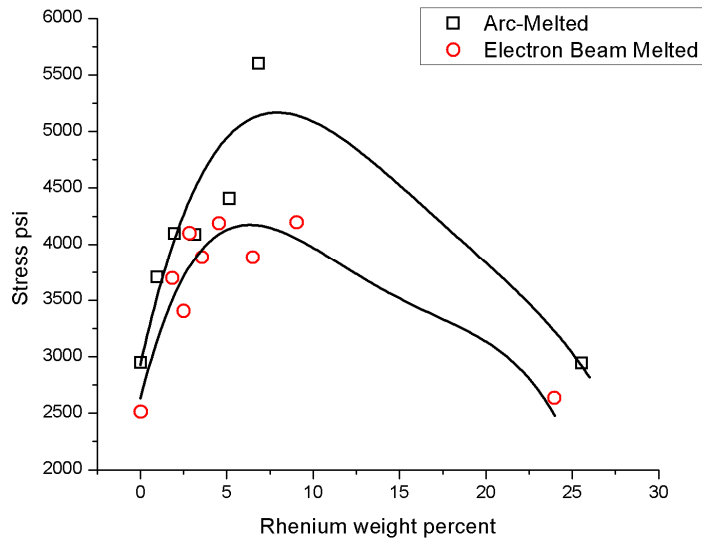
Figure 2. Plot of high temperature strength of W-Re alloys as a function of rhenium content. Steady creep rate 10^{-6} per second; temperature 1927°C (corresponds approximately to rupture life of 50 hrs). Adapted from Klopp *et al*.[33]
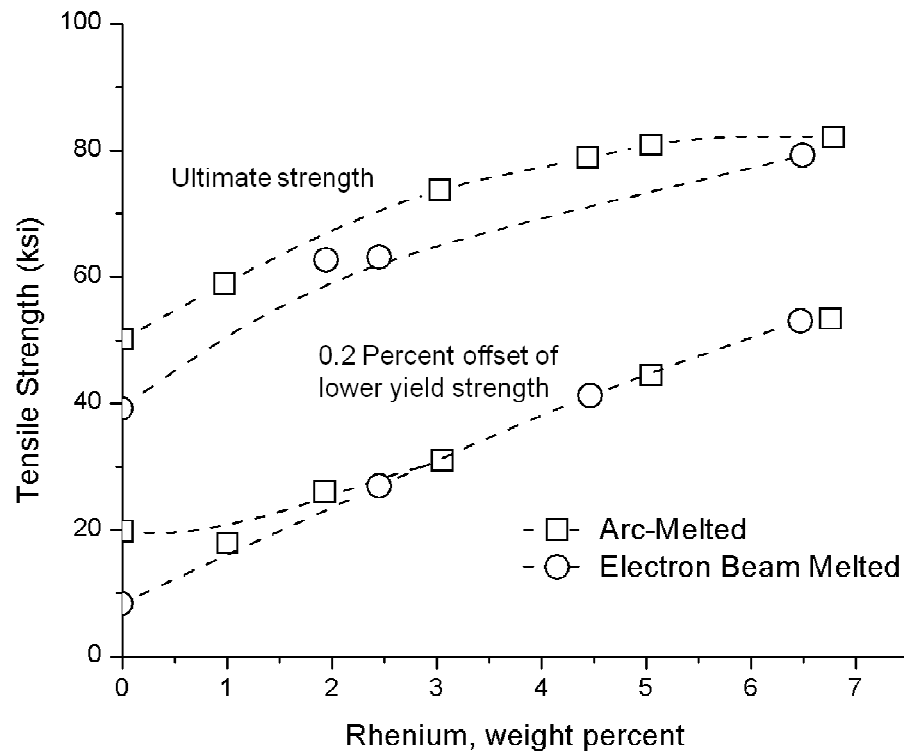
Figure 3. Plot of tensile strength of dilute W-Re alloys at 371°C as a function of rhenium content. Values compiled from three sources (Klopp & Witzke[32], Klopp *et al.*[33], and Witzke *et al.*[58]). Adapted from Klopp *et al.*[33]

The concentration of rhenium in the alloy can yield different properties. Concentrations with 5 at% Re result in a hardness minimum, but the maximum creep strength; this phenomenon is thought to be due to a reduction in the Peierl's stress when alloying.[30; 35] Tungsten has the greatest ductility when alloyed with rhenium concentrations close to the solubility limit, which is approximately 30 at% depending on the processing temperature.[8] This ductilization effect is thought to be largely due to an increase in the number of available slip planes with a smaller part associated with lower stacking fault energies, producing twinning effects.[30] The rhenium ductilization effect is

also believed to be due to a scavenger effect on light element interstitials, where the interstitials are re-distributed from low energy positions (such as dislocations and grain boundaries) to clusters within the lattice.[35] This is thought to increase the grain boundary rupture strength of the W-Re alloy. Alloying to the solubility limit has little effect on the alloy's melting temperature, as increasing rhenium content to 25 at% results in only a small drop in the melting temperature, decreasing from 3422 to 3050°C.[36] Rhenium concentrations beyond the solid solubility limit will yield the intermetallic σ and χ-phases, which will be discussed in a following section of this thesis.

The biggest drawback to the incorporation of rhenium is its cost: the price of rhenium is approximately $900 per kilogram, compared to tungsten, which is approximately $50 per kilogram (as of early 2012).

2.2 - Overview of Sintering Processes and Powder Metallurgy

Tungsten and tungsten-rhenium alloys are commonly fabricated by powder metallurgy methods as casting ingots is a difficult and expensive process.[36; 46] Furthermore, in a study by Stephenson, W-25 at% Re samples produced by powder metallurgical techniques had a lower secondary creep rate at 2200°C.[46] So, processing W-Re powders via powder metallurgy is simpler, more cost-effective, and, at given temperatures, results in alloys less likely to rupture from applied stresses.

Sintering is a fabrication method that has been developed over the course of thousands of years, dating back to the early production of bricks.[19] However, there was little scientific understanding behind the phenomenon until, coincidentally enough, work was done on tungsten powders for light bulb filaments by Coolidge in 1909.[50] Since then, a better understanding of the process has developed, with theoretical models

providing insight into the atomic mechanisms responsible for sintering.[12; 26; 27; 29] The following discussion on sintering and sintering mechanisms relevant to this thesis is summarized from works by German.[19; 20]

The sintering process is a solid state reaction that forms solid bonds between particles when heated sufficiently. The driving force behind this reaction is the overall reduction in surface stresses. The surface stresses of the particles are a function of both the surface energy and the radii of the forming particles, otherwise known as the Laplace equation:

$$\sigma = \gamma \left(\frac{1}{R_1} + \frac{1}{R_2} \right) \tag{1}$$

where σ is the surface stress, γ the surface energy, and R_1 and R_2 are the coalescing particle radii. As these particles are heated, a certain number of atoms can break free from their positions and move. The minimum energy required for these atoms to break their bonds is called an activation energy and the number of atoms that can overcome that activation energy can be expressed with the Arrhenius temperature relation:

$$\frac{N}{N_o} = \exp \left(\frac{-Q}{RT} \right) \tag{2}$$

where N/N_o represents the fraction of atoms present able to break their bonds, Q is the activation energy, R the gas constant, and T the absolute temperature. Atoms with the ability to move are more likely to settle at the interface between particles. In this region, more atomic bonds can be satisfied resulting in atoms in a lower energy state. The bonding between particles usually becomes evident at temperatures approximately half the particle's melting point. With enough atomic migration, there is a build-up between the particles called a neck, which binds the particles together and reduces the overall

volume occupied by the particles. This reduction can be seen in Figure 4, where two spherical particles bond together forming a neck at their interface. Given enough time and heat, the particles eventually coalesce into a single mass.
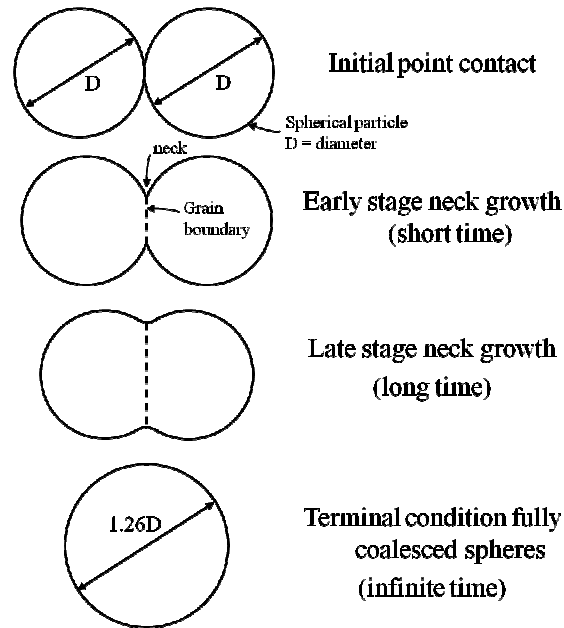
Figure 4.   **Schematic of two sphere model. Adapted from German.[20]**

There are two different types of mechanisms for atomic migration that occur during the sintering process (Figure 5). The lower temperature regime, consisting of surface diffusion and evaporation-condensation, yields no consolidation. A neck can form between the particles; however, the centers of the powders do not move and consolidation does not occur. In contrast, the higher temperature regime of grain boundary and volume diffusion, along with plastic flow, will result in the centers of the particles coming together, shrinkage in the compact, and an overall higher resulting density.
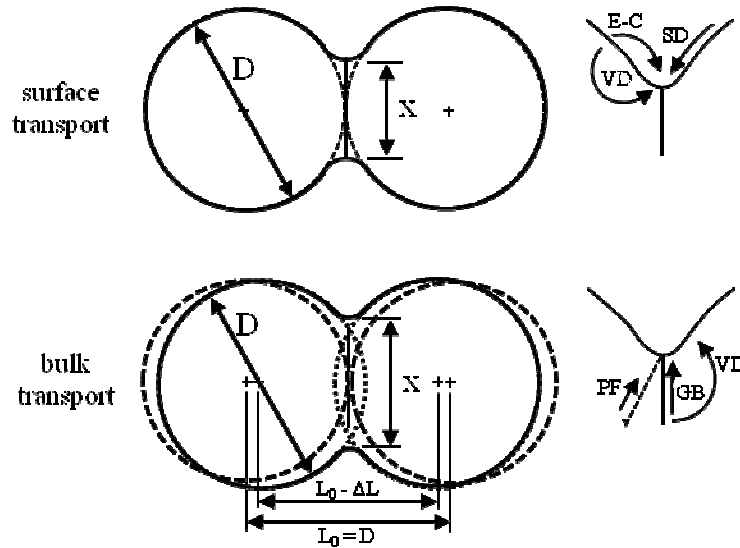
Figure 5. **Schematic of the two classes of sintering mechanisms as applied to a partially sintered geometry. Surface transport mechanisms (evaporation-condensation, surface diffusion, volume diffusion) provide for neck growth by moving mass from surface sources while bulk-transport processes (plastic flow, grain-boundary diffusion, volume diffusion) provide for neck growth using internal mass sources. Only bulk transport mechanisms give shrinkage and densification. Adapted from German.[20]**

There are three stages of sintering: initial, intermediate, and final. The initial stage of sintering is characterized by rapid growth of the inter-particle neck. During the intermediate stage, pores become smoother but remain interconnected, and there is some grain growth at the end of the stage. Final stage sintering yields isolated pores, higher density, and higher amounts of grain growth. When consolidating powders, there is no clear distinction between the sintering stages or the dominant mechanisms occurring as it happens.

To a large extent, there are two approaches to sintering powders: conventional pressureless sintering and pressure-assisted sintering. Conventionally sintered samples are generally pressed in a die at high pressures then the compact is then removed and

thermally treated in a furnace at temperatures where diffusion can occur. This approach is simpler and cheaper than pressure-assisted sintering, which simultaneously applies stress to the powders while sintering. Benefits of pressure-assisted sintering are higher densification rates, less porosity, and increased performance. Drawbacks are comparative cost and contamination from interaction between powders and die/punches, which worsens with longer processing time.

2.2.1 - Shrinkage Background

There are different methods to determine the active mechanisms occurring during sintering. One approach is to use a shrinkage model for early stage sintering as seen in Equation 3:

$$\left(\frac{\Delta L}{L_o}\right) = \frac{B\,t}{2^n\,D^m} \tag{3}$$

where L_o is the initial length of the compact, ΔL is the change in length during sintering, t is the isothermal sintering time, and D, m, and n are materials constants. The variable B is given by:

$$B = B_o\,e^{\left(\frac{-Q}{RT}\right)} \tag{4}$$

where B_o is a collection of material, temperature, and geometric constants, R is the gas constant, T is the absolute temperature, and Q is an activation energy associated with the atomic transport process. Inserting Equation 4 into Equation 3 yields:

$$\left(\frac{\Delta L}{Lo}\right) = \frac{B_o\,e^{\left(\frac{-Q}{RT}\right)}t}{2^n\,D^m} \tag{5}$$

A few simple mathematical steps will results in an equation that relates shrinkage
to the inverse temperature during sintering.

$$\ln\left(\frac{\Delta L}{Lo}\right) = \frac{2}{n}\ln\left(\frac{B_o\,t}{2^n D^m}\right) - \frac{2Q}{nRT} \qquad (6)$$

Once the linear rate of change is determined, values of n associated with different
diffusion mechanisms (as seen in Table 1) can be substituted in. The dominant
mechanism can be inferred after comparing the correlating activation energies with
literature values for the likely mechanism.

**Table 1.   Initial stage sintering mechanisms and associated parameters.
Adapted from German.[20]**

Mechanism	n	m	B
Viscous flow	2	1	$3\gamma/\eta$
Plastic flow	2	1	$9\pi\gamma b D_v/kT$
Evaporation-condensation	3	2	$(3P\gamma/\rho^2)(\pi/2)^{1/2}(M/kT)^{3/2}$
Volume diffusion	5	3	$80D_v\gamma\Omega/kT$
Grain boundary diffusion	6	4	$20\delta D_b\gamma\Omega/kT$
Surface diffusion	7	4	$56D_s\gamma\Omega^{4/3}/kT$

γ = surface energy   Dv = volume diffusivity

η = viscosity   Db = surface diffusivity

b = Burgers vector   Ds = grain boundary diffusivity

k = Boltszmann's constant   P = vapor pressure

T = absolute temperature   M = molecular weight

ρ = theretical density Ω = atomic volume

δ = grain boundary width

There is little contribution to densification during initial stage sintering.
Intermediate stage sintering is much more complex even when considering the shrinkage
of a pure element. For an alloy containing multiple intermetallics phases, determining a
dominant mechanism would be quite complicated and is beyond the scope of this

research. However, while a dominant mechanism might not be established using the shrinkage model, the effects of processing parameters on possible mechanisms occurring within the compacts and how this might change the consolidation process can be inferred.

2.3 - Development of Intermetallics

Rhenium is only partially miscible in tungsten up to approximately 30 at% (depending on processing temperature). Localized rhenium concentrations above that solubility limit will result in the formation of intermetallic phases. The tungsten-rhenium system has two intermetallic phases: σ and χ.[52] The occurrence of either of these phases, even in small quantities, is undesirable as they degrade the properties of the alloy.[8] Of the two, σ-phase is the more problematic intermetallic as it is more stable and difficult to dissolve.[52] The solubility limits for tungsten and rhenium along with compositional ranges for the two intermetallics can be seen in Figure 6.
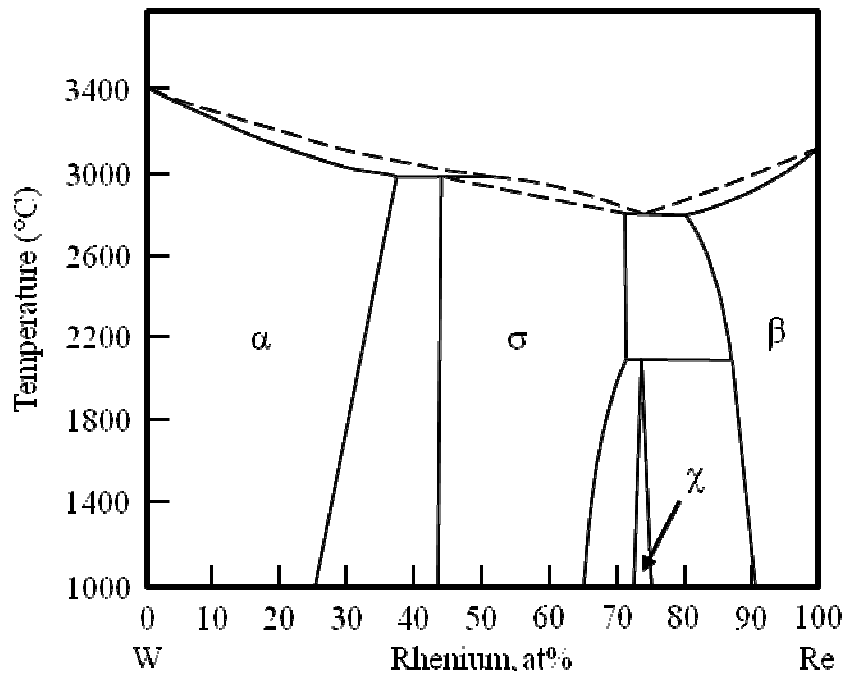
Figure 6.　　**Phase diagram of W-Re system. Adapted from Klopp.[30]**

The σ-phase is a large tetragonal structure containing 30 atoms in the unit cell but with no definite stoichiometry.[5] It is very brittle and has high hardness values of up to HV 1300-2000.[8; 14] A σ-phase particle is rhenium-enriched and, as rhenium has low diffusivity rates in tungsten, the dissolution of this intermetallic phase necessitates either high temperatures or long hold times to allow suitable amounts of diffusion to occur to where the alloy is considered homogeneous.[15]

While the presence of σ-phase is commonly identified in microstructures using XRD and EDS characterization, to our knowledge, there is little research on formation and dissolution rates for σ-phase in spark plasma sintered tungsten-rhenium alloys. However, comparable research on the kinetics of formation and dissolution of σ-phase was conducted by Smith and Hehemann in the early 60's.[52] In their experiments, W-5 at% Re powders were blended and then consolidated using a susceptor-induction furnace in a hydrogen atmosphere. To avoid the development of χ-phase, they sintered all their pellets at temperatures above 2125°C, which is the upper stability limit for the χ-phase, as shown in Figure 6. Their compacts were consolidated at multiple temperatures withhold times ranging from 0 to 100 min to determine phase evolution as a function of sintering time. Their rhenium powders were produced via plasma-arc spraying, which yielded a spherical morphology. This shape allowed easier quantification of the forming and dissolving phases in the W-Re microstructure. The researchers measured the radius of each rhenium particle along with the developing σ-phase forming at the interface between a spherical rhenium particle and surrounding tungsten matrix. This evolution of phases can be seen in Figure 7.
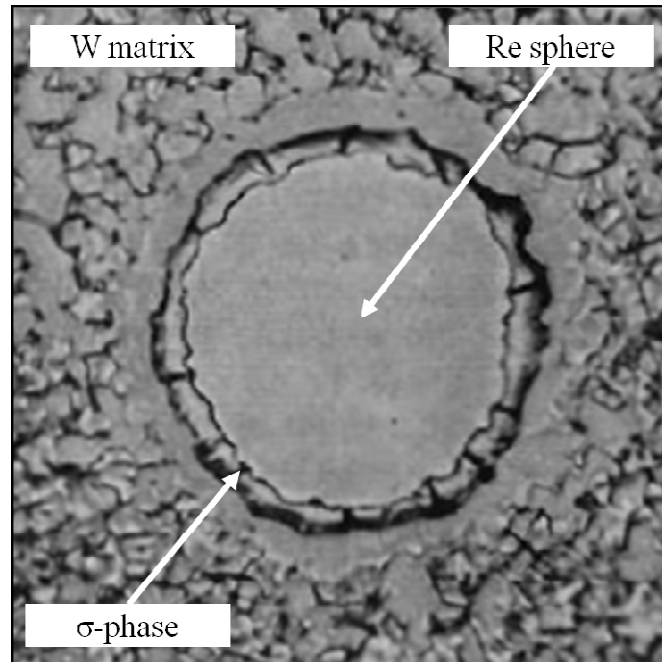
Figure 7. **Optical image of σ-phase forming around round rhenium particle in tungsten matrix. Adapted from Smith and Hehemann.[52]**

Smith and Hehemann used a coarse-grid systematic point count to determine the average radius and volume of the σ and rhenium phases.[52] Figure 8 illustrates the dissolution of the σ and rhenium (α) particles in their compacts.
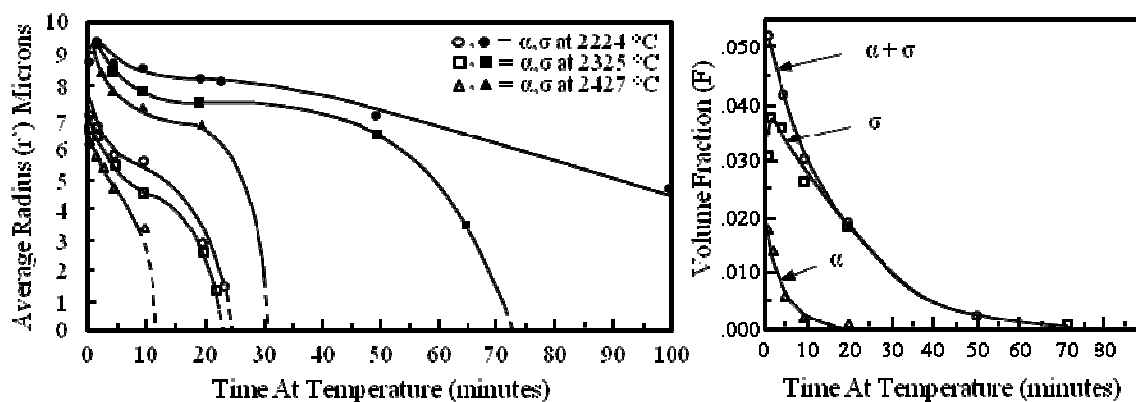
Figure 8. **Average radius of Re (α) and σ-phases as a function of sintering time (left) and volume fractions of Re (α) and σ-phases (normalized to theoretical density) as a function of time at 2325°C (right). Adapted from Smith and Hehemann.[52]**

With this information, and using a parabolic rate law to describe the dissolving rhenium particle, Smith and Hehemann were able to determine dissolution rate constants along with activation energies for both the rhenium and σ-phases.[52] They could then extend these values to calculate the hold times necessary to dissolve σ-phase as a function of sintering hold time at a given temperature. These relations can be seen in Figure 9.
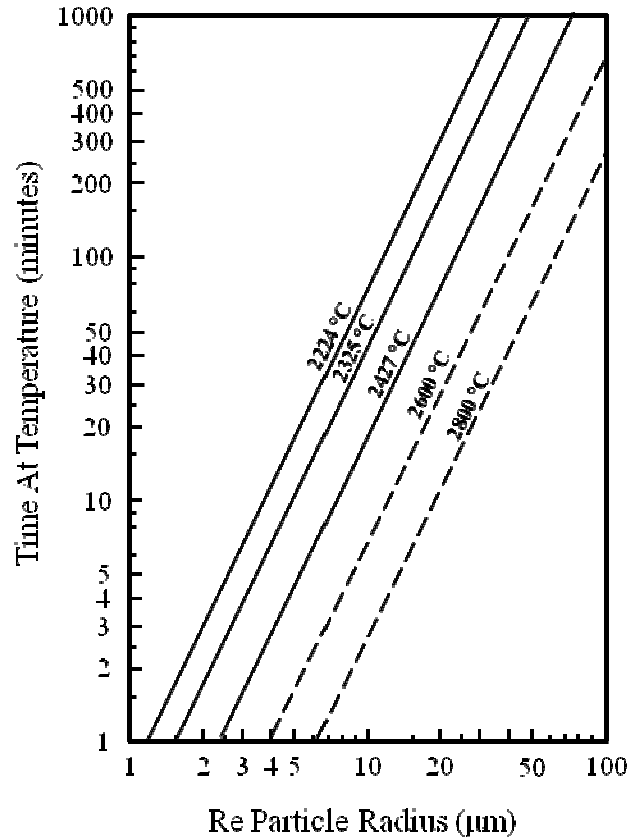
Figure 9.   Time required for σ-phase dissolution for multiple temperatures as a function of rhenium particle size. Adapted from Smith and Hehemann.[52]

Research by Smith and Hehemann shows that higher temperatures, longer hold times, and small rhenium particles will result in less σ-phase in an alloy's microstructure.[52] Unfortunately, the dissolution rates at given temperature determined in their experiments are only valid above 2224°C and for pressure less consolidation techniques similar to their inductor-susceptor approach. Below those temperatures, χ-phase develops and different mechanisms dominate the sintering and dissolution process. Also, the use of pressure assisted sintering methods would likely influence the evolution and dissolution of the phases within the alloy. Regardless, the results of Smith and

Hehemann work provide a fundamental understanding of how σ-phase forms and dissolves as a function of processing parameters.[52]

2.4 - High Energy Ball Milling

High energy ball milling is a powder processing method that has been shown to be effective in synthesizing powders of unique or difficult-to-fabricate materials such as amorphous metals, tungsten-carbide, magnetically isotropic compounds, and difficult-to-alloy transition metal binary alloys.[22; 51; 54] Mechanical milling can be a non-equilibrium processing technique able to synthesize materials with superior homogeneity, and refined and/or metastable crystal structures.[34] It has also been shown to be successful at both refining grain size and mechanically alloying tungsten-rhenium powders.[25; 43]

Mechanical alloying was first developed by Benjamin *et al.* in an effort to synthesize complex oxide dispersion strengthened alloys.[34] The process involves putting powders and milling media in a vial (typically in an inert atmosphere), which is then placed in a ball mill. The mill spins the vial and the powder/media mixture is subjected to high impact collisions as seen in Figure 10.
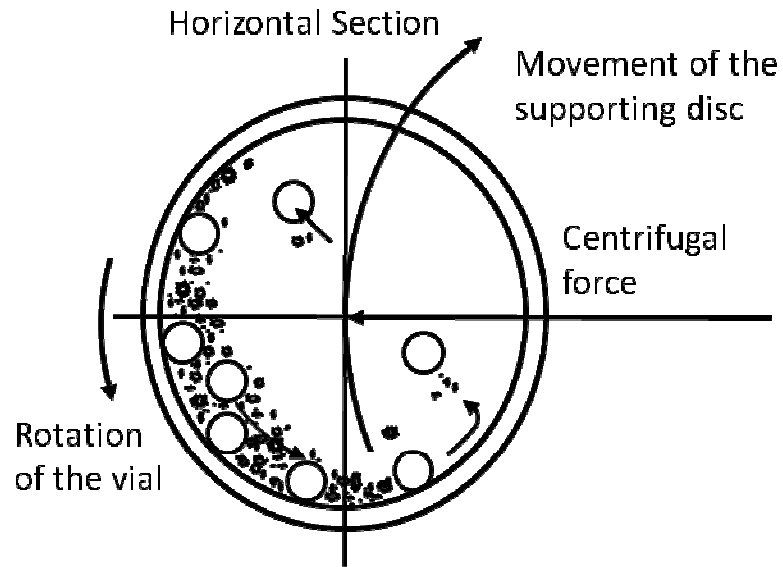
Figure 10. **Schematic depicting the ball motion inside a planetary ball mill. Adapted from Suryanarayana.**[10]

These collisions fracture individual particles while also welding others together. The welding action can initially occur more rapidly than the fracturing, resulting in overall larger particles. Eventually, more particles begin to fracture and a steady state is reached, as seen in Figure 11. This continued process of fracturing and re-welding can result in two types of elemental powders forming homogeneous solid solutions.[10; 38]
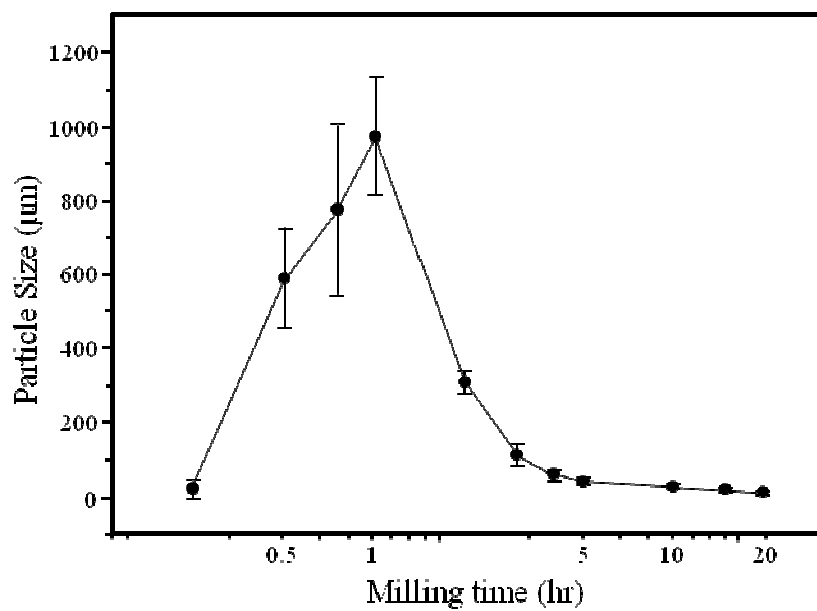
Figure 11. **Particle size distribution as a function of milling time for NiTa. Adapted from Suryanarayana.[10]**

There are many variables that influence the effectiveness of mechanical alloying. Some of the important variables include milling time, milling speed and energy, charge ratio, jar/media size and type.[10] The effects these variables have on the powders are not independent of each other. For instance, increasing the charge ratio has been seen to increase the overall energy imparted to powders, but adding too much media to the jar will restrict the internal movement within the vessel, limiting media-powder interaction.

Ball milling two different powder types can have different results depending on the brittle or ductile nature of each type of powder. For a brittle and ductile combination such as tungsten and rhenium, the theory is that the ductile rhenium powders will flatten into lamellar structures while the brittle tungsten will fragment and embed themselves at the boundaries between the ductile rhenium particles.[4; 10] With longer milling times, the ductile plates become thinner, more convoluted, and the brittle and ductile components

become more evenly distributed. The ball milling process can also aid the

homogenization process by enhancing diffusion pathways by the plastic deformation in

the ductile component.[34] An example of the microstructural evolution for a ductile/brittle

system can be seen in Figure 12.
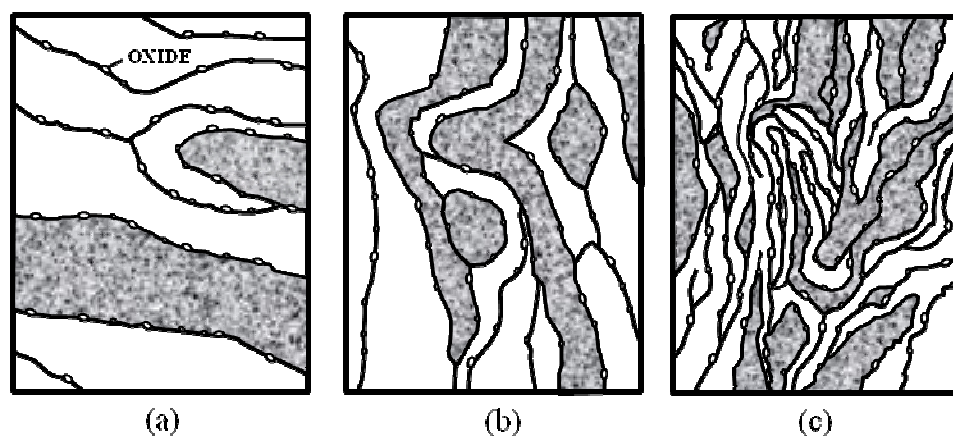
Figure 12.   **Schematic example of microstructural evolution for a ductile-brittle system (oxide dispersion strengthen case), with increased milling time (a to c). Adapted from Suryanarayana.[10]**

Mechanically altering the powders is somewhat of a necessity in producing a W-

Re solid solution. Interdiffusion studies of arc cast tungsten and powder metallurgy

rhenium by Arcella determined diffusion depths as a function of annealing temperature

and time.[3] To achieve a zone width comparable to the average diameter of commercially

available rhenium would take hundreds to thousands of hours for temperatures between

1800°C and 2000°C. A reduction in the average size of the rhenium particles via ball

milling would decrease the diffusion distance and necessary hold times.

Ball milling can decrease powder sizes and aid in the diffusion between binary

compounds. Sintering W-Re powders that are finer and/or have been mechanically

alloyed to some degree can drastically reduce the time required for inter-diffusion to occur, yield less intermetallic phases, and induce superplasticity in the alloy.[25; 43] Ball milling might also be useful in extending the solubility range of rhenium in tungsten. Supersaturated alloys have been synthesized with ball milling for many different systems and this would likely decrease the σ-phase concentration in the alloy.[10]

A drawback to the ball milling process is the rise in contamination levels within the powders. Provided the milling occurs in an inert environment (typically argon), the main source of contamination is likely to be the milling vessel and media. High energy ball milling is a high impact process and, as such, will result in the incorporation of material from the milling jar and media. Dissimilar media/vessel material will incorporate different elements into the powders. In contrast, matching the milling vessel and media material to the powder material will keep different element types out of the powder, but will change the powder composition. The amount of contamination can vary widely even with similar types of milling equipment. For instance, Froes *et al.* found Fe contamination of 3500 ppm when ball milling W-25 wt% Re for 10 h.[15] In a different study, Kim and Koch measured 5 at% Fe concentrations when milling Nb and Sn up to 30 h and Boldrick *et al.* found 3 to 40 at% Fe when milling 1 to 50 h.[7; 28] Chen *et al.* used WC media in a SPEX 8000 steel vessel for higher density type media, yielding increased milling energies; however, they kept their milling times minimal to prevent contamination.[11] This wide variation in contamination found in the literature is likely due to the large differences in charges, milling energy, media size, vessel size, and other factors. These parameters are very rarely reported comprehensively though, so direct comparisons are difficult.

2.5 - Spark Plasma Sintering

Spark Plasma Sintering (SPS) is also known as pulsed electric current sintering (PECS), pulse discharge sintering (PDS), plasma activated sintering (PAS), pulse current sintering (PCS), plasma pressure compaction (P^2C), and field activated sintering technique (FAST), amongst others.[45] The presence of either a spark or plasma is not agreed upon. Recent research using in situ atomic emission spectroscopy suggests that neither is present regardless of the conductivity of the powders.[24]

The SPS technique is a relatively simple process that has been used to consolidate metal, ceramic, intermetallic, and composite powders, typically with superior properties.[45] The key components to the process are the ability to rapidly heat powders while simultaneously applying moderate pressures. Temperature ramp rates are generally hundreds of °C per minute with pressures in the tens of MPa range. The powders to be processed are placed into a cylindrical die, typically comprised of high-strength graphite. Punches, also made of high-strength graphite, are inserted in both ends of the die and placed between the electrodes of the SPS unit, which are located in a vacuum chamber. The chamber is closed and the atmosphere altered as conditions require (typically evacuated). The SPS then pulses DC current through the punch/die configuration with temperature feedback provided by a thermocouple or pyrometer, which monitors the die through a high-temperature quartz window. The current required to heat the system can be hundreds to thousands of amps. A schematic of this process is shown in Figure 13. For more information, a more comprehensive review of the SPS process was compiled by Munir *et al.* [42]
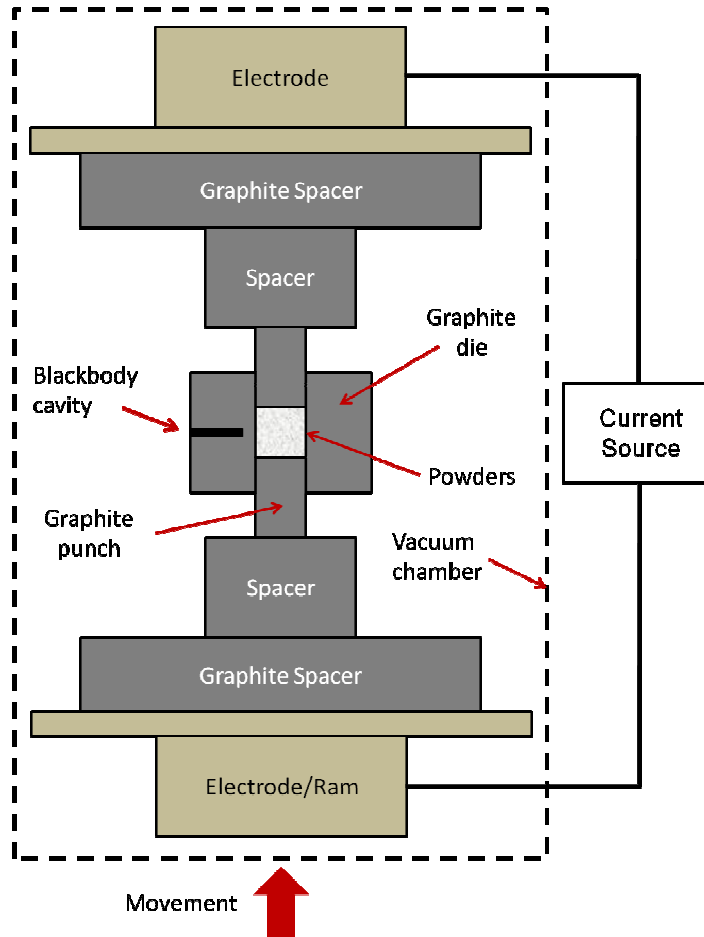
Figure 13. Schematic of SPS sintering configuration

2.5.1 - SPS Effects on Grain Size

The short ramp and hold times used by the SPS typically yield finer grained microstructures.[23; 42; 44; 45] Modeling work by Olevsky *et al.* indicated that a higher heating rate limits surface diffusion that occurs in early stage sintering.[44] This results in less change in pore morphology, which can limit grain boundary diffusion, which contributes to densification. Limiting grain growth during sintering can have positive effects on tungsten's high-temperature mechanical properties. Research by Sutherland and Klopp found that the creep behavior of fine-grained tungsten fabricated through

powder metallurgy was stronger at 4800°F (2649°C) when compared to larger grained samples.[53] In high temperature tensile testing at 2500°F to 4150°F (1371°C to 2282°C), a similar trend for arc-melted tungsten was determined. By decreasing the average grain diameter from 1 mm to 50 μm, the yield strength increased 80% and the ultimate tensile strength 40%.[31] Strain hardening coefficients for recrystallized materials also increased with this drop in grain size.[31] Furthermore, Ratliff *et al.* contended that decreasing grain size increases the grain boundary area, resulting in a lower impurity concentration and improved ductility.[49]

Besides lowering the concentration of impurities and dispersed phases, restricting grain size is also ideal in regards to lowering tungsten's DBTT.[49] Figure 1 illustrates the DBTT values for tungsten and a tungsten-rhenium alloy as a function of the average recrystallized grain diameter. It can be seen that for both the arc and electron beam melted samples, restricting the grain sizes can drastically decrease the transition temperature for the W-Re alloys. Given the difference in processing conditions, it is expected that powder metallurgy samples will have smaller grain sizes and, therefore, transition temperatures even lower in magnitude than those shown.

CHAPTER THREE: EXPERIMENTAL METHODS

The experimental component of this study was comprised of two components; the first to establish the effects of the SPS temperature and hold times, along with the ball milling energy on the tungsten-rhenium powders. This was accomplished by mixing one set of W-25 at% Re powders and varying the temperature and dwell time during SPS. A second set of powders (of the same composition) were ball milled with increasing rotational energy and the resulting powders sintered at one temperature with varying dwell times. The density, grain size, σ-phase content, and hardness values of both sets of consolidated samples were evaluated using SEM/BSE, TEM, XRD, EBSD, and Archimedes method.

The second experimental component consisted of using parameters determined from the first set that result in little to no σ-phase, high density, low grain size, and porosity, along with minimized contamination. These processing parameters were used to fabricate alloy samples with rhenium compositions ranging from 0 to 25 at%. Microstructural evaluation of these samples was conducted using characterization techniques similar to the first set.

3.1 - Evaluation of W and Re Powders

Tungsten (99.99% pure) and rhenium (99.999% pure) powders were purchased from Buffalo Tungsten, Inc. (Depew, NY) and Rhenium Alloys Inc. (Elyria, OH), respectively. According to Buffalo Tungsten, the average powder size was 0.65 μm.

While Rhenium Alloys, Inc. provided a particle size distribution, Buffalo Tungsten did not. To characterize the particle size distribution of the tungsten powders, the diameters of 500 particles were measured from SEM images.[55]

3.1.1 - Particle Size Analysis

The as-received and milled powders were analyzed using a Horiba Partica LA-950 Laser Scattering Particle Size Distribution Analyzer (PSA). The following protocol and parameters were determined by an evaluation performed by Horiba Instruments Inc. on W and W-25 at% Re powder test samples.

Approximately 100 mg of each powder set was added to 50 mL 0.1% sodium pyrophosphate (NaPP) in water. The mixture was then ultra sonicated in a 50 W sonicator for 15 min and then applied to the PSA with an eye-dropper where it was circulated and agitated. The refractive index values for pure tungsten were 3.374 and 2.420i for the red LED and 3.701 and 2.946i for the blue LED. The parameters for W-25 at% Re were 2.951 and 2.42i for the red LED and 3.196 and 2.946i for the blue LED. For the compositions between W and W-25 at% Re, the real component for both refractive indices were interpolated and the imaginary component held constant.

3.2 - Reduction Process

Tungsten and rhenium can have oxides present on and within the powders. Sintering with these oxides present can result in oxygen at grain boundaries, degrading the mechanical properties of the alloy.[1] While there have been recent studies indicating that the electrical current from the SPS debonds the surface oxides, in this study the oxides were removed prior to any sintering.[2] The tungsten and rhenium were reduced

using hydrogen, which bonds with the oxygen, leaving water and pure metal as the by-products.[39; 40]

Both tungsten and rhenium powders were loosely packed into two alumina crucibles and loaded into a 50 mm diameter alumina tube (CoorsTek, Golden, CO) housed in a high temperature furnace (Model 1730-12 HT, CM Furnace, Inc. – Bloomfield, NJ). Both ends of the alumina tube were sealed and a mixture of N_2– 6 at% H_2 gas (Praxair, Salt Lake City, UT, USA) flowed through into a bubbler at a rate of approximately 100 cm^3/min. The temperature of the furnace was ramped to the hold temperature of 850°C at a rate of 5°C/min, allowed to dwell for 6 h, and then ramped down at 5°C/min (profile seen in Figure 14). The powders were then quickly bagged and transferred to an argon-filled glovebox (870-CLC , Lansing, MI) for further processing.
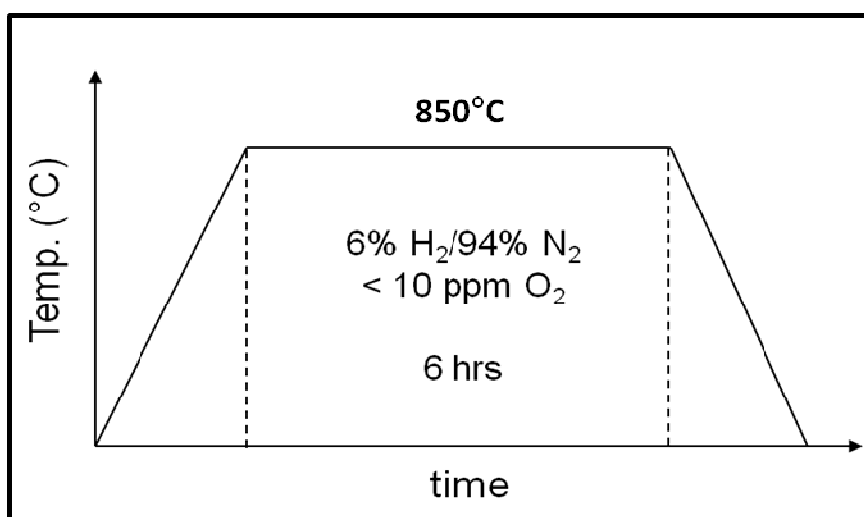
Figure 14.   **Reduction profile for tungsten and rhenium powders**

The powders were examined both before and after the reduction process using a Hitachi-4500S SEM to ensure that no changes in powder morphology with regards to sintering occurred.

3.3 - Powder Processing

3.3.1 - Variable Milling and Temperature Powders

One 50 ± 0.004 g batch of W-25 at% Re powders was blended at 150 rpm for 5 h in a multi-tank mixer (MTI, Inc., Richmond, CA). Another 50 ± 0.004 g batch of powders of the same composition was milled in a Retsch PM100 planetary ball mill at 200, 275, 350, and 400 rpm for 5 h. The milling vessel was a 250 mL hardened steel jar, the milling media 10 mm diameter WC-6 Co balls, the charge ratio ~5/1 media/powder by weight (249g/50g) and a 5:1 duty cycle was used (5 min running and 1 min cool down). The jar, media, and planetary ball mill can be seen in Figure 15.

Previous experimentation with YSZ media in the hardened steel vessel had shown the media rather than the vessel as the prime source of contaminants. WC-6 Co media was used as it was believed that an influx of WC would be preferable to Fe or Zr from the milling media. Both the blended and milled samples were loaded and sealed in an argon-filled glovebox to avoid oxidation during their respective processing.

Figure 15.   Milling vessel and media (left) and PM100 planetary ball mill (right)

3.3.2 - Optimized Powders

Two batches of 60 ± 0.004 g of each composition (W-3 at% Re, W-6 at% Re, W-10 at% Re, W-25 at% Re) were ball milled at 400 rpm for 30 h. The milling vessel and media was WC-6Co. The volume of the milling vessel was 125 mL and the media were 10 mm in diameter. The charge ratio was ~3.9/1 by weight (233.4g/60g) and a 5:1 duty cycle used.

3.4 - XRD of Powders

3.4.1 - Variable Milling and Temperature Powders

The blended and milled W-25 at% Re powders were characterized using an MPD X'Pert XRD tool (Phillips, Inc.). The diffractometer uses a Cu K_α x-ray source and Bragg-Brentano geometry. The powders were scanned with a 2θ of 20 to 120° with a 0.02° step size.

3.4.2 - Optimized Powders

The powders for the optimized powder sets were characterized using an AXS D8 Discover XRD tool (Bruker, Inc.). The diffractometer also uses a Cu K_α x-ray source with a nickel filter, Göbel mirror and germanium primary monochromator. Their scans utilized a Hi-Star area detector with a 2θ ranging from 20 to 50°.

3.5 - Sintering with SPS

The W-Re powders were consolidated in a Dr. Sinter SPSS-515 (Syntex Inc., Kanagawa, Japan) unit owned by Boise State University and housed at the Center for Advanced Energy Studies (CAES) in Idaho Falls, ID (Figure 16). The SPS unit used in

this research has a maximum voltage and current of 20V and 1500A, respectively. The

sintering chamber contains two water-cooled rams that also function as electrodes for the

current. The rams have a maximum range of 65 mm and can apply up to 50 kN of force.

Figure 16.   SPS unit currently housed at CAES facility in Idaho Falls, Idaho

Each sample was consolidated in a die and punch set made from AXF-5Q POCO

high-strength graphite (Figure 17). The outer diameter of the die was 44.5 mm, the inner

diameter 12.7 mm, and the height 30 mm. The die used two punches, which had

diameters of 12 mm, were 20 mm in length, and were fabricated from the same type of

POCO graphite. Each die had a 1.6 mm bore that extended 11.2 mm in from the external

surface. This bore was used as the target for the pyrometer and acted as a blackbody

radiation source. A portable radiation thermometer (Chino IR-AHS) viewed the bore

through a quartz window in the side of the SPS chamber.
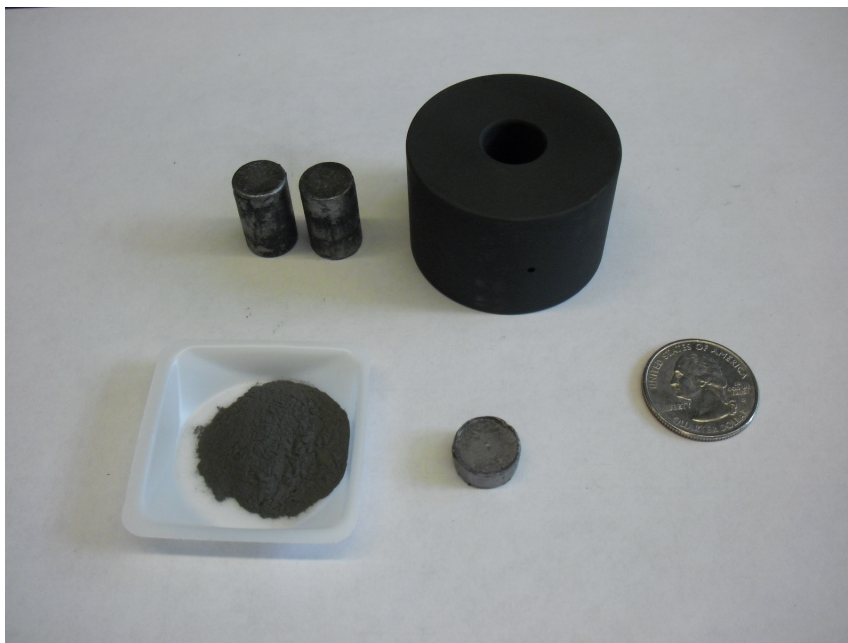
Figure 17. **Photograph of two graphite punches, die, tungsten powders and resulting pellet**

For each sample, the interior of the die was lined with high-purity graphite foil to prevent inter-diffusion between the powders and the carbon in the die. This resulted in a foil encapsulation that required significant grinding to remove, though without the foil the pellet could not be removed without breaking the die. For each sample, a 12 mm graphite foil disk was placed on top of the bottom punch and 8.0 ± 0.02 g were poured into the die. Another 12 mm graphite foil disk was placed on top of the powders and the top punch inserted. The graphite die was then covered with a 4 mm thick carbon felt insulation to minimize heat loss and the thermal gradient from the center of the punches to the edge of the die. Two circular layers of felt were also applied to the top and bottom of the die, with 12 mm holes cut out to allow punch access.

After the die is loaded with powders and the punches inserted, the die set is placed in the SPS chamber. Each electrode has two cylindrical graphite separators: a 25.4 mm

thick, 38.1 mm diameter cylinder on top of a 12.7 mm thick, 101.6 mm diameter cylinder. These separators protect the electrodes from both the high temperatures and force from the punch. The die is balanced on the top separator with the bore directed toward the pyrometer. Two complementary separators were then balanced on the top punch to protect the top electrode. The bottom ram was then raised, compressing the punches into the die. The pyrometer is then aligned and the chamber closed. For each sintering run, the chamber was evacuated and purged three times using a rough pump and argon supply. After the last purge cycle, a booster pump engages, which typically decreases the pressure to 20-30 Pa ($2 - 3 * 10^{-4}$ torr).

The Dr. Sinter unit uses two automatic KP1000 controllers (Chino Corp.) for both the temperature and pressure. After entering the respective profiles, the controllers automatically dictate the current output and ram force to increase or decrease the temperature or pressure, respectively. The data of the temperature, current, force, ram displacement, displacement rate, and chamber pressure were recorded with LabView software at a sample rate of one data point per second.

The pressure profile was also automatically controlled. When starting each sintering run, the controller would ramp the force from the minimum engagement force (4.8 kN) to 5.0 kN in two minutes. This force correlates with a punch pressure of 42.4 MPa. All sintering runs utilized this low ram force to reduce damage to the graphite punches. According to the manufacturer, the AXF-5Q type graphite has a compressive strength of approximately 130 MPa, but at high-temperatures this value is likely to have decreased.

3.6 - Sintering Profiles

3.6.1 - Variable Milling and Temperatures Powders

The blended W-25 at% Re samples were consolidated at 1500°C, 1700°C, and 1900°C for 0, 10, 20, 40, and 60 min hold times. The ball milled W-25 at% Re powders were consolidated at 1700°C with identical dwell times. The constant parameters used for the SPS unit were a ram force of 5.0 kN (42.4 MPa), 100°C/min ramp rate, and low vacuum environment (~20 Pa). These sintering parameters can be seen in Table 2.

Table 2. **Variable milling energy and temperature sintering matrix**

	0 min.	10 min.	20 min.	40 min.	60 min.
1500°C	B	B	B	B	B
1700°C	B, M	B, M	B, M	B, M	B, M
1900°C	B	B	B	B	B

B = Blended W-25 at% Re
M = Ball Milled W-25 at% Re @ 200, 275, 350, and 400 rpm

3.6.2 - Optimized Powders

The variable composition optimized samples were consolidated at 1800°C with 0, 15, and 30 min dwell times with three samples fabricated for each parameter set to show process variability (Table 3). The constant SPS parameters were a ram force of 5.0 kN (42.4 MPa), 100°C/min ramp rate, and low vacuum environment (~20 Pa).

Table 3. **Optimized sample sintering matrix with each condition processed 3 times**

	0 min.	15 min	30 min
W-3 at% Re	x 3	x 3	x 3
W-6 at% Re	x 3	x 3	x 3
W-10 at% Re	x 3	x 3	x 3
W-25 at% Re	x 3	x 3	x 3

The optical pyrometer has a minimum temperature limit of 570°C, so for each sintering run the controller would slowly increase the current until the die temperature was above the minimum. The current would drop, allowing the temperature to return to a programmed hold temperature of 600°C. After stabilizing for 2 min, the current would ramp back up such that the temperature ramp rate would be 100°C/min, which would be maintained until reaching the hold temperature. At the end of the hold time, the current would shut off and the die set would quickly cool to room temperature, which would typically take around 15-20 min. The current and corresponding temperature measurement for a typical processing run is shown in Figure 18.
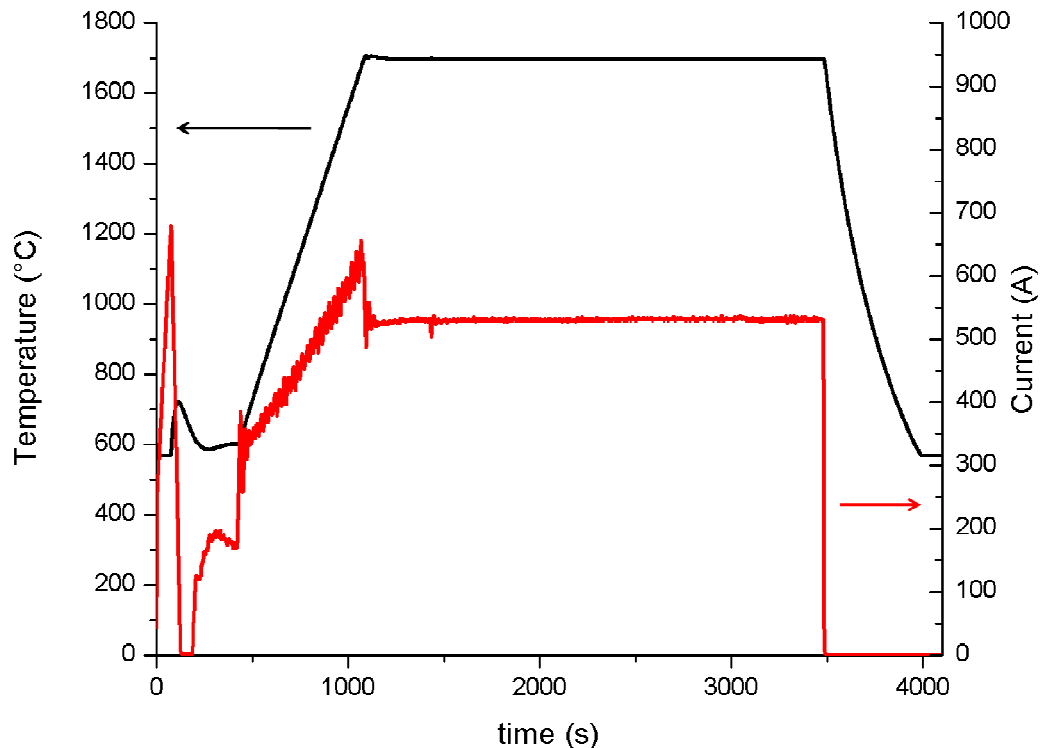
Figure 18.   Typical temperature and current profiles

3.7 - Post-Processing of Samples

After pressing the pellets out of the graphite die using a manual lever press, each sample would have encapsulating graphite foil surrounding its exterior. This would be polished off using a 74 μm diamond pad. The carbon in the graphite foil would also diffuse into the pellet, resulting in a visually darker region that would also need to be ground off with the diamond pad. The amount of time necessary to remove this carbon rich region was a function of the sintering temperature and dwell time but typically required approximately 20-40 min.

3.8 - Density Measurements

After sintering runs, the graphite paper encapsulating each sample was ground off and the densities measured using Archimedes principle. An analytical scale (Mettler Toledo, AB54-S) and associated density kit (33360) were used for all density measurements. A thermometer was inserted into the water in the suspension beaker and the temperature allowed to stabilize before taking measurements. Each sample was measured five times in air and five times suspended in water. The samples were dried off with paper towels between suspension measurements.

3.9 - Metallographic Preparation

After grinding off the grafoil and taking density measurements, the samples were cross-sectioned. Each sample was segmented with a TechCut low speed saw using a high-density diamond blade (Allied High Tech Products, Inc.). The cut was made as close to the center of each pellet as possible, with the cut normal to the surface. One half of the pellet was embedded in a conductive graphite-enfused thermoset compound

(Konductomet, Buehler, Inc.) while the other half was retained for TEM samples and miscellaneous experimentation.

The embedded samples were then ground with SiC polishing paper from 400 to 1200 grit. They were then polished with 1.0 μm and then 0.3 μm Al_2O_3 slurries on nylon felt pads. This was followed by vibratory polishing for six hours in 0.05 μm Al_2O_3 slurry. After washing the sample in de-ionized water, the sample was etched for 5-7 s with Murakami's Reagent (10 mL water, 1 gram potassium ferricyanide, 1 g sodium hydroxide) using a cotton swab. The samples were then quickly washed in de-ionized water, dried with compressed air, and then stored in a vacuum chamber until microstructural characterization. A post-processing flowchart can be seen Figure 19.
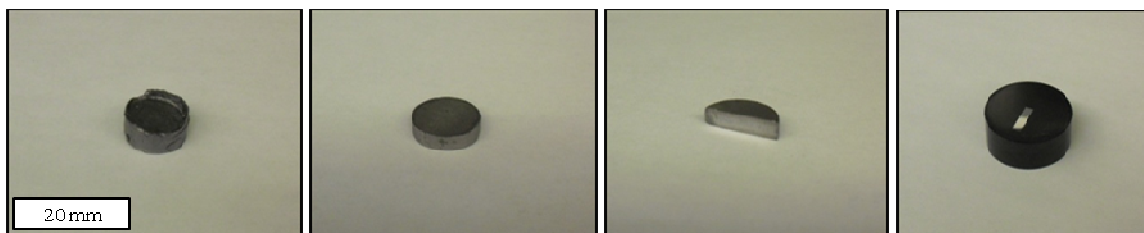
Figure 19.   Photographs of the post-processing steps: removal of grafoil, sectioning, mounted in conductive epoxy (from left to right)

3.10 - Evaluation with XRD

3.10.1 - Variable Milling and Temperature Samples

The cross section of each pellet for the ball milled samples (both variable energy and optimized) and the 1700°C blended set was characterized using an AXS D8 Discover XRD tool. The samples were scanned with a 2θ ranging from 20-50° with a NaI(Tl) scintillation point detector, which utilized a step size of 0.02° with a hold time of 1.5

seconds per step. However, as the samples were smaller than the x-ray spot, their epoxy mounts added their own signature peaks.

3.10.2 - Optimized Samples

One sample from each set of optimized W-25 at% Re was characterized with the AXS D8 Discover XRD tool. These samples had the highest concentration of rhenium and, if present, the highest likelihood of σ-phase presence. The samples were scanned with a 2θ ranging from 20 to 50° with a NaI(Tl) scintillation detector point detector, which utilized a step size of 0.02° with a hold time of 1.5 seconds per step. After reviewing the W-25 at% Re optimized sample's scans, the remaining compositions were not scanned.

3.11 - SEM/BSE Measurements

The amount of σ-phase in each sample was quantified using backscatter electron (BSE) images. The contrast in a BSE image directly correlates to the atomic density at any given point. The differences in packing density for the tungsten, rhenium, and σ-phases can be differentiated in this manner. Each sample was imaged 10-15 times at the center of their cross-section with roughly 100 μm between each image using a Rutherford BSE detector attached to a LEO 1430VP scanning electron microscope. The magnification was 2500x giving each image an area of approximately 41 x 62 μm. This magnification was a balance of having a suitable sampling area versus having the resolution to differentiate phases present. These images were then analyzed using ImageJ software where the area percentage of σ-phase could be determined through both outlining and threshold techniques (Figure 20). The error associated with each sample

was a combination of outlining error and the variability of the rhenium concentration, size, and morphology at that sample point.
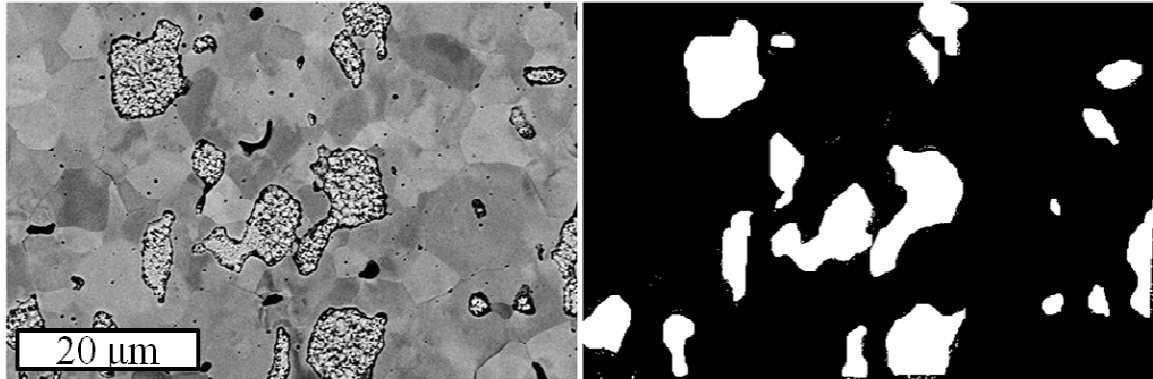
Figure 20.   SEM/BSE image of σ-phase particles in a tungsten matrix (left) and after highlighted using ImageJ software (right)

3.12 - SEM/EBSD

The grain size of each sample was determined using a linear intercept method with an EBSD detector associated with a LEO 1430VP SEM. Each sample was tilted 70° relative to the electron beam and the resulting scanned diffraction patterns captured by the Digiview III CCD camera (Ametek, Inc) and the data collected with TSL OIM Data Collection 5 software.

The accelerating voltage was 25 kV and the working distance 19 mm. An area in the center of each sample's cross section was focused on at 1000x. The beam scanned across the microstructure in a 10x10 grid pattern with a 0.25 μm step size. While lower step sizes would give more accurate measured grain diameters, it was found that changing the step from 0.35 μm down to 0.15 μm on the same scanned region resulted in

a drop in average grain size of 3.1%. Thus, the 0.25 μm step was a compromise of accuracy and scanning speed.

The error of measurement of grain size was 0.13 μm and this was determined by re-scanning a sample three times in different regions near the center of the pellet. However, the number of grains counted for each scan was approximately 570 counts and it is expected that the measurement error would be lower for the higher counts per area associated with the smaller grain samples. The grid would cover an area of approximately 300 μm x 300 μm and count anywhere from 150 to 1200 grains. For lower grain counts, 2-3 additional scans were made.

The optimized samples were scanned using the linear intercept mode for grain size, but additionally had a complete area scan for one of each dwell set for the W-3 at% Re and W-25 at% Re samples. These EBSD area scans provided information in regards to grain and grain boundary structure. The scans covered a 150 μm x 150 μm area and had a 0.34 μm step size.

3.13 - SEM/EDS

3.13.1 - Variable Milling and Temperature Samples

The variable milling speed samples were characterized with regard to composition and contamination levels using an Oxford ISIS-Link EDS system associated with a LEO 1430VP SEM. The accelerating voltage was 20 kV with an area scan at 500x magnification. The count rate was approximately 2000 counts per second for 60 seconds. This was repeated 3-4 times for each sample.

3.13.2 - Optimized Samples

The optimized samples were analyzed for contaminants using the same parameters as those listed for the variable milling and temperature samples but were scanned five times each. A Hitachi S-3400-II Analytical SEM was also used to confirm contamination results found in the optimized samples using STEM/EDS.

3.14 - Hardness Measurements

3.14.1 - Variable Milling and Temperature Samples

Samples were indented with a micro-indenter (LM 247AT, Leco). For both experimental sets, the indents were spaced 700 μm, were indented with 300 gf, 13 s imprint time, and this was in accordance with ASTM E384. The first experimental set was indented with a 4 x 17 grid (Figure 21). This imprinting scheme was to determine whether there were variations in hardness values as a function of position across each pellet.
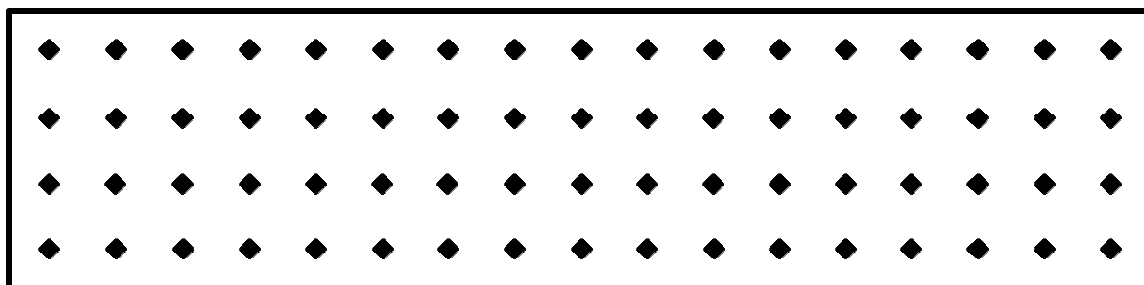
Figure 21.   Indentation scheme for the cross-section of a variable temperature sample

The second experimental set was only indented with a 1 x 10 pattern across their

cross sections for statistics rather than information about hardness as a function of

position (Figure 22). The indents for these samples were in the uncontaminated center of

each sample and were imprinted in accordance with ASTM standards.
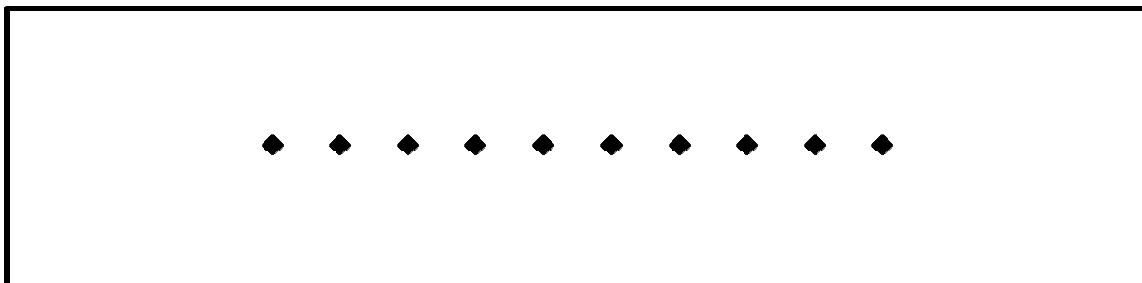
Figure 22.   Indentation scheme for the cross-section of an optimized sample

3.15 - TEM and STEM/EDS

<u>3.15.1 - Variable Milling and Temperature Samples</u>

A sample milled at 400 rpm and consolidated at 1700°C for 40 minutes was

evaluated using a high-resolution analytical TEM (JEM-2100, JEOL). The sample was

prepared using a PIPS ion mill unit. The sample was polished to approximately 100 μm

and then perforated with the PIPS using an accelerating voltage of 5 kV and an incident

angle of 9° for 13 h. The sample was evaluated for elemental distribution using the TEM

in STEM/EDS mode.

3.15.2 - Optimized Samples

W-25 at% Re samples from the optimized experimental set were analyzed for contamination, elemental distribution, and crystal structure using the same TEM. The grain boundaries of these samples were also examined for precipitates and oxides using HRTEM techniques.

The samples were prepared using two different approaches. The first method was manually grinding to approximately 100 μm thick and then perforating the center using a dimple grinder. The perforation was then ion milled using a PIPS ion mill unit. The accelerating voltage was 5 kV with the sample inclined sequentially, first at 4° for 1 h, 8-9° for 5.5 h and then 2° for 40 min to clean the surface. The second set was prepared using a dual-beam focused ion beam (Quanta 3D FEG, FEI Incorporated).

CHAPTER FOUR: RESULTS AND DISCUSSION

4.1 - Variable Milling Energy and Temperature Trials

4.1.1 - Evaluation of As-Received Powders

The SEM analysis revealed that the tungsten powders form polygonal aggregates while the rhenium powders were more rounded and ligamental. The rhenium was also seen to aggregate together to a much higher degree than the tungsten powders and to be much larger in size. The structure and morphologies of the two powder types can be seen in Figure 23.
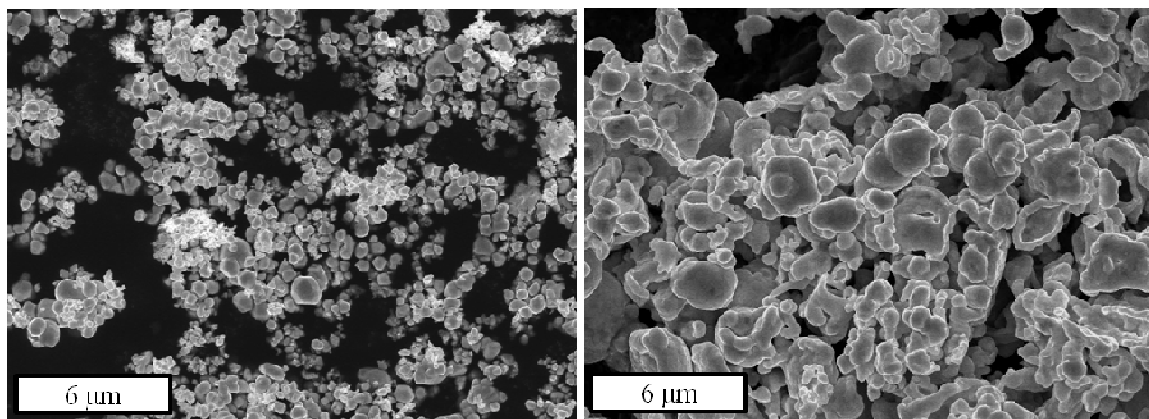
Figure 23. **SEM images of as-received tungsten (left) and rhenium powders (right)**

The SEM measurements showed the tungsten powders had an average size of 0.43 μm. The compilation of the measured particle sizes from these tungsten particles measurements along with the manufacturer data for the rhenium particles is shown in

Figure 24. This bi-modal distribution of the two powders has ramifications on the alloy's

sinterability and resulting microstructure. Given the Laplace relationship, the small size

of the tungsten should aid in sintering, to a much higher degree than the larger rhenium

particles. These large rhenium particles will also result in more σ-phase, as the diffusional

pathways from the interior of each rhenium particle to the tungsten matrix will be greater,

requiring longer sintering times to homogenize the alloy microstructure.
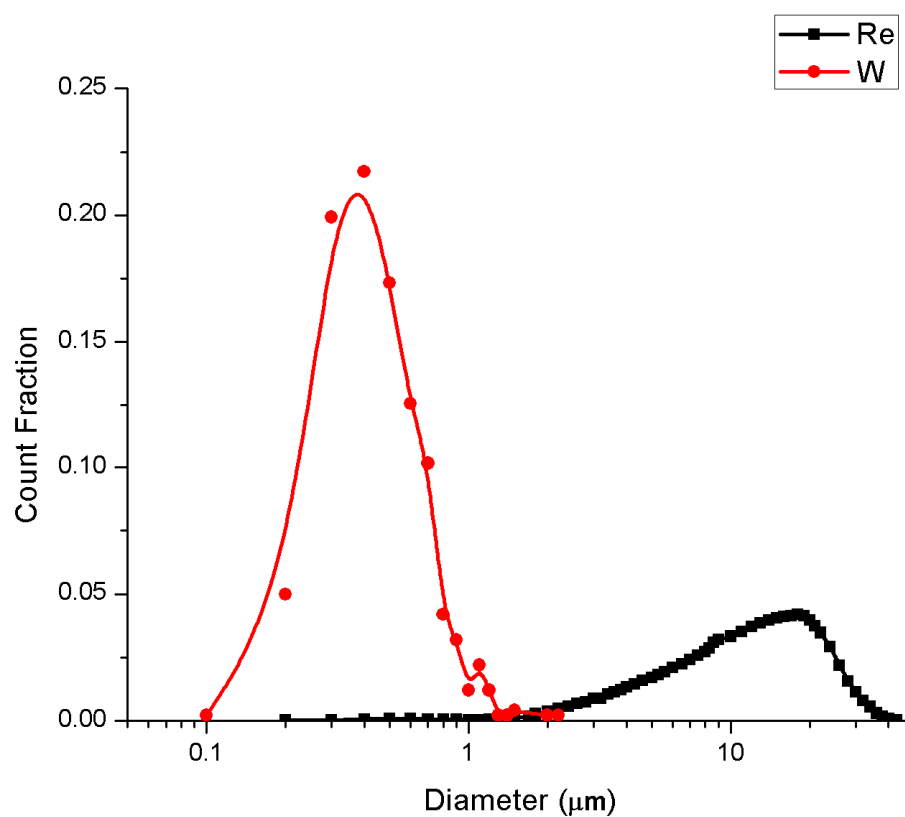
Figure 24.   **Particle size distributions for as-received tungsten and rhenium**

4.1.2 - Reduced Powders

The SEM analysis of the reduced powders showed that there was no morphological change for either powder types in regards to sintering (Figure 25). There was no necking seen between the powders and no aggregates. The tungsten powders did, however, form large collections of particles, which Lassner and Schubert indicate to be a structure called a pseudomorph.[35] This is a remnant structure of a previous structural arrangement formed as the oxides reduce to pure metal. So, while this is not a definite indication as to whether the powders were completely reduced, it is a positive indicator of oxygen being removed from the particles.
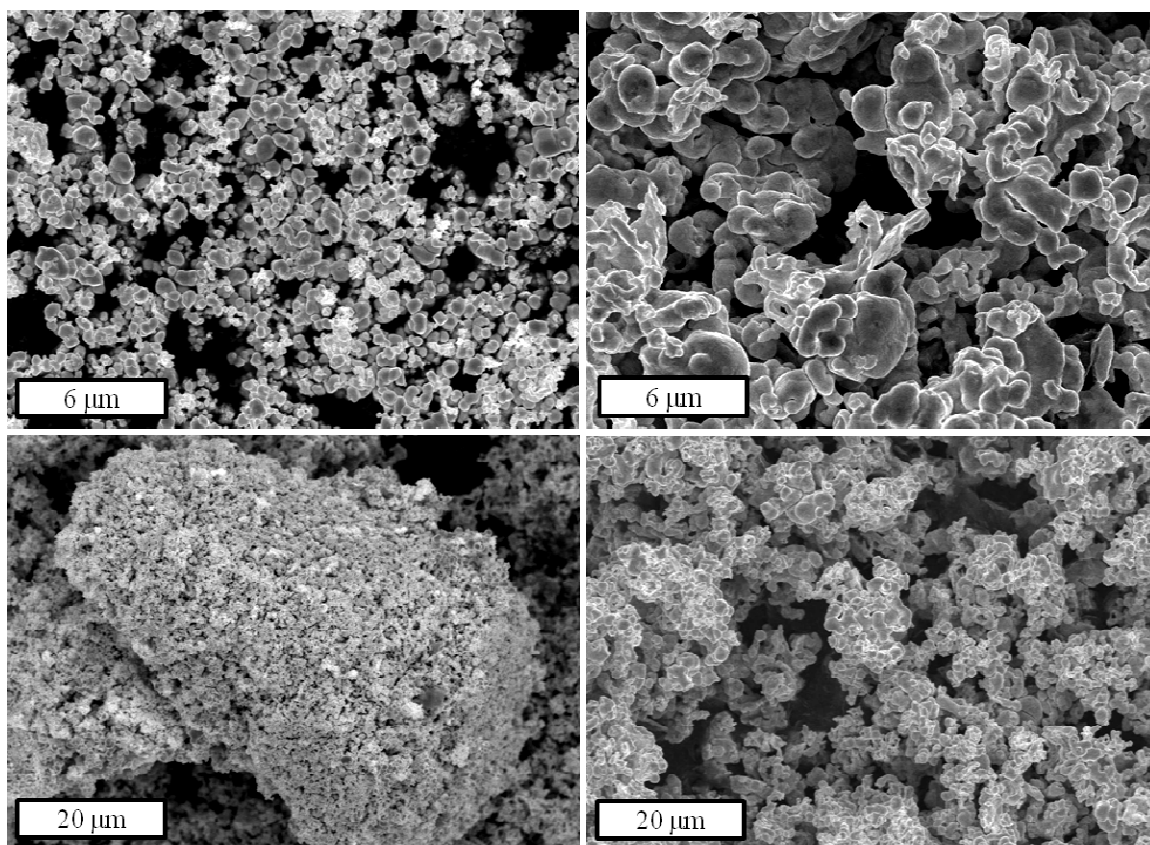
Figure 25.   **SEM images of tungsten (left column) and rhenium (right column) both as-received (top row) and after hydrogen reduction (bottom row)**

4.1.3 - Particle Size Distributions

The particle size distributions for the variable milling energy powders resulted in an increase in the average particle size with increased milling energy. This shift in average particle size is seen in Figure 26, with the average size increasing from 1.09 μm to 3.17 μm with an increase of milling energy from 200 rpm to 400 rpm, respectively. This is likely due to the incorporation of the much larger rhenium particles with the tungsten particles. Unfortunately, it appears that either the particle size analyzer was unable to gauge pure rhenium with the protocol developed by Horiba labs or the very wide distribution of rhenium resulted in too few counts to detect relative to the tungsten and tungsten-rhenium particles. Regardless, the distributions do show a distinguishable growth in particle size as a function of milling speed and energy.
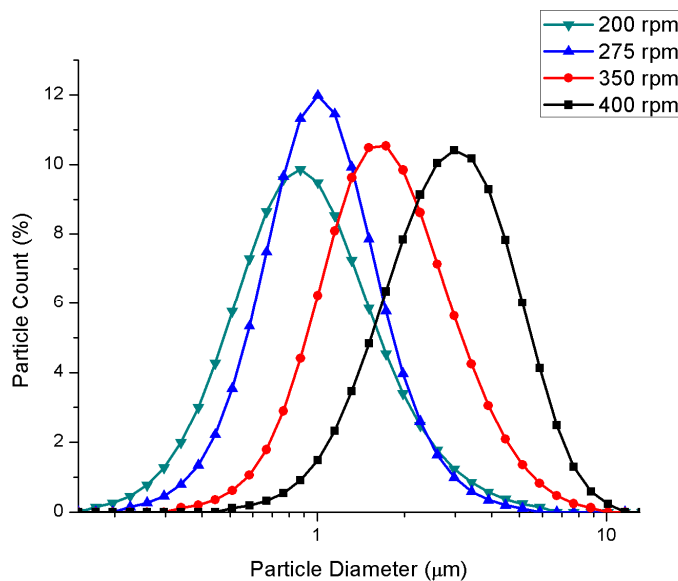
Figure 26.   **Particle size distributions for the W-25 at% Re powders milled with variable speeds**

The tungsten-rhenium powders milled at 400 rpm are shown compared to the as-received powders in Figure 27.The differences in the distributions constitute a signifigant alteration in the tungsten and, more importantly, the rhenium average sizes.
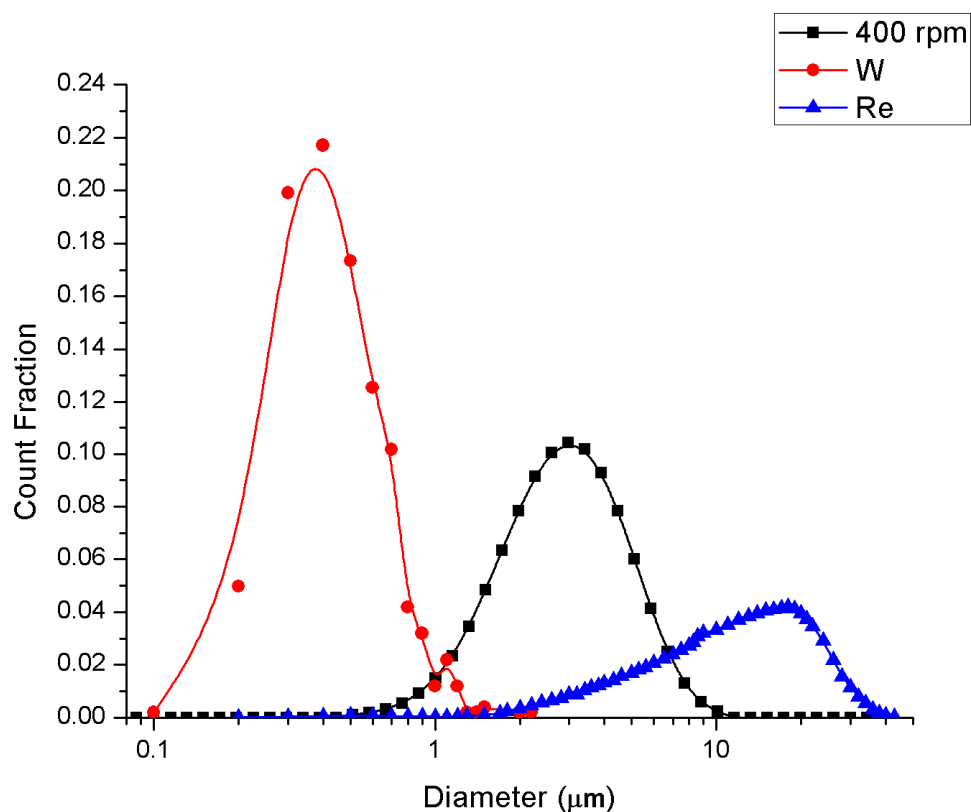
Figure 27.   Particle size distributions for the as-received tungsten, rhenium along with the W-25 at% Re milled at 400 rpm

4.1.4 - SEM Analysis of Milled and Blended Powders

The SEM micrographs illustrate that there is little change in the morphology of the blended powders when compared to the as-received tungsten and rhenium powders. The blending process was low energy and only intended to uniformly mix the two

powder types, not change their shape or particle size. The interspersed powders can be seen in Figure 28.
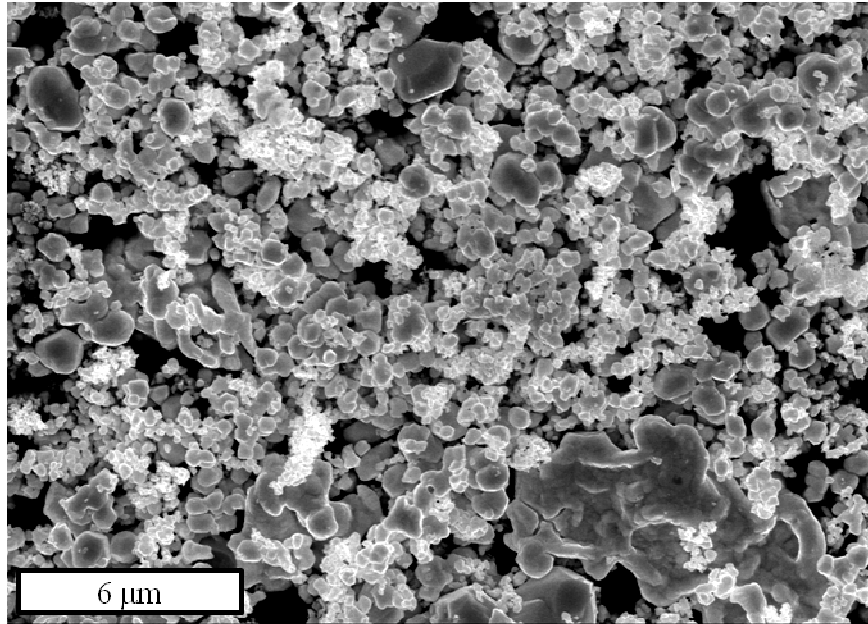
Figure 28.   SEM image of blended W-25 at% Re powders

There was, however, a significant change in the morphology for the milled samples. Figure 29 shows that there is an obvious disparity in particle sizes for the 200 rpm batch. The disparity appears to shrink with higher milling energies until, at 400 rpm, the particles seem more homogeneous in size and the general morphology of the particles becomes more rounded in shape. This increase in particle size agrees with the changes seen in the particle size distributions.
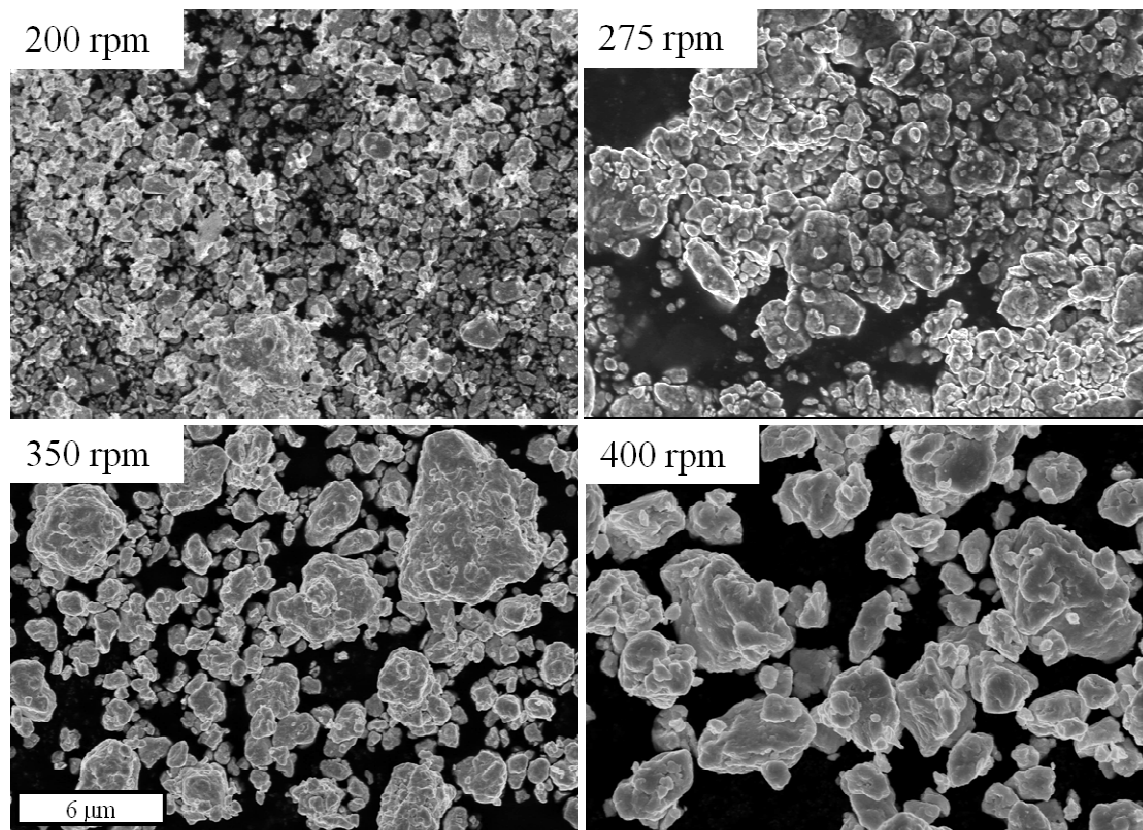
Figure 29.   SEM images of W-25 at% Re powders ball milled at 200 rpm to 400 rpm

4.1.5 - XRD of Powders

The XRD scans shown in Figure 30 illustrate the effect of milling energy on the

W-25 at% Re powders. There is a general broadening of the full width, half max

(FWHM) for each tungsten and rhenium peak. This is likely due to a reduction in

crystallite size for both powder types. The 100% rhenium peak [3101] shown in Figure

31 can be seen to decrease in amplitude while increasing in peak width. This may suggest

that the rhenium is mechanically alloying into the tungsten BCC matrix. Both the

reduction of crystallite sizes and alloying between tungsten and rhenium particles will aid

in sintering and homogenization of the powders.
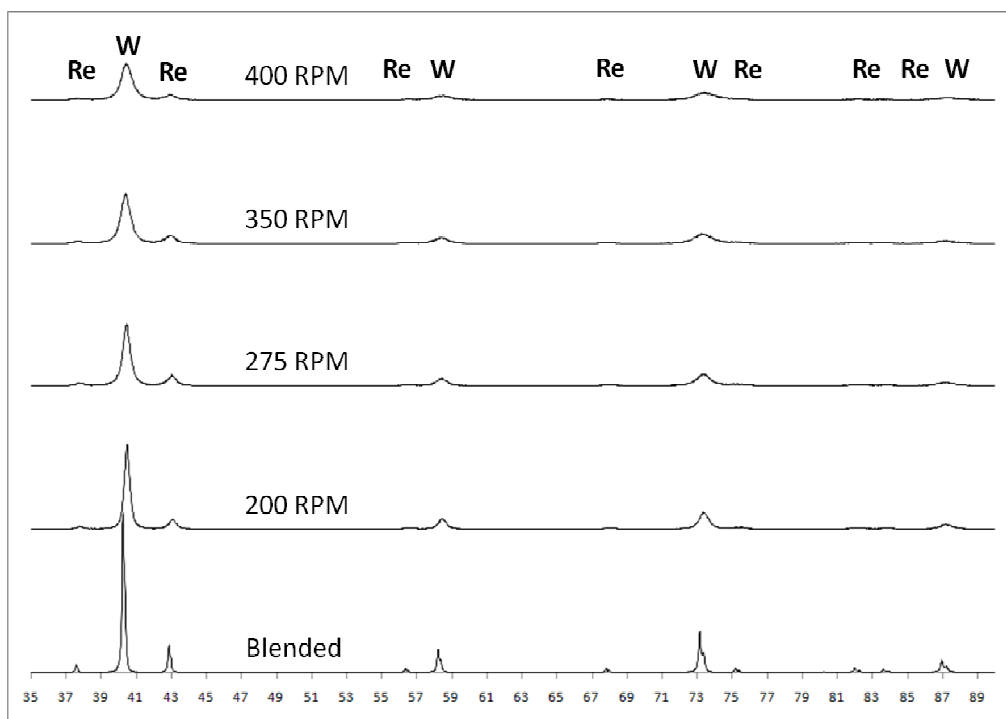
Figure 30.   XRD scans for the blended and milled W-25 at% Re powders
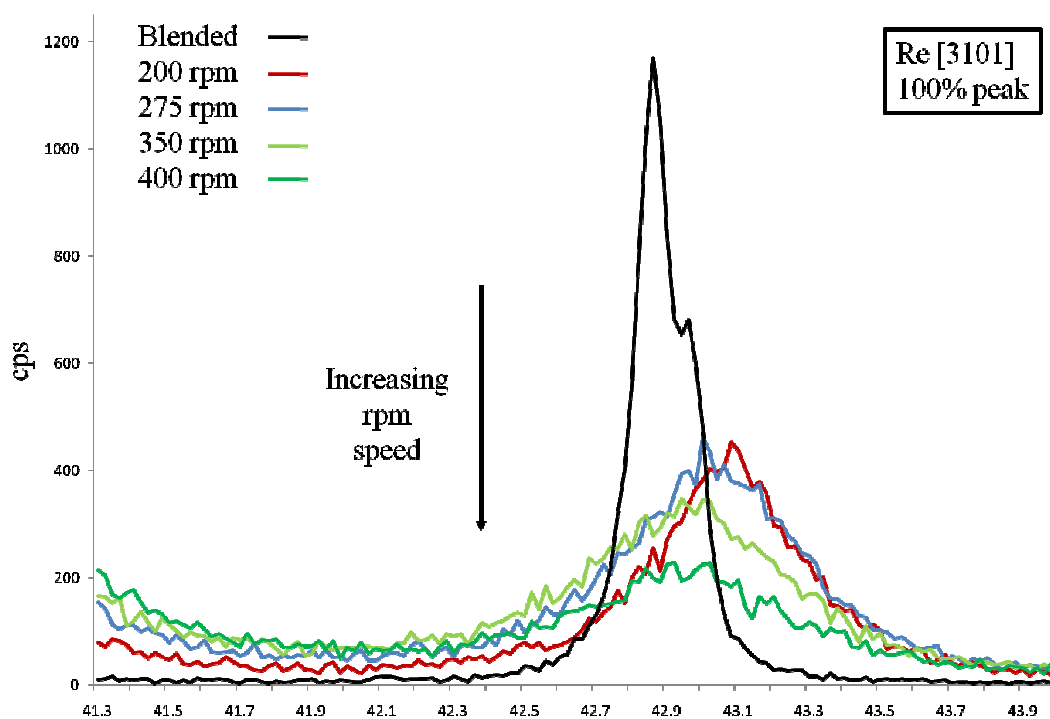
Figure 31.   Overlaid Re 100% XRD peaks for blended and milled W-25 at% Re powders

4.1.6 - Displacement Curves

One of the datum recorded by the SPS is the ram displacement as each sample is consolidated. The rate and degree of displacement can provide clues with regards to dominant mechanisms, densification rates, packing efficiency, etc. The displacements for the blended W-25 at% Re samples are seen in Figure 32.

The majority of the displacement of the SPS rams occurred between 800°C to 1300°C during the temperature ramp. There is little difference between the 1500°C, 1700°C, and 1900°C curves, suggesting similar mechanisms occurring during the consolidation. The amount of displacement for each sample is also comparable suggesting analogous densities (provided similar packing efficiencies during initial powder compression).
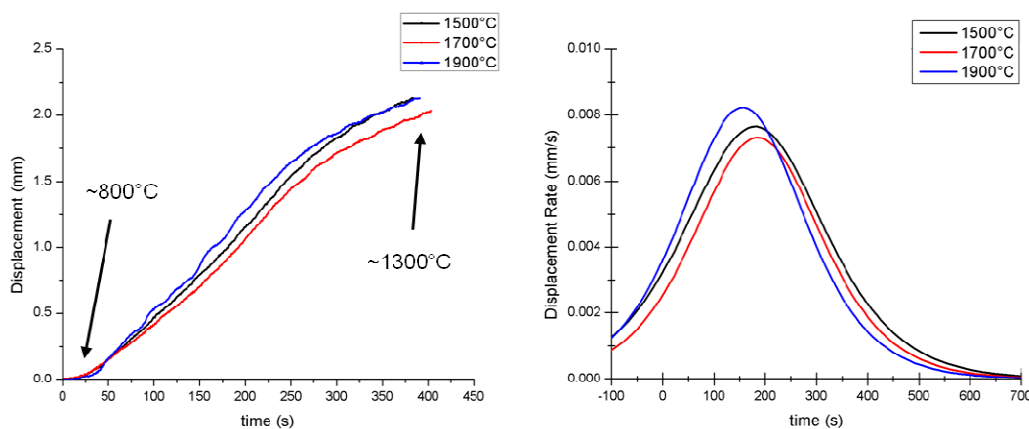
Figure 32.   SPS ram displacement (left) and modeled displacement rate (right) as a function of sintering time for the blended W-25 at% Re samples

The displacement data for the variable energy ball milled samples is markedly different than that of the blended samples. The degree of displacement for this experimental set is approximately 40% less than the overall blended displacment. This

may be due to a lower final density or a much higher packing density upon initial compression in the ball milled samples.

The rate of displacement for the ball milled samples is also signifigantly different from the blended samples. The ultimate displacement is reached in a shorter amount of time during the temperature ramp. This may be due to a change in mechanism during sintering. There is also a discernable difference between the displacement rates as a function of milling speed. The 400 rpm powders are seen to consolidate in approximately 70% the amount of time required for the 200 rpm sample. The changes in the displacement and displacement rates are shown in Figure 33.
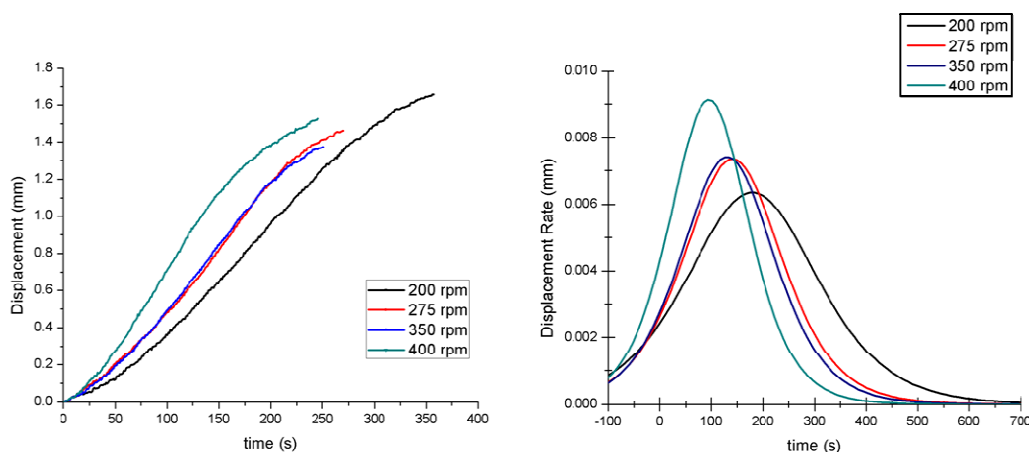
Figure 33.   SPS ram displacement (left) and modeled displacement rate (right) as a function of sintering time for the milled W-25 at% Re samples

4.1.7 - Density Trends

The theoretical density of the W-25 at% Re pellets was a weighted average of the density of tungsten and rhenium (19.68 g/cm^3). However, if the rhenium atoms diffused completely into solid solution within the tungsten BCC crystal then the actual theoretical

density would be approximately 19.37 g/cm^3. The average densities of the blended and milled samples exceeded 94% theoretical density. There was a general drop in density with longer dwell times for both the blended and milled samples as seen in Figure 34 and Figure 35, respectively. This drop is likely a combination of effects: the dissolution of rhenium, the dissolution of σ-phase, and the diffusional influx of carbon from the surrounding grafoil.
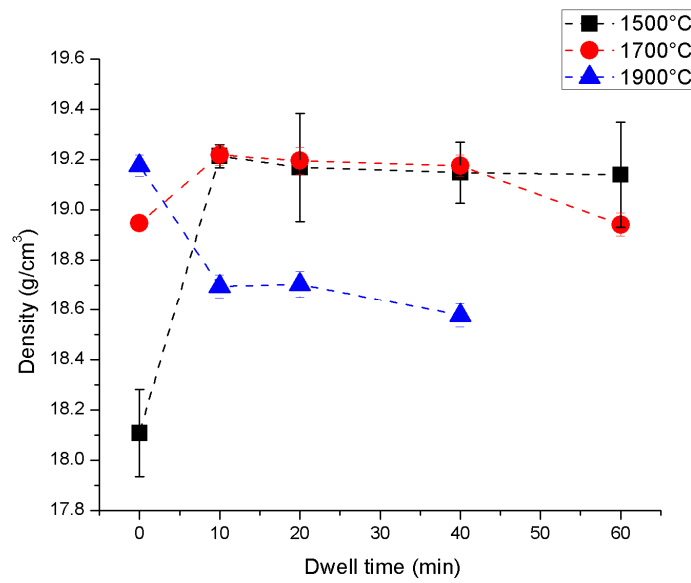
Figure 34.   Density as a function of SPS dwell time for blended W-25 at% Re samples
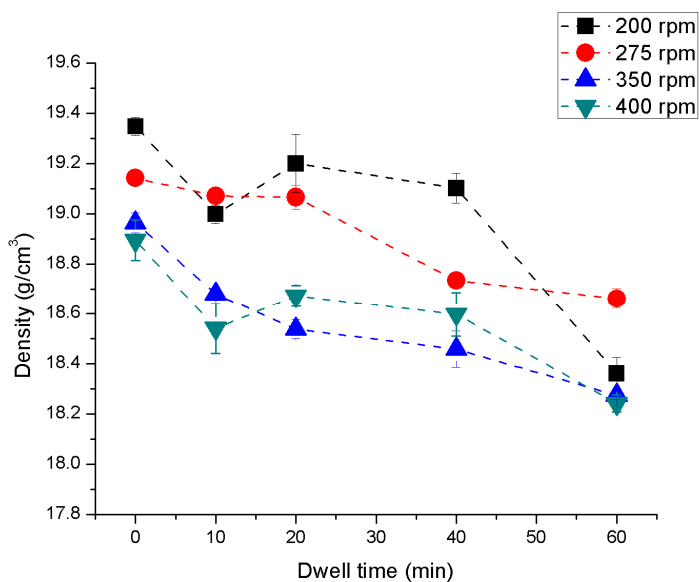
Figure 35. Density as a function of SPS dwell time for milled W-25 at% Re samples

The density measurements indicate that values close to theoretical density at the beginning of the hold time but will drop during the remainder of the dwell due to the incorporation of carbon diffusing in from the surrounding graphite paper. This contamination and resulting higher porosity at the edges of a sample is undesirable for a number of reasons. This problem can be avoided if a different type of high-temperature material can be used to separate the W-Re powders from the graphite die. Samples were fabricated using niobium foils to insulate and there was little contamination found. This is due to the much smaller diffusivity of niobium in tungsten and shorter penetration depth. Comparison cross-sections of samples sintered at the same temperature and hold times are shown in Figure 36. White and Jurkowitz characterized the carbide layer that formed while hot pressing 2.0 μm tungsten in a graphite die at 1800°C for 30 min.[56] The layer

extended between 101 to 203 μm and this influx was inversely related to the pressure applied. White's results are comparable to what was found in this study.
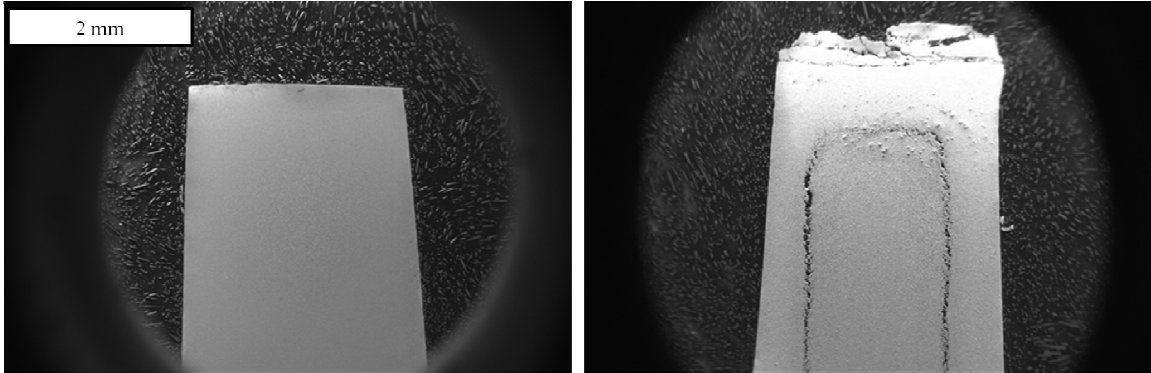
Figure 36.   SEM images of W-25 at% Re sample sintered with no dwell (left) and 30 minute dwell (right)

4.1.8 - Shrinkage Model

A shrinkage model can be used to infer an activation energy for different mechanism types if the final density is known. The displacement data from the SPS ram had the thermal expansion of the graphite subtracted out and knowing the final volume of what the allotment of powders used would occupy, the values for ΔL and L_o were determined. When plotting the natural logarithm of the ratio of these two values versus inverse temperature during heating (seen in Figure 37), a slope can be determined that equals $2Q/nR$. One can then vary the value of the materials constant n for values for surface, grain boundary, and volume diffusion values.
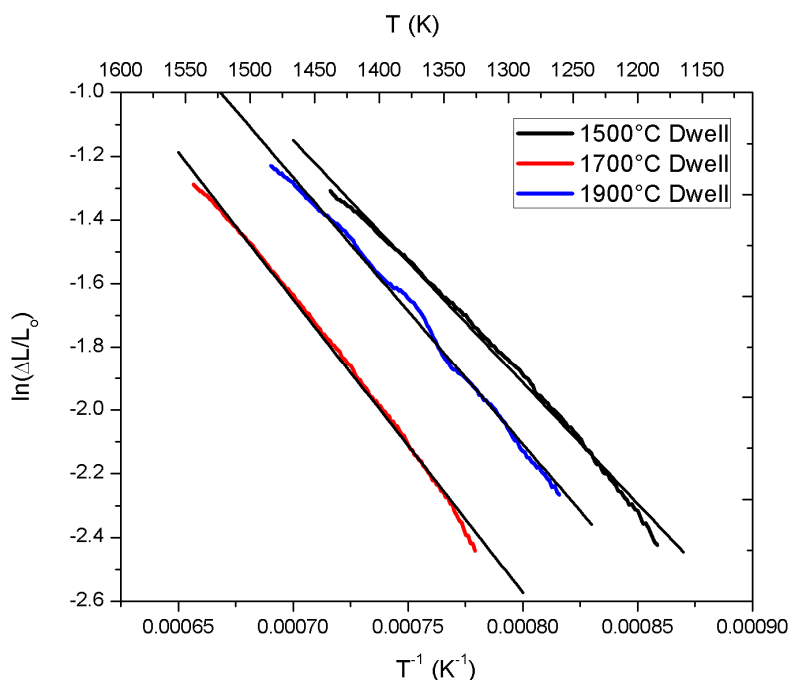
Figure 37. **Logarithmic shrinkage as a function of inverse temperature for the W-25 at% Re blended samples**

The slopes and resulting activation energy values for the blended samples are shown in Table 4. There is a slight increase for each mechanism type correlating with an increase in SPS temperature. This could signify the inclusion of higher energy mechanisms of the mass-transport class with higher temperatures. As for determining the dominant mechanism, the only activation energy value that could be found in the literature that had been processed using comparable methods and temperatures was 180 kJ/mol for grain boundary diffusion.[3] While this value is close to those calculated for grain boundary diffusion in Table 4, the shrinkage data used here extends through the intermediary and final regions of sintering where there are multiple mechanisms occurring. Hence, these values are more useful as a comparison to processing changes within this study.

Table 4. **Potential activation energies and mechanisms from shrinkage data for the blended W-25 at% Re samples**

		(Vol. Diff.)	*(GB Diff.)*	*(Surface diff.)*
	Slope	**n = 5 (kJ/mol)**	**n = 6 (kJ/mol)**	**n = 7 (kJ/mol)**
1500°C	7626	160	190	220
1700°C	8406	180	210	250
1900°C	9226	190	230	270

The milled W-25 at% Re samples shrinkage data is shown in Figure 38 and it can be seen that the slopes are steeper than those seen for the blended samples. This higher slope yields average activation energies that are roughly 60% higher than those found for the blended samples. These values can be seen in Table 5. And while all milled values are higher than the blended samples, there does not appear to be a trend with regards to milling speed and energy. This increase in overall energy between the blended and milled results could be due to the change in powder structure during processing. Ball milling the powders will introduce dislocations, vacancies, and a higher number of grain boundaries from the layering effect.[10] This in turn would yield a larger contribution of mechanisms from the higher energy mass transport class when compared to the blended samples. However, this would result in an increase in calculated activation energy as a function of milling energy and that is not seen in Table 5. This discrepancy may be a result of the accuracy of using the shrinkage model in that there is a clear distinction between the blended and milled but not between the different milled samples.
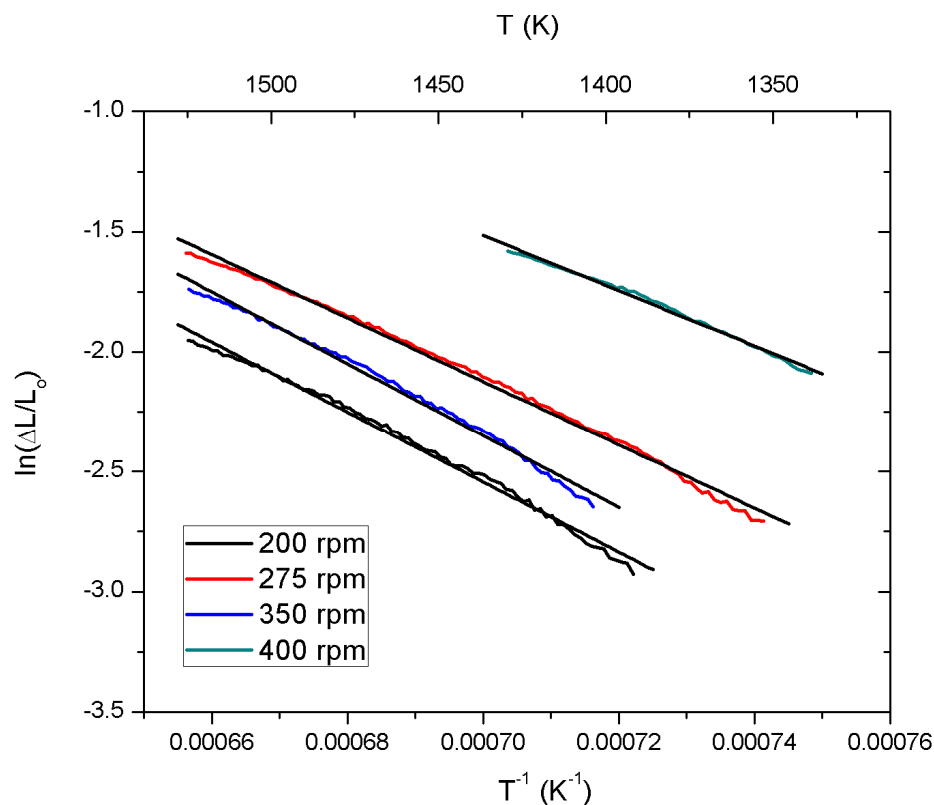
Figure 38. **Logarithmic shrinkage as a function of inverse temperature for the W-25 at% Re milled samples**

Table 5. **Potential activation energies and mechanisms from shrinkage data for the milled W-25 at% Re samples**

	Slope	(Vol. Diff.) n = 5 (kJ/mol)	(GB Diff.) n = 6 (kJ/mol)	(Surface diff.) n = 7 (kJ/mol)
200 rpm	14598	300	360	430
275 rpm	13218	270	330	390
350 rpm	14959	310	370	440
400 rpm	11494	240	290	330

4.1.9 - Microstructure

The SEM/BSE image results are shown in Figure 39. The σ-phase can be seen to be brighter than the surrounding tungsten matrix. There was variability in the

effectiveness of the etching process which may be due to the time between polishing and etching and/or the length of time the Murakami reagent was applied. There were samples that were not immediately etched after being removed from the vibratory polisher and it is possible that the alloy may have slightly oxidized during the interim. The etching time was 5 to 7 s, which could also yield a wide degree of variability in the degree of grain relief.

There are pores that can be seen in the microstructures especially in the 1500°C sintered with no dwell, correlating with the Archimedes density results. For the remaining samples, the porosity is much smaller, also agreeing with the density measurements. There were many dark regions that contain orthogonal-like structures. These were later determined to likely be WO_2 using EDS. These regions also appeared to increase in number with longer SPS dwell time. This may be due to an issue with the seal of the SPS chamber but this would likely yield much more WO_2 near the edge of the samples, which was not seen. In more likelihood, the powders had been contaminated prior to consolidation or not reduced sufficiently.
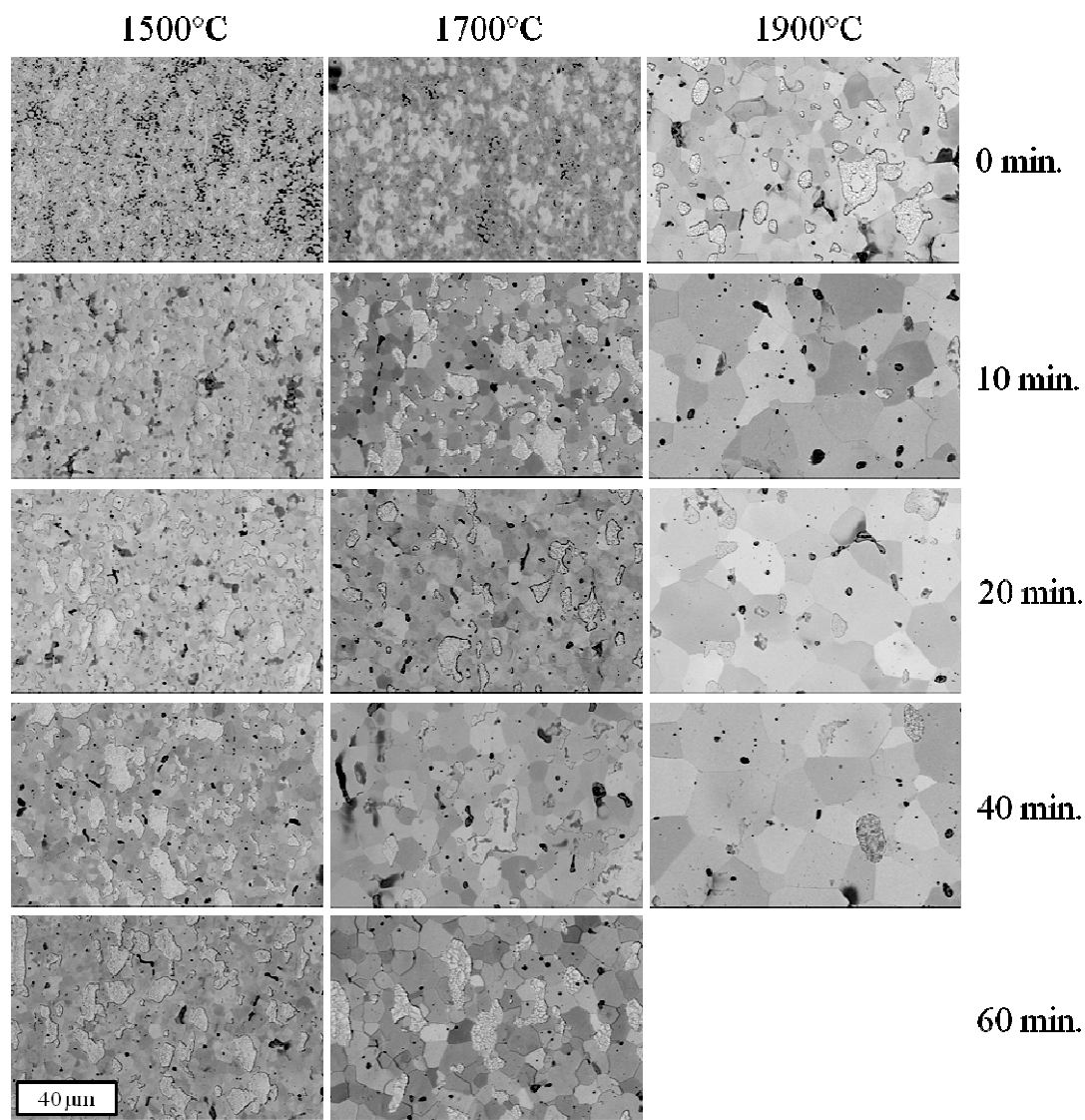
Figure 39. SEM/BSE images of blended samples consolidated at 1500, 1700, and 1900°C for 0 to 60 minutes (mag. = 2500 X)

The microstructures for the ball milled samples are shown in Figure 40. There is qualitatively less σ-phase in each sample relative to the blended samples. In addition to that, there appeared to be small but more numerous pores within the microstructures and also more variability in the overall grain sizes seen. The degree of grain relief from the etch was, again, somewhat inconsistent.

There is WO$_2$ present but not to the degree seen in the blended samples. The powders for the milled samples were reduced separately from the blended samples and their reduction process may have yielded fewer oxides. While the temperature, hold time, and N$_2$– 6 at% H$_2$ flow rate were constant, variables such as the amount of powders in the crucible, packing density of the powders, and powder depth could result in less oxide content. There may have also been less exposure during powder transfers. Another possibility is that if surface oxides were present after the reduction process, they would be distributed throughout the crystallites during the milling process.
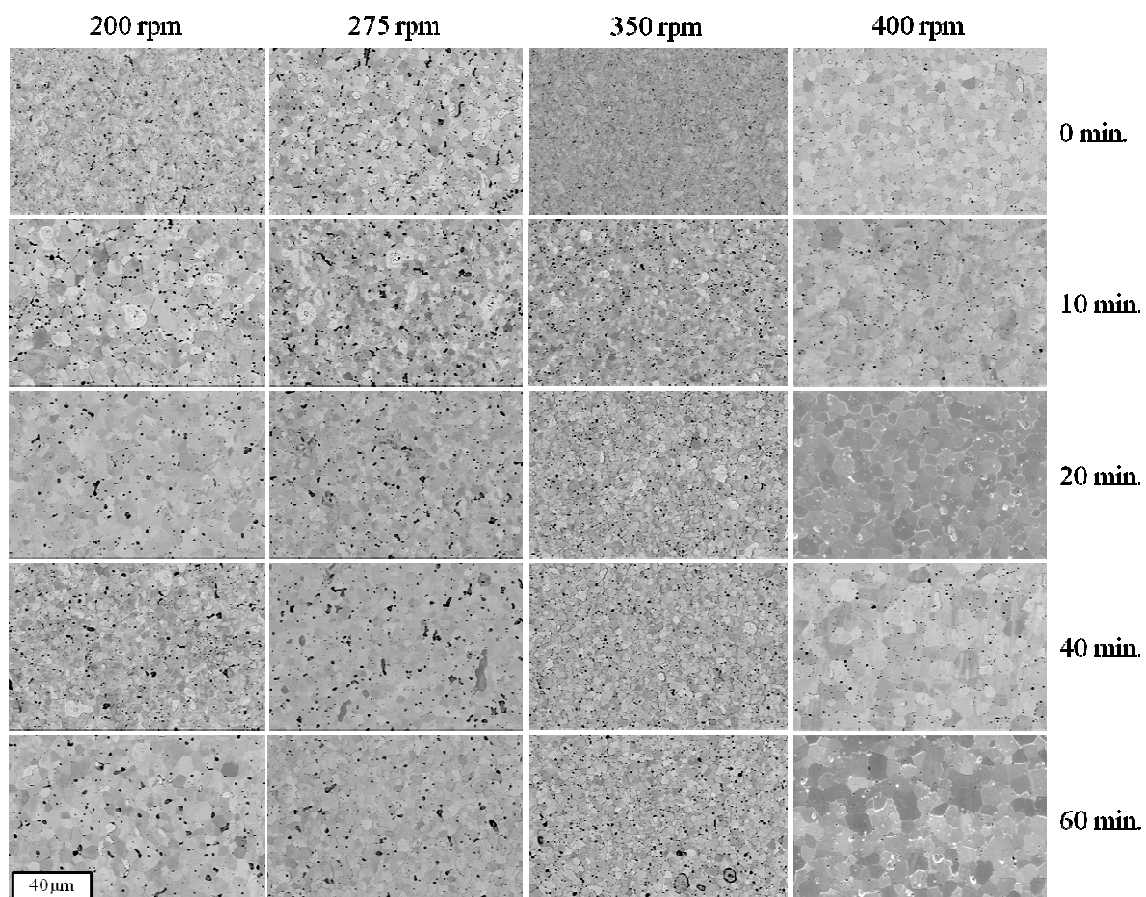
Figure 40. **SEM/BSE images of ball milled samples consolidated at 1700°C for 0 to 60 minutes (mag. = 2500 X)**

4.1.10 - XRD of Pellets

The XRD scans of each sample's cross section show a microstructure with no discernable rhenium peaks. However, in addition to the tungsten peaks, there were peaks that correlated with σ-phase.[57] Peaks for χ-phase or any contaminant phase were not detected. The scans for the 0, 10, 20, 40, and 60 minute dwell samples of the blended, 1700°C set are shown in Figure 41.
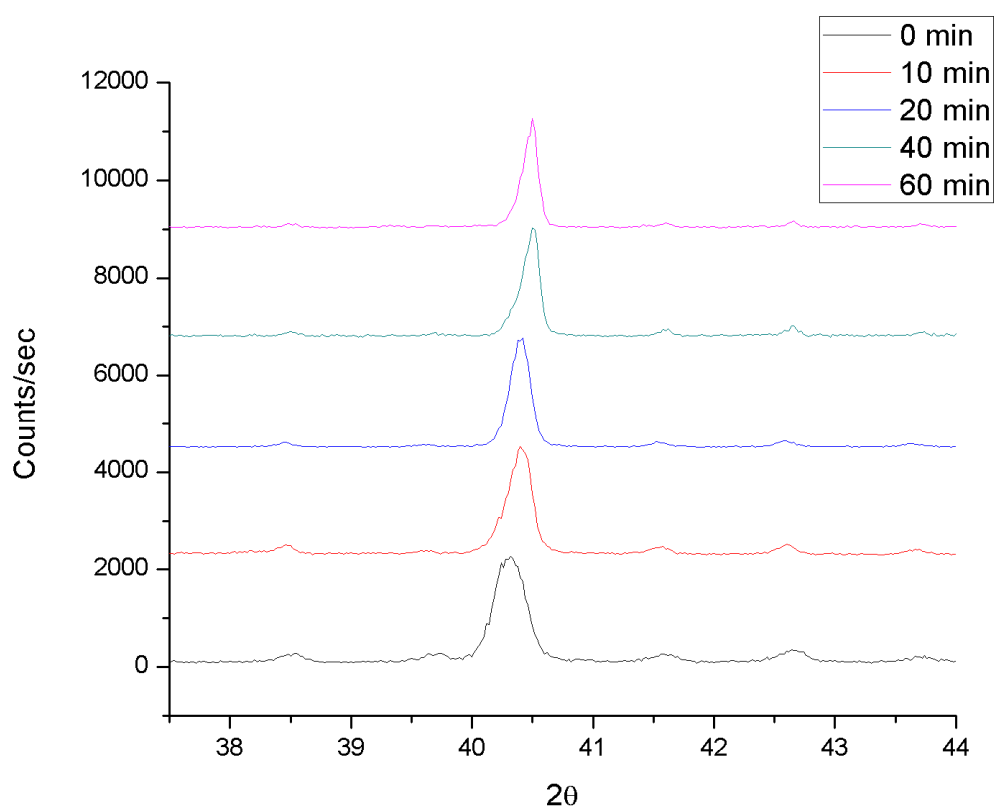
Figure 41.   XRD scans for the W-25 at% Re blended (1700°C) showing the 0-60 minute dwells; vertical lines indicate σ-phase [57]

These σ-phase peaks could be seen to decrease in amplitude with longer dwell times though never entirely disappearing. This can be seen in the same blended, 1700°C samples with their scans overlaid in Figure 42.
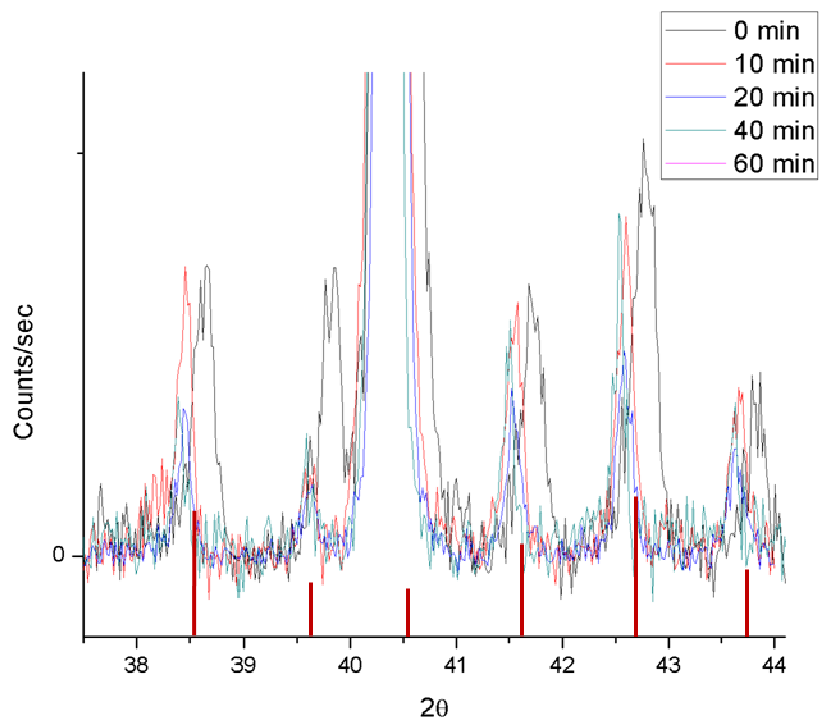
Figure 42.   Overlaid XRD scans for blended (1700°C) W-25 at% Re samples; vertical lines are σ-phase reference peaks.[57]

Not only did the σ-phase peaks decreases with longer dwell times but also with higher rotational energies from ball milling. An attempt at quantifying the amount of σ-phase and rate of dissolution using Reitvelt refinement; however, the results were unsatisfactory. To use this method, the atomic positions of each atom with the σ crystal structure must be known to accurately quantify the concentration within the

microstructure. Research has shown that these positions shift with changing tungsten and

rhenium content and this is sure to be occurring as interdiffusion occurs during the SPS.[6]
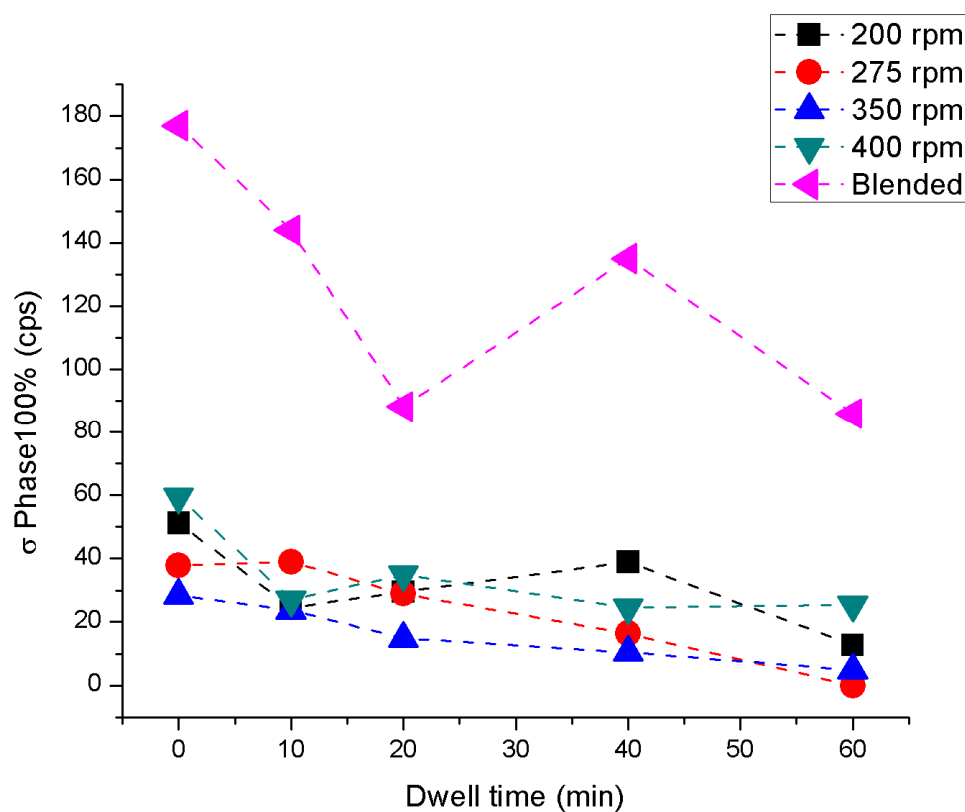
Figure 43. **The 100% peak intensity for σ-phase as a function of sintering dwell time for variable ball milled and blended (1700°C) samples**

4.1.11 - Intermetallic Content

The σ-phase area fraction for the blended samples seen in Figure 44 clearly shows

an inverse relationship between the sintering temperature and σ area fraction. The amount

of σ-phase at 1500°C is still forming during the first 10 minute dwell but decreasing

during the remaining 50 minute dwells. Besides reaching their hold temperature two and

four minutes prior to the 1700 and 1900°C samples, respectively, the σ phase content in

the 1500°C samples is also restricted by not being fully consolidated and thus having more pores and voids between particles. The densification for the 1500°C samples can be seen to come to an end after the first 10 minute dwell (Figure 34) and this transition point correlates well with the impending drop in σ-phase for the remaining dwell time. The 1700 and 1900°C samples are already decreasing in σ fraction during all of their dwell times. This would suggest that the rhenium phase had dissolved prior to reaching their hold temperatures.
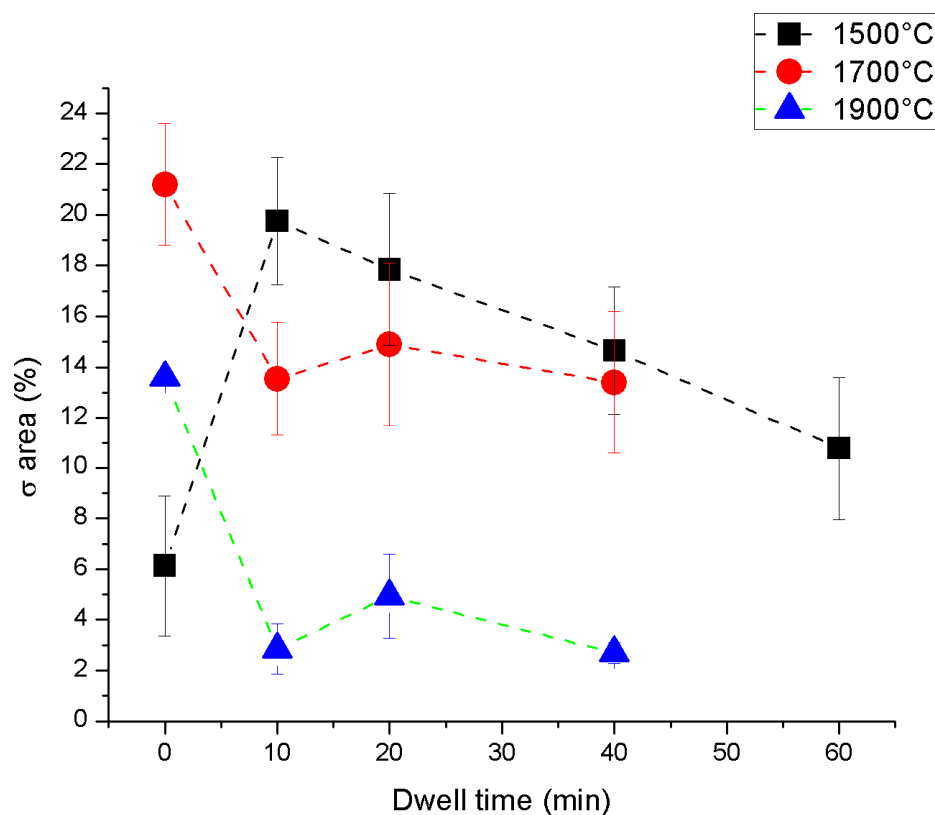
Figure 44. σ-phase area fraction as a function of SPS dwell time for the W-25 at% Re blended samples

The dissolution trends for σ-phase found for the blended samples correlate, to a large degree, with what was determined by Smith and Hehemann. Figure 45 shows a rough comparison between the σ-phase dissolution for the W-25 at% Re samples of this study and the W-5 at% Re of Smith and Hehemann's.[52] Of course, there are processing differences, such as the fact that their induction furnace could ramp and cool their W-Re samples to temperature in seconds, while using temperatures above the stability limit for χ-phase. That being said, the minutes long lag time of ramping to temperature difference between the two studies is not so large when considering the longer dwell times. There was also little to no χ-phase detected in the SPS samples indicating its formation and dissolution bear little effect on the dissolution of σ-phase once the hold temperatures are reached. With these caveats in mind, the σ-phase dissolution trends between the two studies seem reasonably comparable, even with such different temperatures utilized.
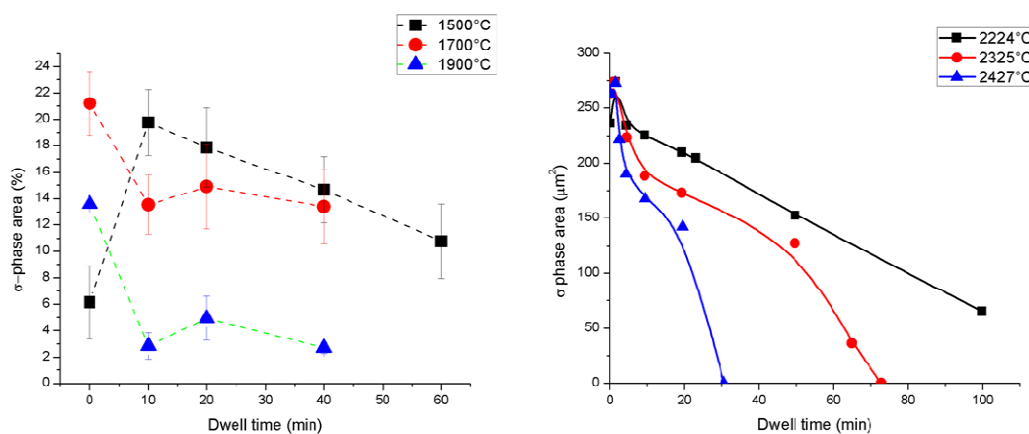
Figure 45.   σ-phase area content for blended samples (left) and the calculated area from σ-phase radii measured by Smith and Hehemann (right) as a function of sintering dwell time.[52]

The milled samples also show a drop in σ concentration with increasing dwell time but also an inverse correlation between milling energy and σ concentration. All milled samples were lower in σ content compared to the blended samples consolidated at the same temperature. And while there is a substantial reduction in σ-phase with milling, it should be noted that the greatest difference between the milling speeds is found in the first 20 minutes of the temperature dwell. After that, each set reaches a lower limit. The 400 rpm set seems to have reached that limit upon reaching its hold temperature and drops very little during the remaining dwell time. This would suggest that, regardless of milling speed, five hours is insufficient in milling time for reducing rhenium particle size and/or mechanically alloying tungsten and rhenium together.
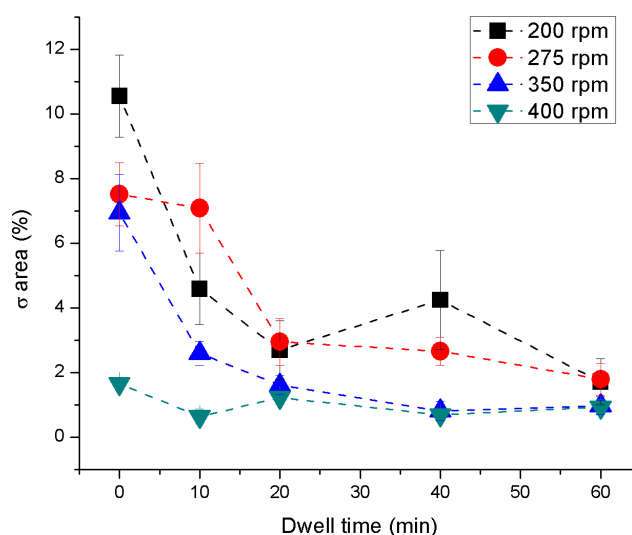
Figure 46.   σ-phase area content as a function of SPS dwell time for the W-25 at% Re milled samples

4.1.12 - Tungsten Grain Growth

The grain sizes for the blended samples show a definite relationship between the sintering temperatures and grain diameter, shown in Figure 47. While there was little difference between the 1500 and 1700°C samples, there was a substantial increase in grain growth between the 1700 and 1900°C sets. The 1500, 1700, and 1900°C samples appeared to reach a plateau grain size of approximately 3.9, 4.9, and 13.5 μm, respectively.
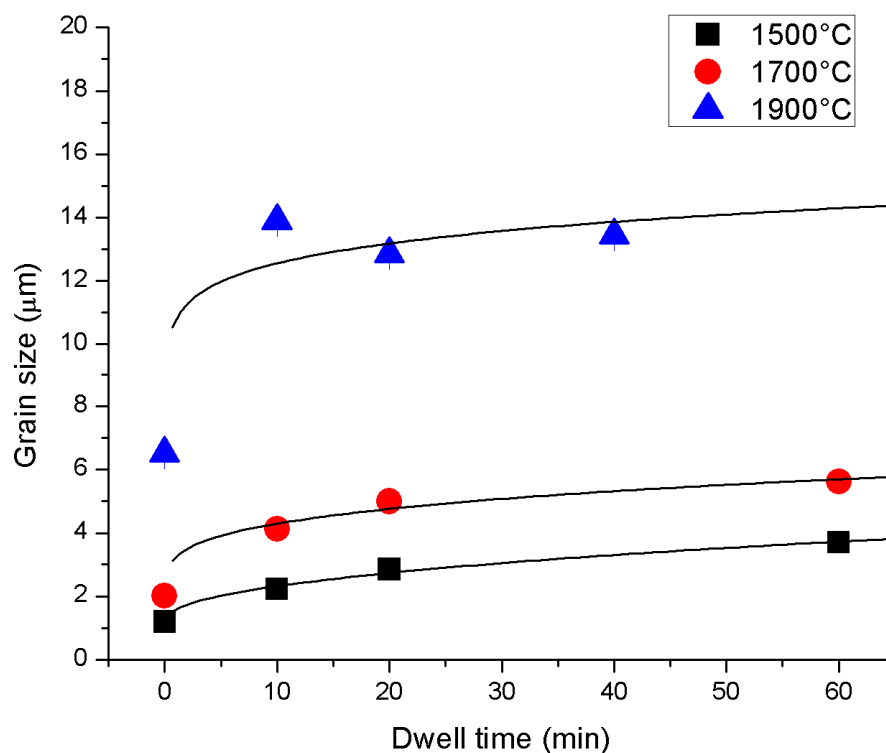
Figure 47. **Grain size as a function of SPS dwell time for the W-25 at% Re blended samples. The measurement error bars were obscured by the symbols so were not included.**

There were no discernible trends for the milled samples. The 275 rpm and 350 rpm samples reach a plateau a little over 2 µm while the 200 rpm and 400 rpm samples reached approximately 5 µm. This is not likely to be due to the error in measurement for the EBSD linear intercept measurements as multiple scans showed an error of approximately 0.13 µm for 3 scans of different areas. The variation seen is likely due to error within the fabrication process.
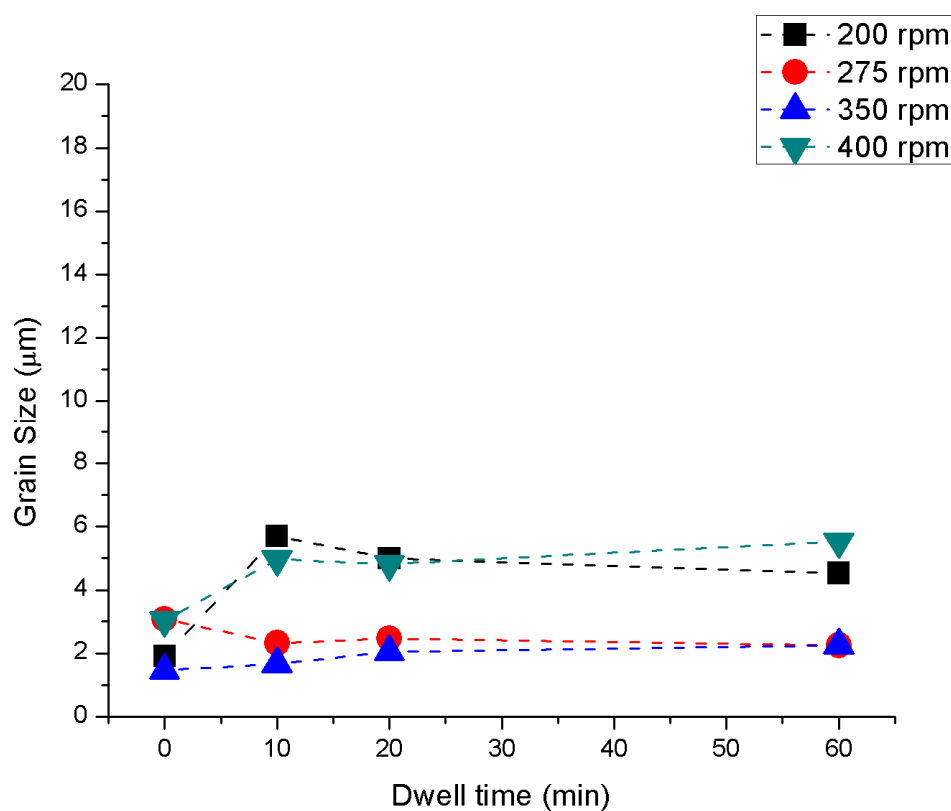
Figure 48.   Grain size as a function of SPS dwell time for the W-25 at% Re milled samples. The measurement error bars were obscured by the symbols so were not included.

4.1.13 - Hardness Values

The micro-indentation results show a decrease in Vickers hardness with longer sintering dwell time. This is likely due to a Hall-Petch type relationship as the grain sizes of the samples are increasing with longer time. The decrease in hardness for the blended sample is more severe than the milled samples and this likely due to the more dramatic drop in σ-phase in the blended samples than the 400 rpm milled sample. σ-phase is much harder than tungsten or rhenium and as it dissolves it results in a much lower average for each individual indent.[14]

The micro-indentation data also revealed a change in hardness values as a function of position in the specimen. With longer dwell times, there was a general drop in hardness at the edges of each sample's cross section relative to the hardness at the center of the sample. This can likely be attributed to the diffusion of carbon from the graphite paper surrounding the powders during the sintering process. This drop in hardness would also extend further into the microstructure with longer dwell times also suggesting the influx of carbon is responsible.
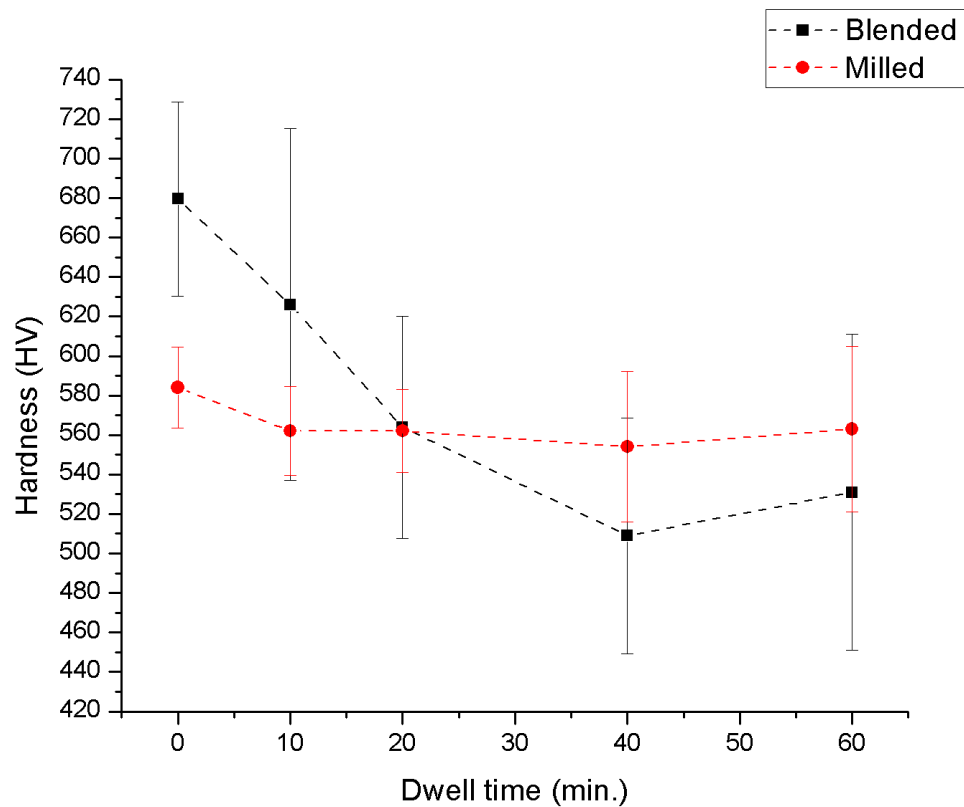
Figure 49.   Hardness as a function of SPS dwell time for the blended (1700°C) and the 400 rpm W-25 at% Re samples

4.1.14 - TEM and STEM/EDS

TEM bright field images showed different phases apart from the tungsten grains. The morphology of these structures differed from what was predominately seen with the SEM images (i.e. the periodic oxides at grain boundaries). One of these structures can be seen in the TEM bright field image in the center of Figure 50, which is a W-25 at% Re sample milled at 400 rpm and consolidated for 40 minutes.
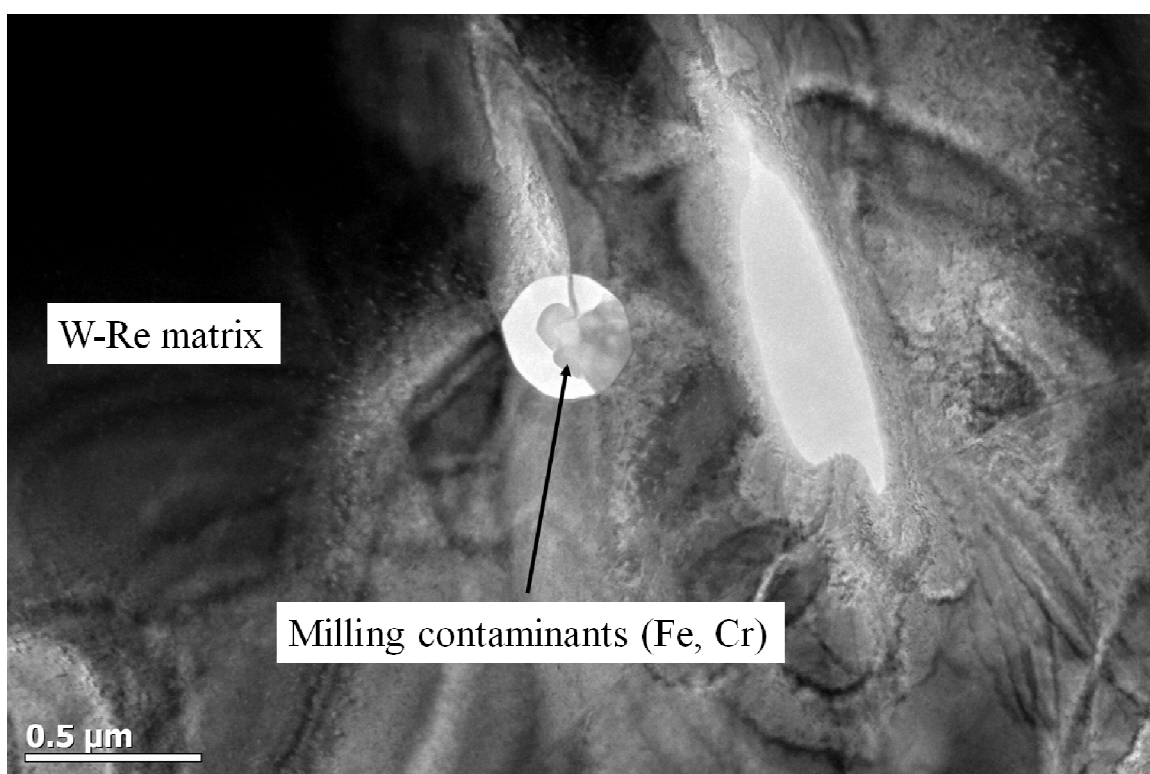
Figure 50.   TEM bright field image of W-25 at% Re milled at 400 rpm, consolidated at 1700°C for 40 min.

STEM/EDS results for Figure 50 showed predominantly tungsten with rhenium distributed uniformly throughout each grain. The measurement also showed copper (from the TEM grid support) along with iron, chromium, and oxygen sparsely distributed, but also localized at the different phase region. The STEM/EDS results in Figure 51 show the

even distribution of rhenium through the tungsten matrix and the Fe, Cr, and O elements at the grain boundaries. This contamination is likely due to the incorporation of material from the hardened steel milling vessel and residual oxygen present in the sintered powders. The X-ray spectra and elemental quantities from the EDS scan are shown in Figure 52 and Table 6, respectively.
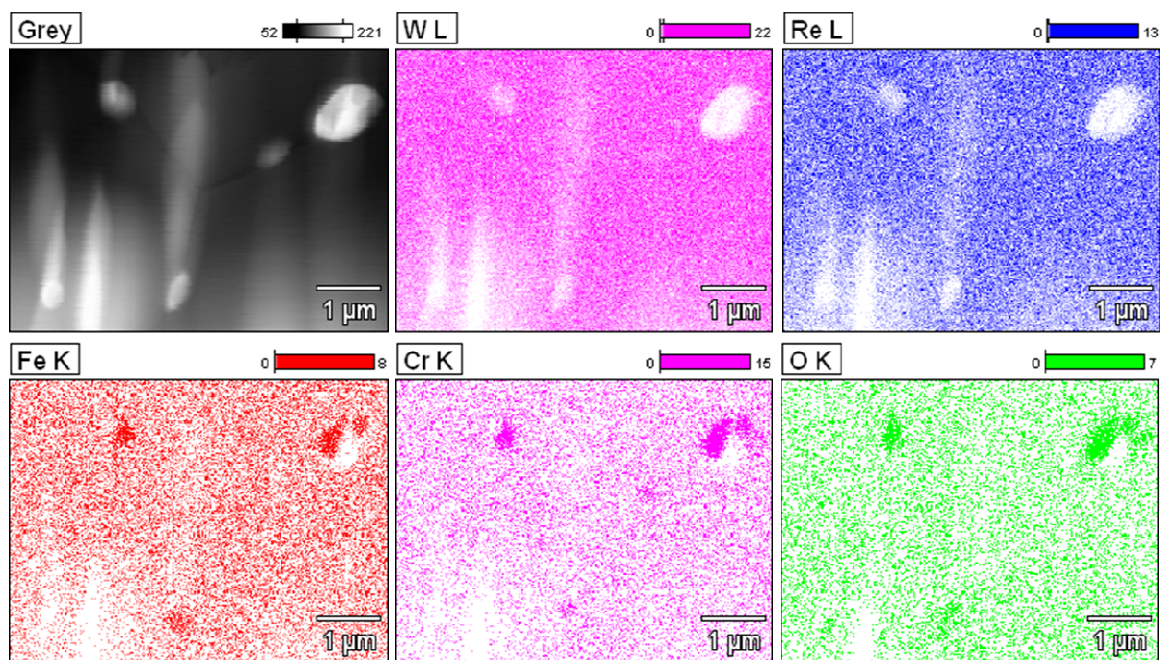
Figure 51.   STEM/EDS results for W-25 at% Re sample milled at 400 rpm, consolidated at 1700°C for 40 min.
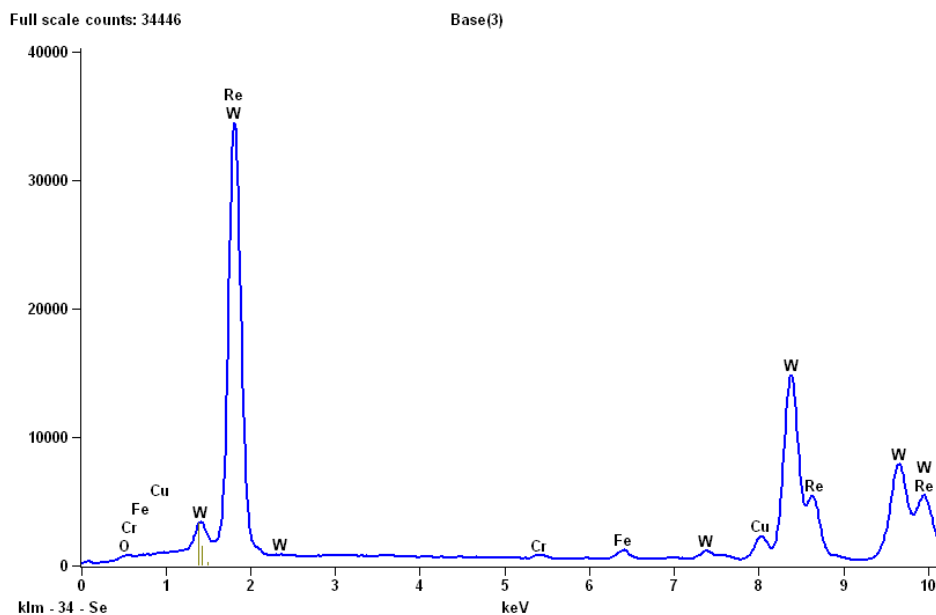
Figure 52.   X-Ray spectrum found during STEM/EDS scan

Table 6.   Elements found in STEM/EDS area scan

Element Line	Net Counts	Weight %	Atom %	Atom % Error
Cr K	5386	0.93	2.89	+/- 0.24
Fe K	14235	1.63	4.73	+/- 0.19
Cu K	42346	4	10.2	+/- 0.28
W L	552852	69.82	61.59	+/- 0.43
Re L	181911	23.63	20.58	+/- 0.28
Total		100	100	

4.1.15 - Contamination Effects from Media and Vessel

The SEM/EDS scans of the ball milled samples using the ISIS system showed

only slight deviations of the W/Re compositions and little else. However, the 400 rpm

samples picked up Fe concentrations ranging from 1.8 to 2.9 at% iron. Figure 53 shows

this iron content as a function of SPS dwell time. There were no contaminants found for

the 200, 275, and 350 rpm samples microstructures, however, the lower detection limit

for the ISIS EDS system is a little over 1 at%. The STEM/EDS also showed occasional

Fe/Cr rich precipitates with one area scan showing 2.9 at% and 4.7 at% for Cr and Fe,

respectively. The source of this contamination is very likely the hardened steel milling

vessel. While this level of contamination is within the very wide range seen in the

literature mentioned in the background section, it is still undesirable.
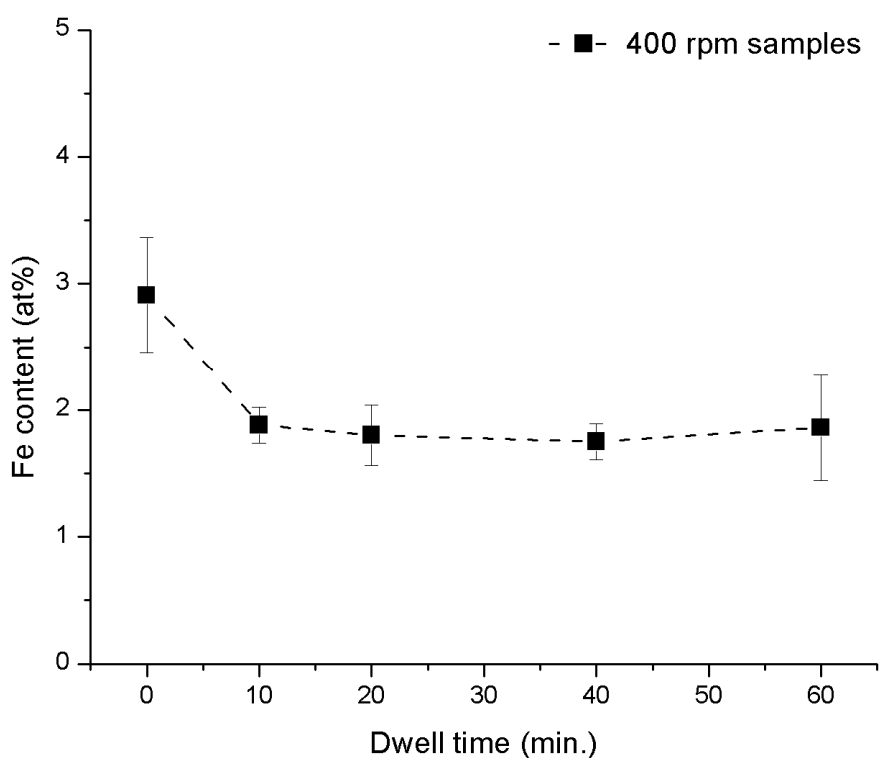
Figure 53.   Fe at% as a function of SPS dwell time determined through EDS

4.1.16 - Determination of Optimized Parameters

4.1.16.1 - SPS Temperature and Dwell Time

The variation of SPS temperature on the W-25 at% Re samples showed that:

- high densities were achieved regardless of temperature

- grain growth dramatically increased when sintered at 1900°C

- σ-phase content substantially decreased at 1900°C while the decrease for 1500°C and 1700°C was not as large

- the attrition rate for the graphite punches was much higher for the 1900°C samples as the current densities needed to achieve that hold temperature typically caused the punches to deform

Given this information, the ideal temperature for the optimized samples was chosen to be 1800°C. This was a desired balance of the higher dissolution rates seen above 1700°C but a lower degree of grain growth seen in the 1900°C samples. Also, previous sintering studies at BSU had shown that the current densities typically required to reach an 1800°C hold temperature resulted in significantly less damage to the graphite punches. The AXF-5Q punches would routinely hold up without chipping or buckling even with hold times as long as 60 minutes.

The sintering dwell times showed that:

- other than the 10 minute dwell for the 1500°C temperature, densification did not increase with longer dwell times

- most σ-phase dissolution occurred within the first 20 minutes

- grain growth was non-linear with most growth occurring within the first 10-20 minutes

Given this information, the ideal dwell time for the optimized samples was limited to a 30 minute dwell. Sintering for longer than that amount of time would yield minimal

gains in regards to σ dissolution while suffering carbon diffusion contamination and punch degradation. Dwell times of 0 and 15 minutes were also chosen to evaluate microstructural trends for the optimized samples.

The ramp rate and pressure variables were kept constant. While an increased ramp rate would lower the overall process time, the current required to increase the temperature to 1800°C is much higher and would result in a higher punch attrition rate. Higher pressures might restrict grain growth for the optimized samples but at the very high processing temperatures used there was, again, concern for the stability of the graphite punches. The optimized SPS parameters are shown in Table 7.

Table 7.   Optimized parameters for SPS powder consolidation of W-25 at% Re

Temperature	*Time*	*Ramp Rate*	*Pressure*	*Atmosphere*
1800°C	30 min.	100°C/min	42.4 MPa	Low Vac.

4.1.16.2 - Milling Speed and Time

The variable milling energy results showed that:

- increasing the milling energy from 200 rpm to 400 rpm decreased the σ area content considerably,

- the decrease in σ-phase from higher milling energies only went so far with a 5 hour mill time; none of the variable milling energy samples were without σ-phase, regardless of dwell time, and this is likely due to large rhenium particles that were not sufficiently fractured and distributed during milling,

- the reduction of rhenium crystallite size and/or degree of alloying with tungsten can be qualitatively monitored with XRD,

- increased milling energies resulted in contamination from the milling vessel with the higher density media and possible lack of powder coverage within the jar likely to blame.

Given this information, the optimized milling parameters were determined to involve:

- changing the milling vessel to a WC material to match the media hardness values and reduce powder contamination,

- milling at 400 rpm, while periodically monitoring the reduction in peak amplitude for the rhenium XRD peaks,

- using a higher powder charge, which would likely better shield the vessel walls from the impacting media. The powder will also be periodically scraped and dislodged between milling intervals to ensure that areas that receive fewer impacts from the media (such as the region where the lid and jar join) are properly milled.

These optimized milling parameters are more qualitative than those determined for the SPS parameters, particularly the milling time. The monitoring of the rhenium peaks during milling is a balance of σ-phase dissolution and contamination effects. While a complete removal of the 100% rhenium peak would be an indicator favorable to minimal σ-phase content, the milling contamination may be unacceptable. The ideal approach is to evaluate the peaks and, when an agreeable peak amplitude is achieved, sinter the milled W-25 at% Re powders using the SPS optimized parameters. If σ has not

dissolved, longer milling is required. For these optimized parameters, preliminary milling of W-25 at% Re was found to be eliminated with 30 hours of milling (25 effective hours given the 5:1 duty cycle used). The optimized ball milling parameters are shown in Table 8.

Table 8. **Optimized parameters for high-energy ball milling process of W-25 at% Re**

Speed	*Time*	*Vessel type*	*Powder Mass*	*Charge*
400 rpm	30 hrs	WC-6Co	60.0 g	3.89

4.2 - Optimized Samples

4.2.1 - Particle Size Distribution For Optimized Powders

The particle size distribution for the optimized samples follows a similar trend relative to the variable milling speed samples. The distributions, seen in Figure 54, show a decrease in the average size of particles with lower rhenium concentrations. This correlates with the first experimental PSD results in that there is less of the larger diameter rhenium to be welded to the tungsten particles, increasing the measured particle average. This can be seen with the shift of the peak position at approximately 1.4 μm to 3.5 μm for the W-3 at% Re to W-25 at % Re, respectively.
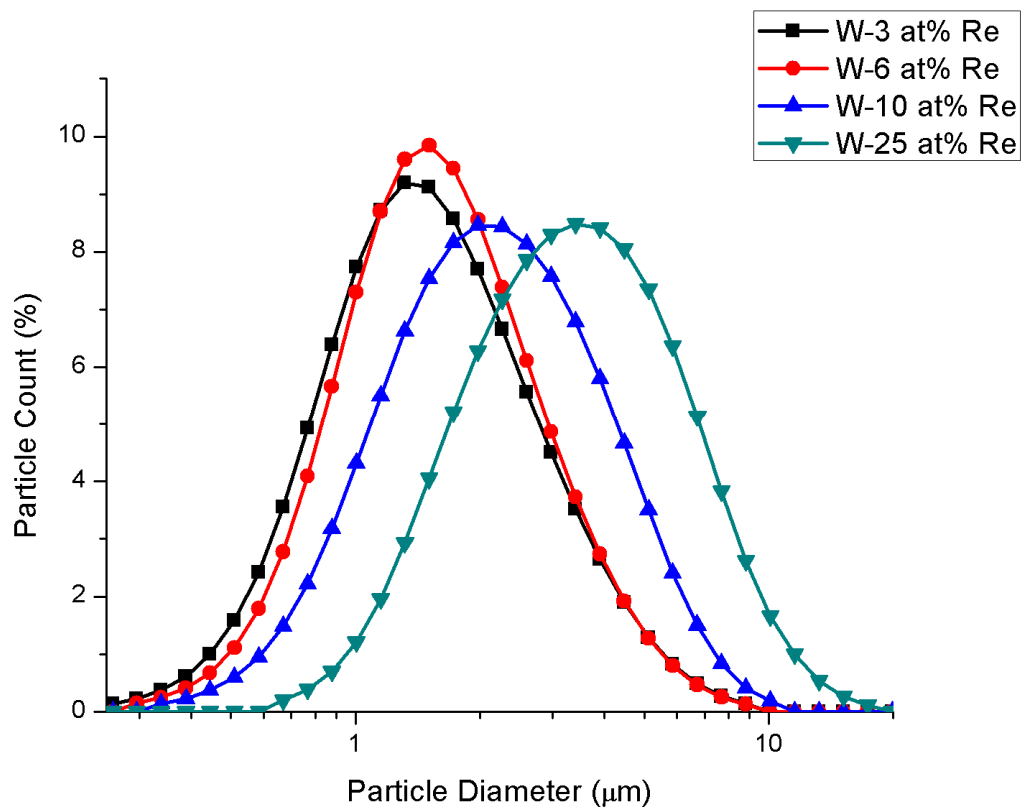
Figure 54.   **Particle size distributions for the optimized W-xRe powders milled for 30 h**

This peak position for the W-25 at% Re particles is quite close to the peak value for the 400 rpm distribution milled 5 h. However, it can be seen in Figure 55 that the 30 h milling time is skewed further right than the 5 h milling time. This suggests that more rhenium was incorporated with the longer milling time. This should be beneficial to homogenizing the alloy and reducing the amount of σ-phase in the microstructure.
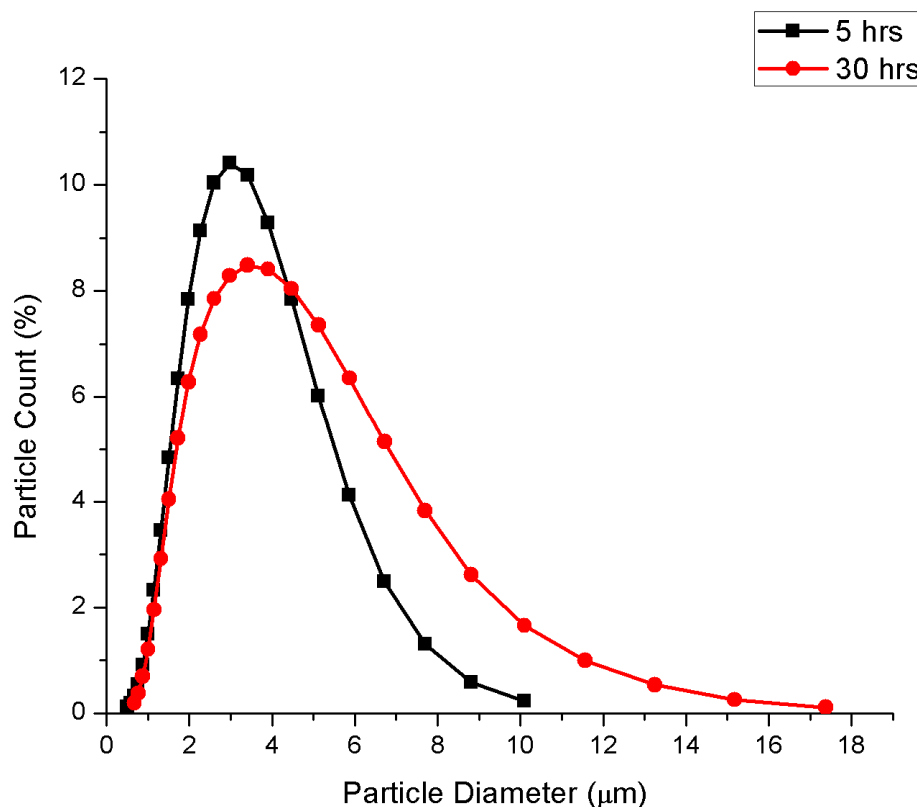
Figure 55. **Comparison of particle size distributions for W-25 at% Re milled 5 hrs and 30 hrs**

4.2.2 - SEM Analysis of Optimized Powders

The SEM characterization seen in Figure 56 shows a consistent, rounded morphology of the powders. The average size of the powders also appeared to decrease with lower rhenium concentrations in the other compositional sets. The particle size analysis confirmed this, showing that milling with less rhenium decreased the mean size of the milled powders. The higher rhenium content powders were also seen to be more homogeneous in size with a more rounded morphology.
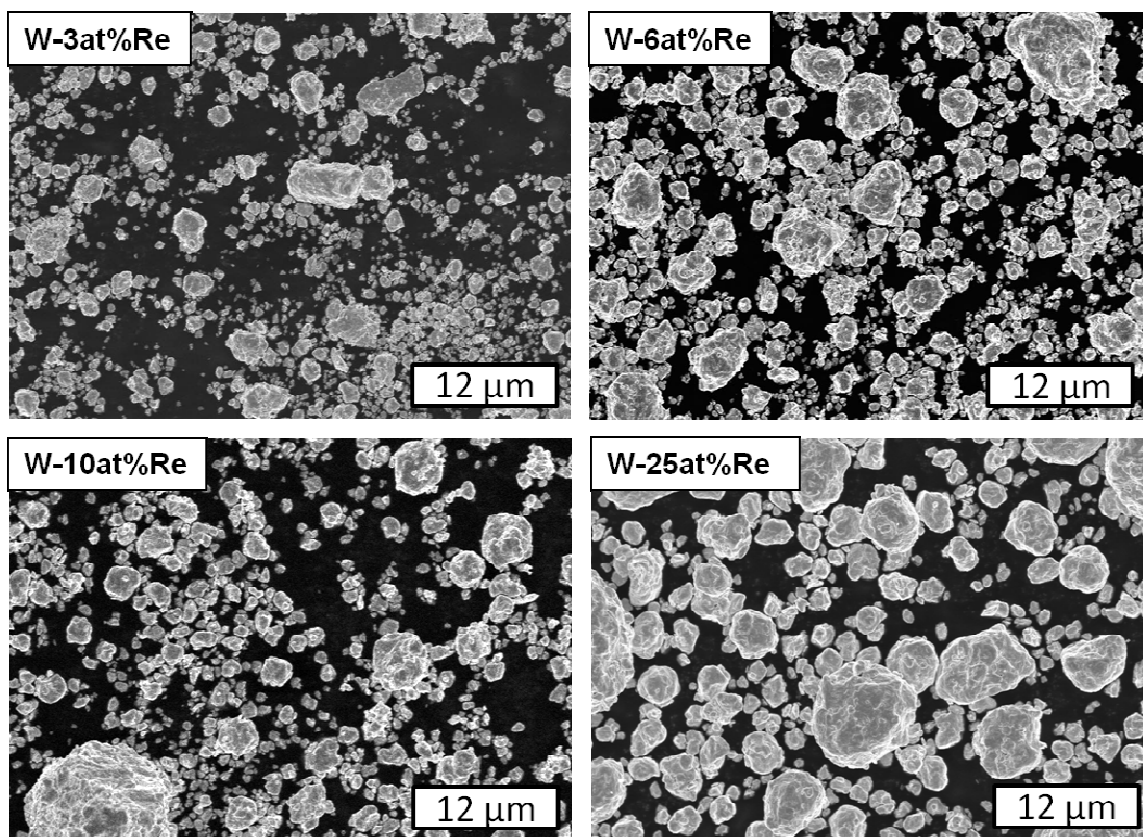
Figure 56.   SEM images of the optimized W-xRe powders

<u>4.2.3 - XRD of Powders</u>

The initial W-25 at% Re powders sets were milled in increments of 10 h until the 100% rhenium peak had been significantly reduced relative to the 100% tungsten peaks (Figure 57). The milling was halted after 30 h due to concern about rhenium adherence to the milling media and vessel. Further milling would also likely increase the overall porosity of the sintered compacts due to increasing crystalline defects in the milled powders while also increasing the contamination from the milling process.
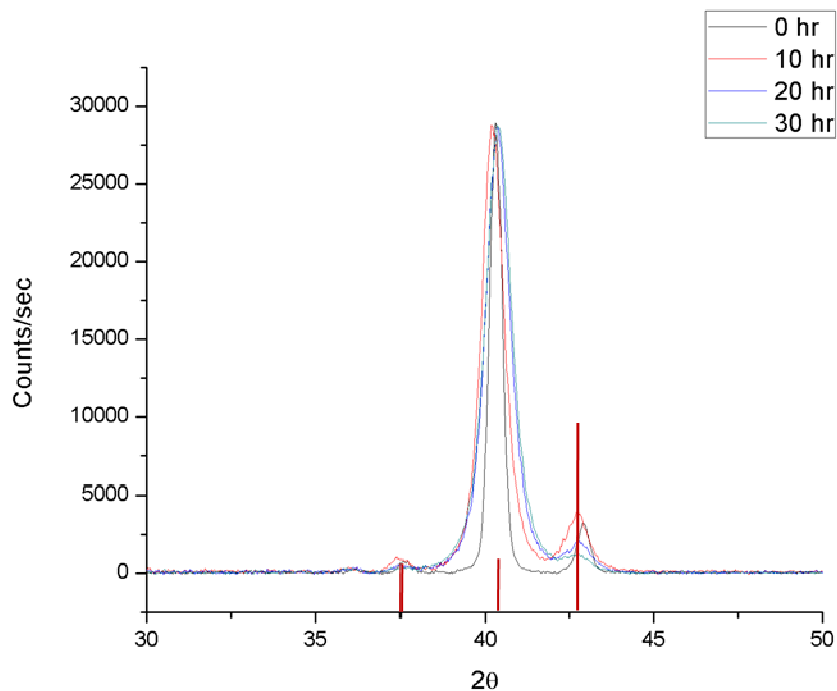
Figure 57.   XRD scans for W-25 at% Re powders milled 0, 10, 20, and 30 hours; vertical lines indicate rhenium peaks.[37]

It is expected for the 2θ values to increase with the addition of rhenium as the lattice parameter for tungsten will decrease from 3.165 Å to 3.145 Å when 25 at% rhenium is brought into solid solution.[9] This can be seen in Figure 58 where the tungsten 100% peak shifts approximately 0.2524 Å decrease after milling 30 h.
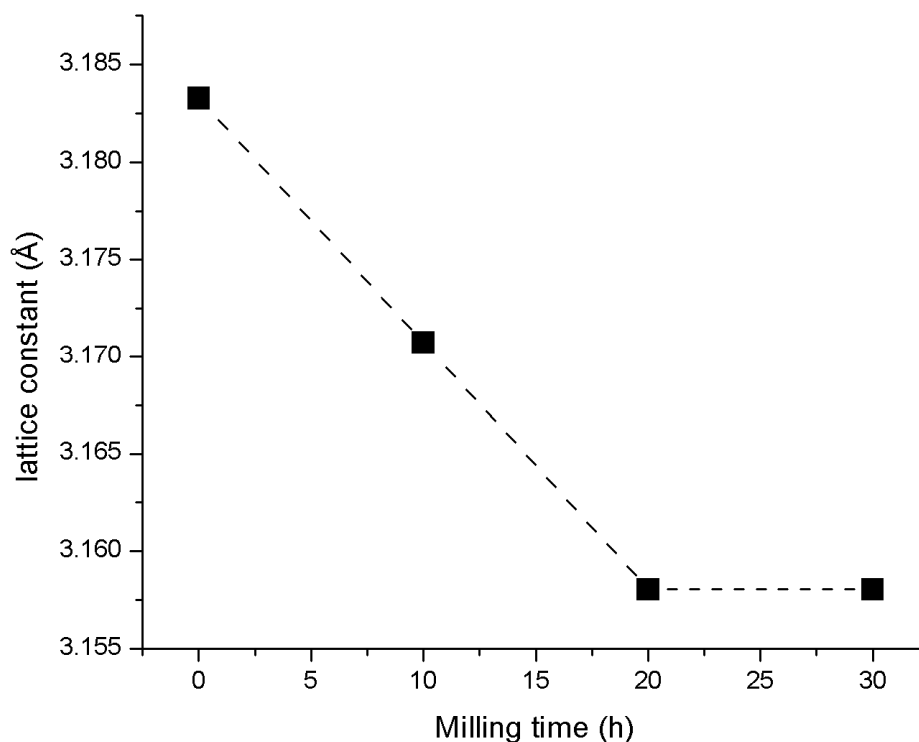
Figure 58.   **Lattice constant of W100% peak of W-25 at% Re as a function of milling time**

The milled powders were imaged conventionally with SEM and with secondary and backscatter detection. A large portion of the powders appear to be crystallites embedded in larger particles as can be seen in the SEM image in the top left of Figure 59. However, a significant number of particles exhibited the layering effect seen in literature for a brittle/ductile system. Both the embedded and layered powder types would be expected to enhance the homogenization in the alloy as there would be more diffusion channels from crystalline deformation and by decreasing the diffusional pathway from the center of a rhenium crystal to its surrounding tungsten matrix.
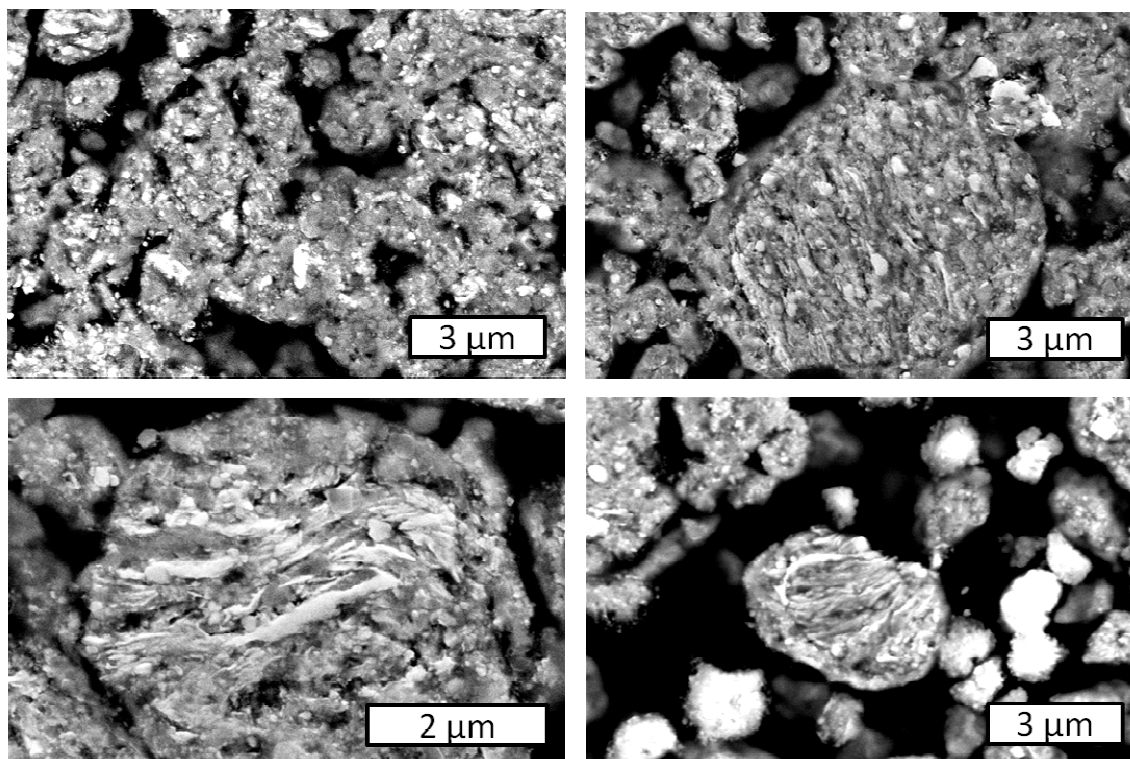
Figure 59.   **SEM images of optimized W-25 at% Re powders milled 30 hours showing embedded combinations (top left) and layered powders (remaining images)**

4.2.4 - Density Trends

The density of the optimized samples showed a definite trend of lower densities with lower concentrations of rhenium (Figure 60). This density drop as a function of composition is due to both the greater difficulty in sintering powders with higher concentrations of tungsten (with its higher T_m) and also the lower theoretical densities relative to lower rhenium concentrations. There was also a similar trend of decreasing density with longer dwell times as was seen with the variable temperature and milling speed samples from the first experimental set. Again, this is attributed to an influx of carbon from the graphite paper causing a higher degree of porosity at each sample's edges.
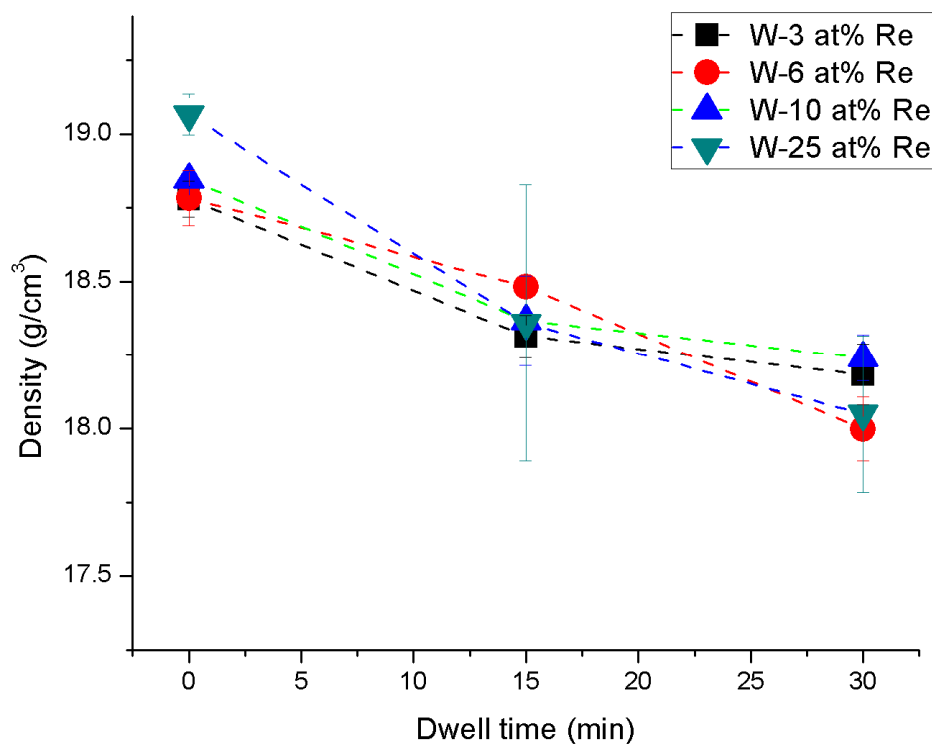
Figure 60.   Density of optimized W-xRe samples as a function of SPS dwell time

4.2.5 - Porosity

There were no discernible trends with the porosity results of each compositional

set. The variation seen in Figure 61 is very likely simply due to statistical variations for

each compositional set. Regardless, these porosity values found in the bulk of the

optimized samples do not correlate with the decrease in density measured as a function of

SPS dwell time.
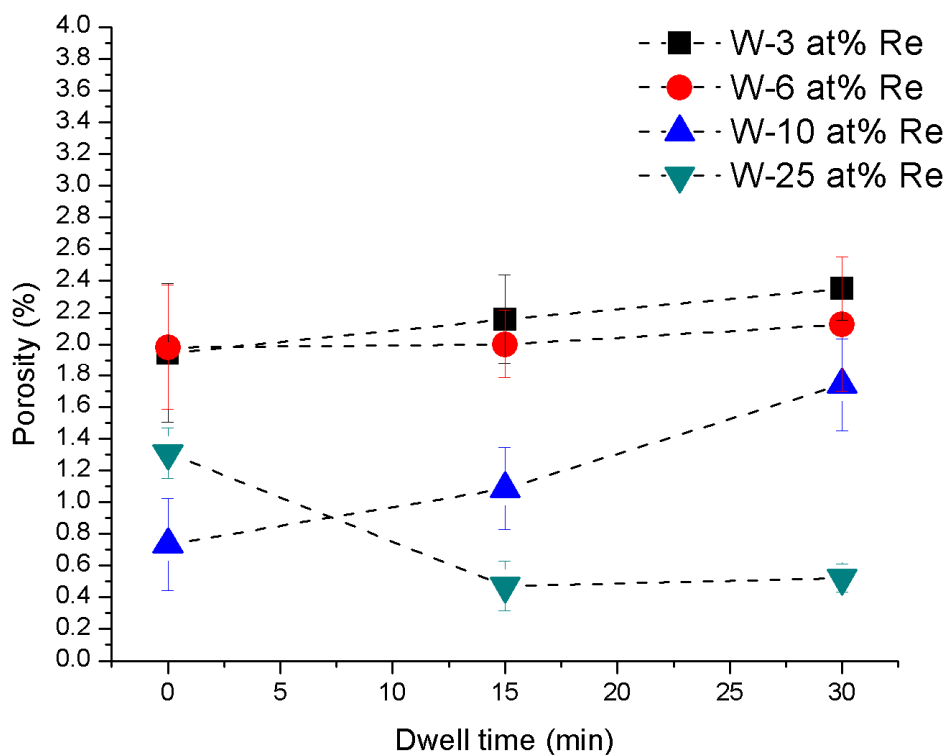
Figure 61. **Porosity in optimized W-xRe samples as a function of SPS dwell time**

Ignoring crystal defects such as vacancies and dislocations, these porosity values can be thought of as complementary to density resulting in calculated density values ranging from 97.7 to 99.5% theoretically dense for all optimized compositions. The difference between the inferred density from porosity measurements in the center of each sample and the densities measured with Archimedes is shown in Figure 62. It can be seen that each compositional set maintains its density with longer dwell and this value is near theoretical densities for each compositional set.
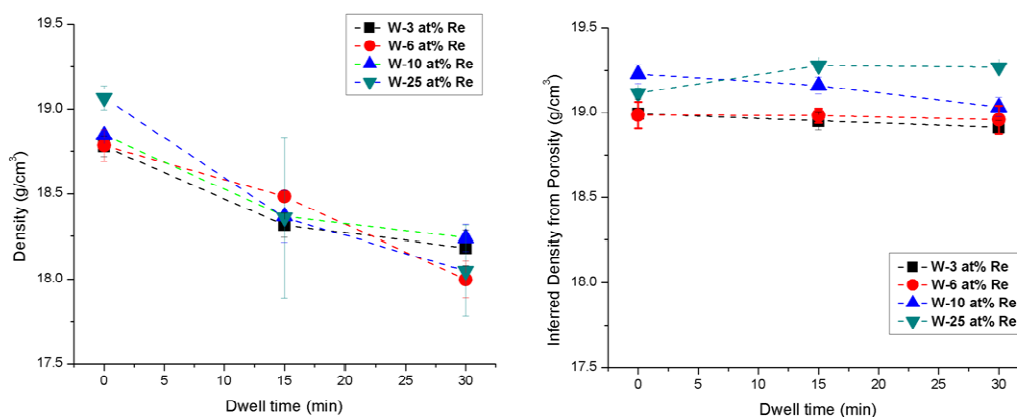
Figure 62. **Measured density (left) and density inferred from porosity measurements (right) for optimized W-xRe samples**

<u>4.2.6 - Displacement Curves</u>

The ram displacement for the optimized samples differs from the variable temperature and milling speed samples in two distinct aspects. The total displacement for each composition is smaller but almost theoretical densities are achieved nonetheless. This suggests that the beginning packing density was higher. This is likely the case, as the milled powders would visually appear denser and also occupy less space in the glass vials used for transporting them to CAES. The blended and, to a lesser extent, variable milling speed samples were less compact and settled within their containers to a higher degree.

The second difference seen in the displacement data for the optimized samples was the displacement rate. Figure 63 shows that the displacement rates modeled from the displacement values using a sigmoid function for all compositions were smaller than both the variable temperature and milling speed samples. The differences between the compositions in regards to both displacement and displacement rate showed no

discernible trends. It would be expected that a higher rhenium concentrations would yield both a higher degree of displacement and higher displacement rate given the lower melting temperature of rhenium but that was not discernible.
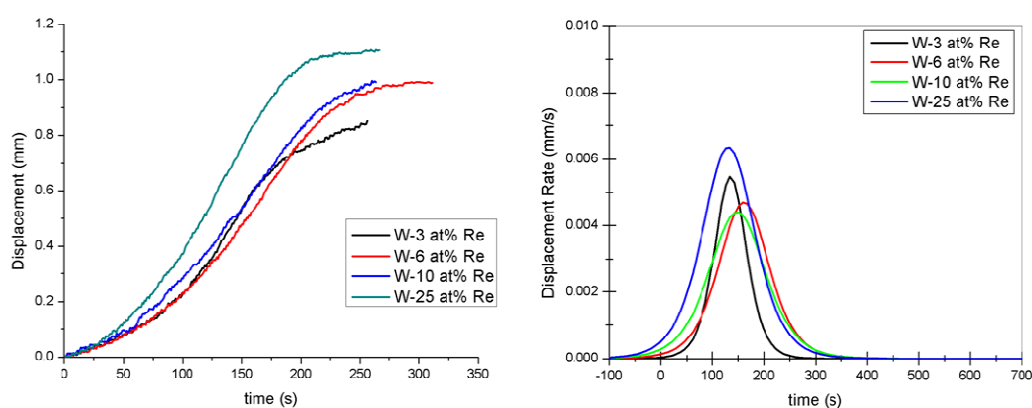
Figure 63.   SPS ram displacement (left) and modeled displacement rate (right) as a function of sintering time for the optimized W-xRe samples

4.2.7 - Shrinkage Model

The shrinkage model was again used to evaluate the possible sintering mechanisms and activation energies involved with the sintering process. The relation between logarithmic shrinkage and inverse temperature along with the linear components of each composition are shown in Figure 64. The resulting activation energies and mechanisms calculated from these slopes are listed in Table 9.
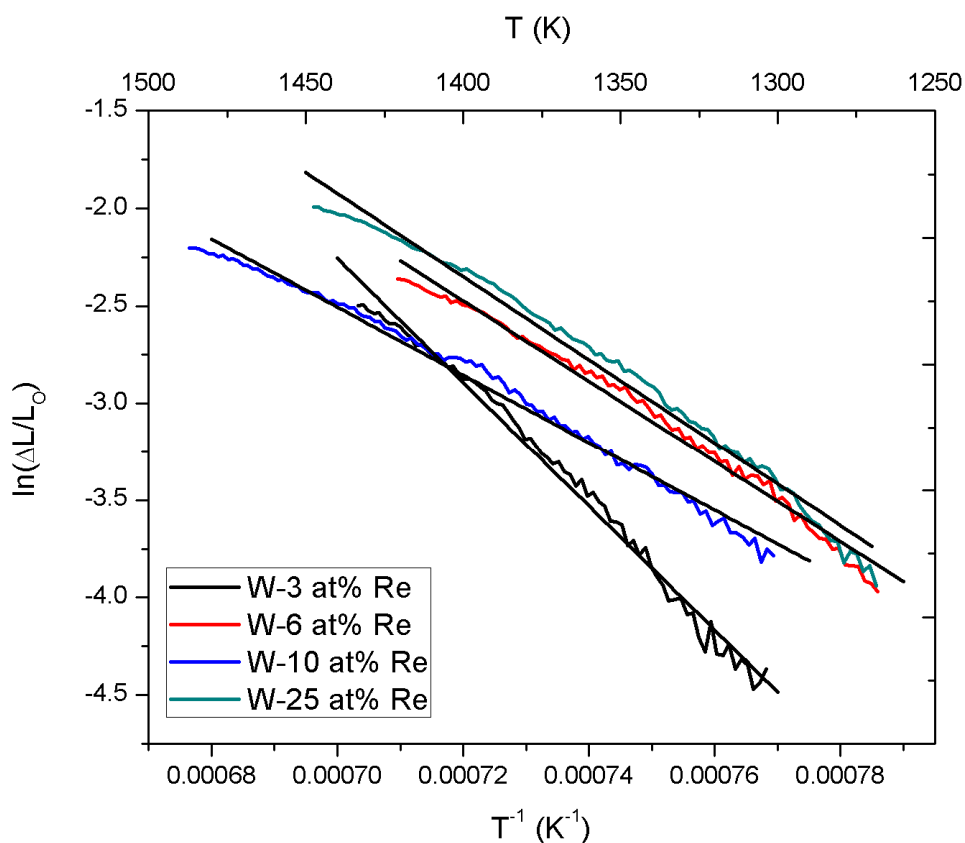
Figure 64.   Logarithmic shrinkage as a function of inverse temperature for the optimized W-xRe samples

Table 9.   Potential activation energies and mechanisms from shrinkage data for the optimized W-xRe samples

	Slope	*(Vol. Diff.)* **n = 5 (kJ/mol)**	*(GB Diff.)* **n = 6 (kJ/mol)**	*(Surface diff.)* **n = 7 (kJ/mol)**
W-3 at% Re	31850	660	790	930
W-6 at% Re	20636	430	510	600
W-10 at% Re	17419	360	430	510
W-25 at% Re	21325	440	532	620

The slopes found for the various compositions are higher in magnitude when compared to the variable temperature and milling speed samples. For all inferred mechanisms (surface, grain boundary, and volume diffusion), the values show a trend of

increasing activation energy values as a function of milling time. This can be seen in Figure 65 where the values calculated for grain boundary diffusion for the variable temperature (blended), variable milled, and optimized samples are shown. As each mechanism scales relative to the value of n used, grain boundary diffusion was simply chosen as an example, not as the determined mechanism. This increase in calculated activation energy from the blended to milled for 5 and 30 hours is thought to be due to a higher degree of mass-transpot mechanisms capable of occurring with higher milling time. The defects that occur during milling would present more diffusional pathways the both crystal structure types, resulting in more volume diffusion at similar temperatures. The values for the optimized W-3 at% Re, W-6 at% Re, and W-10 at% Re further compound the differences, with the contribution from a higher concentration of tungsten changing the mechanisms occurring during the sintering process. The variation between these compositions and the W-25 at% Re sets can also be seen in Figure 65.
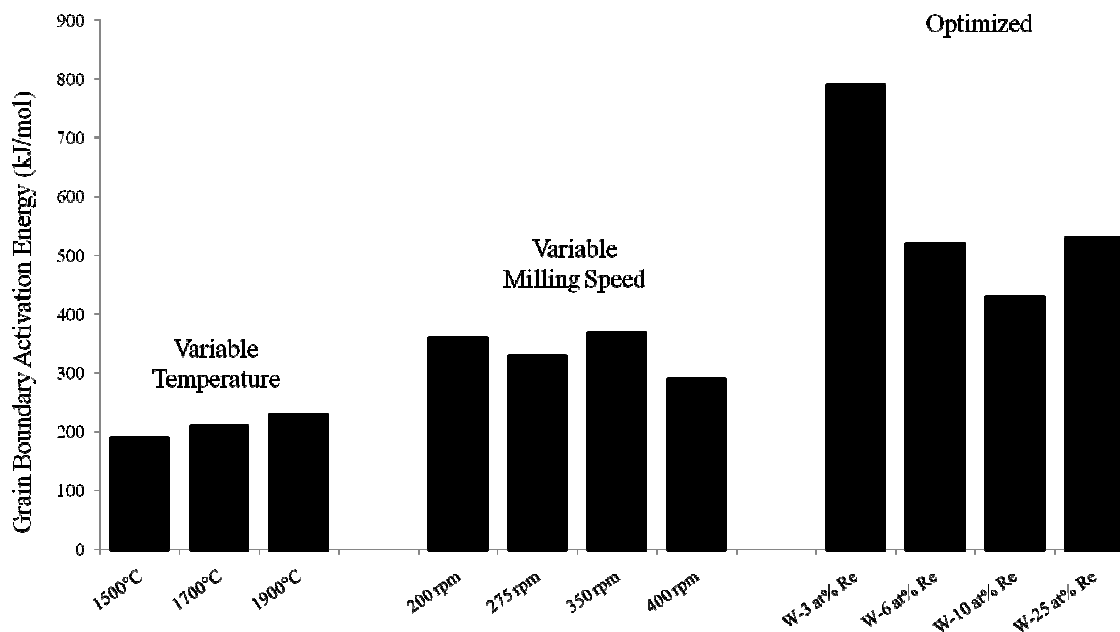
Figure 65. Inferred grain boundary activation energies for the variable temperature, milling speed and optimized samples

4.2.8 - Microstructure

The microstructures of the optimized samples for the four different W-Re compositions are shown in Figure 66. The blended and milled samples from the previous experimental section were evaluated using the backscatter detector; however, the resolution was not sufficient to detect the smaller σ-phase particles in the optimized samples so the higher resolution secondary electron detector was used for quantification. The σ-phase was differentiated from the tungsten matrix by identifying the particles with smooth and regressed grain boundaries as opposed to contrast differences as seen with the backscatter detector. The SEM images show a noticeable increase in grain size with longer dwells and decreases in rhenium content. The grains can also be seen to become more ridged and jutted with a decrease in rhenium content. The optimized microstructure

looks more homogeneous, more compact, and having cleaner grain boundaries when compared to the samples from the first experimental set.
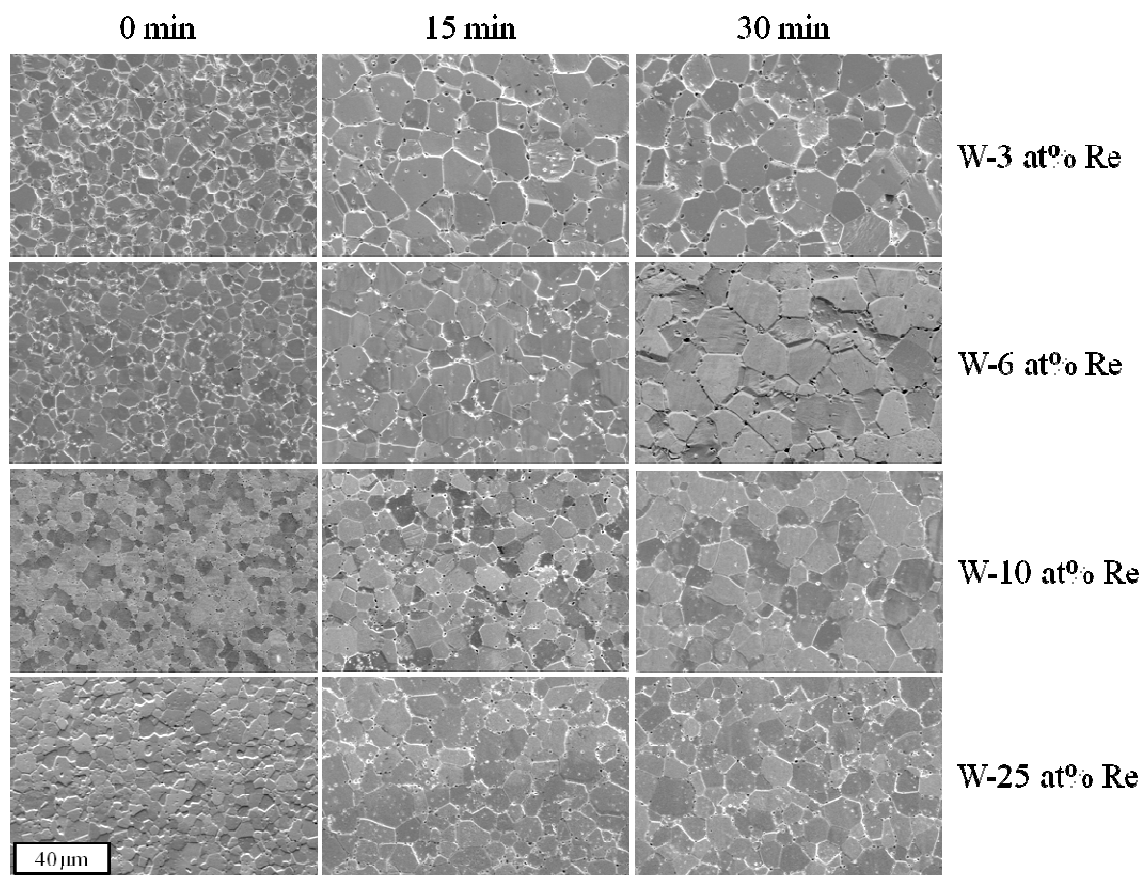
Figure 66. **SEM images of optimized samples consolidated at 1800°C for 0 to 30 minutes (mag. = 2500 X)**

4.2.9 - EBSD

The EBSD scans for the optimized samples were of a much better quality than the blended and milled samples from the first experimental section. The optimized samples were single phase, resulting in cross sections that polished and etched more uniformly, which is critical to producing quality kikuchi bands. The inverse pole figure maps for the W-3 at% Re and W-25 at% Re samples are shown in Figure 67.
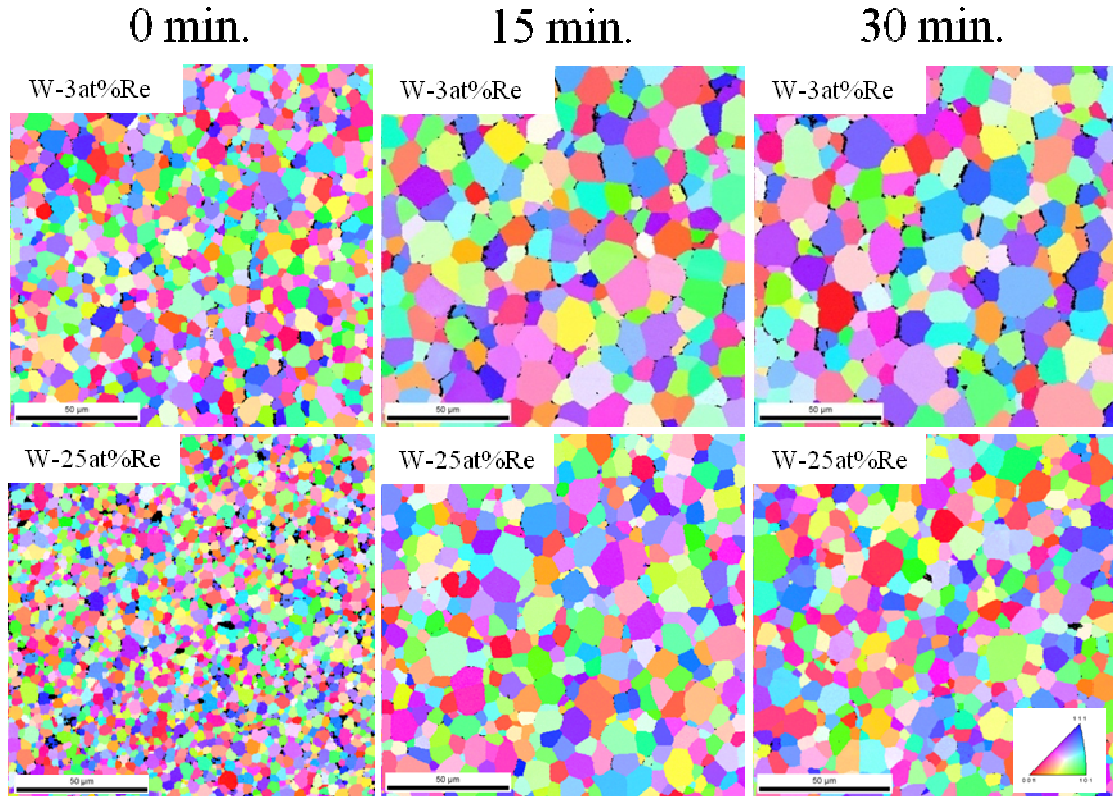
Figure 67. EBSD inverse pole figure maps of W-3 at% Re and W-25 at% Re samples consolidated at 1800°C for 0 to 30 min.

The scans on these samples showed that there is no preferred orientation to the W-Re grains, that the samples are single phase (tungsten BCC), and shows an increase in grain growth with lower rhenium concentrations. There was a slight aspect ratio of 0.57 to the grains, being more elongated normal to the current and pressure from the punches. The grain orientation and aspect ratio for a scan of a W-25 at% Re sample is shown in Figure 68.
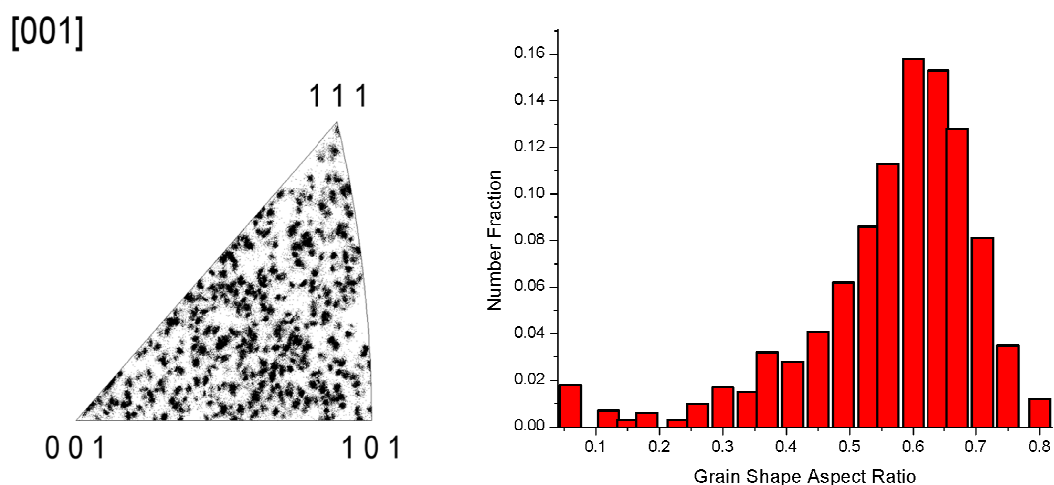
Figure 68. **Inverse pole figure (left) and grain shape aspect ratio (right) for W-25 at% Re sample**

4.2.10 - XRD of Pellets

The XRD characterization of the optimized, consolidated samples detected neither the σ, χ, or rhenium phases (Figure 69). There were also no contaminant phases to be found; only the tungsten BCC phase (and mounting material peaks) can be seen. The tungsten peaks also do not shift in position as opposed to what was seen with the blended samples in the first experimental section. This is likely due to the rhenium already being in solution with the optimized samples as a result of the extended milling. The blended samples, on the other hand, experienced a much larger change in the degree of homogeneity and, as such, a larger shift in the tungsten peaks as rhenium dissolved into the BCC matrix.
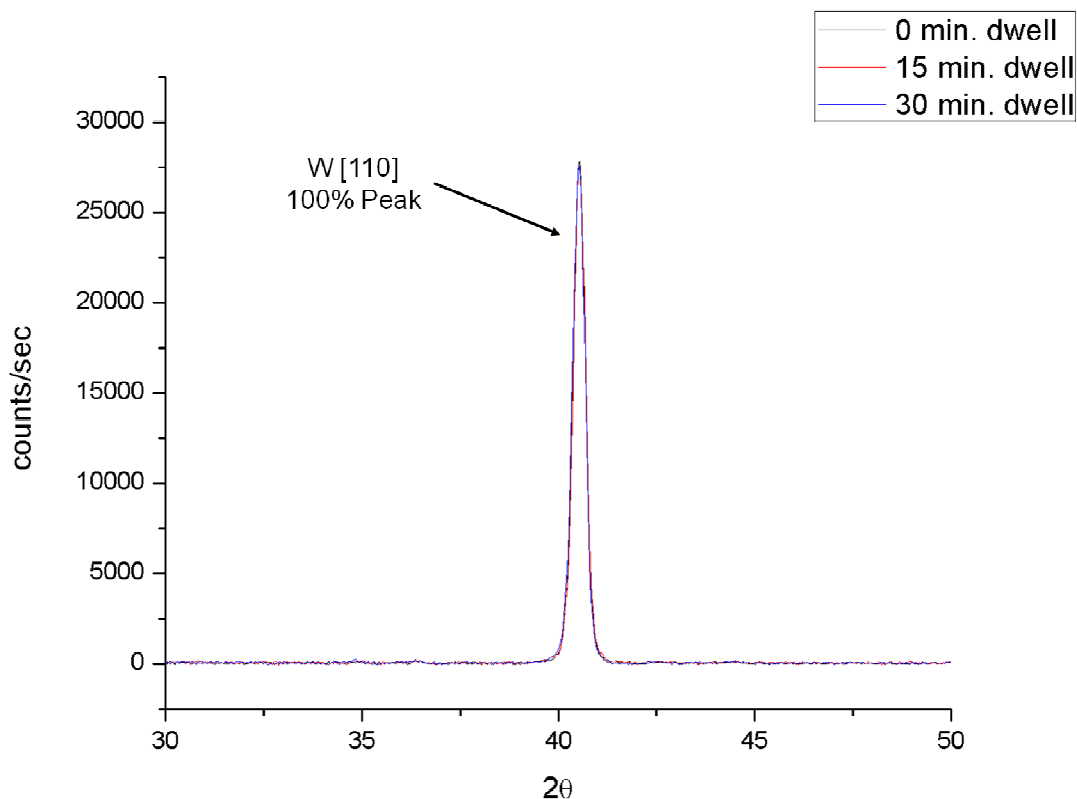
Figure 69. **XRD scan of optimized W-25 at% Re sintered at 0, 15, and 30 minutes; peaks other than tungsten at 40.5° are from mounting epoxy**

4.2.11 - Intermetallic Content

There was little to no σ-phase found in the optimized samples. The W-10 at% Re and W-25 at% Re compositional sets, as seen in Figure 70 and Figure 71, show essentially a decrease to zero area fraction. One σ-phase particle was found in one of the 30 minute dwell, W-25 at% Re samples but the remainders were phase pure after the 30 minute dwell time. As there was a large statistical variance in the image samples due to only finding σ-phase very sporadically, the concentrations are represented with box plots. The σ content for W-3 at% Re and W-6 at% Re were not included as no σ particles were

found in any images for either compositional group. These results indicate that the

intermetallic content for the W-3 at% Re and W-6 at% Re samples were eliminated prior

to reaching their dwell temperatures. The W-10 at% Re samples became homogeneous

within 15 minutes of reaching the 1800°C dwell temperature and the W-25 at% Re

samples free of σ-phase somewhere between 15-30 minutes at the dwell temperature.

This is a substantial reduction in the intermetallic content when compared to the samples

from the first experimental set.
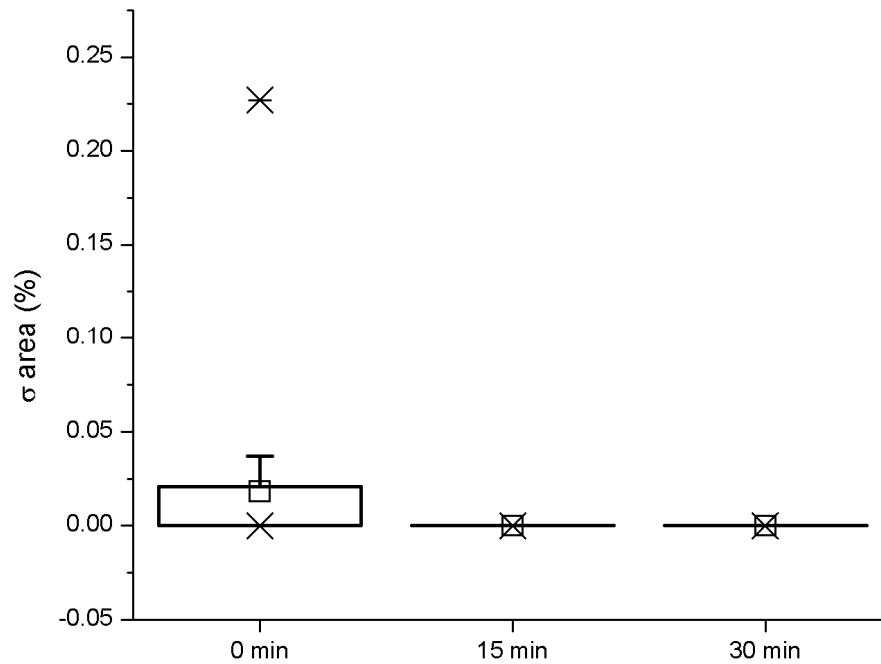
Figure 70.   Box plot of σ area percent as a function of SPS dwelt time for W-10 at% Re optimized samples
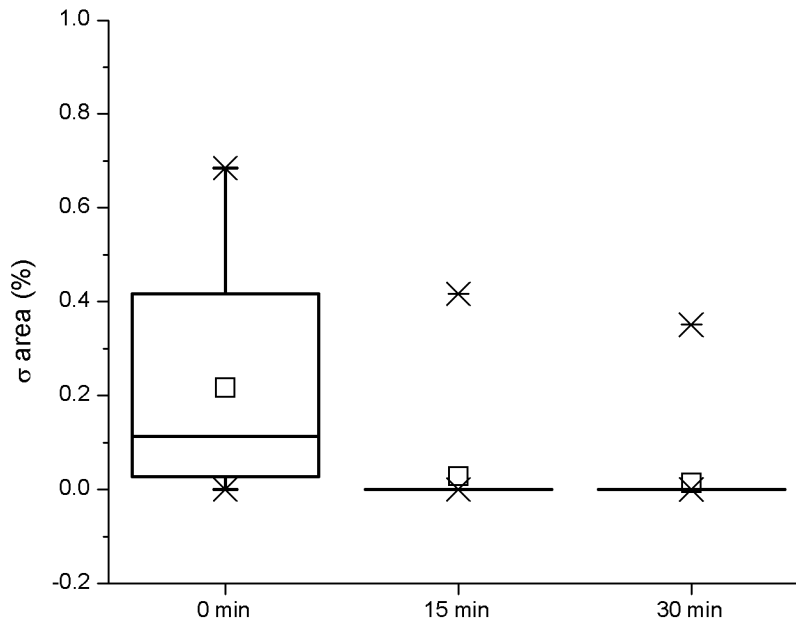
Figure 71. **Box plot of σ area percent as a function of SPS dwelt time for W-25 at% Re optimized samples**

4.2.12 - Tungsten Grain Growth

The grain sizes of the optimized samples exhibited an inverse correlation between rhenium content and grain growth as seen in Figure 72. At the 30 minute sintering dwell mark, the W-3 at% Re had reached an average grain size of approximately 8 μm while the W-25 at% Re samples were determined to be 5.5 μm. The values measured for the W-25 at% Re were only slightly larger than those found for the blended and milled sample's grain sizes determined previously.
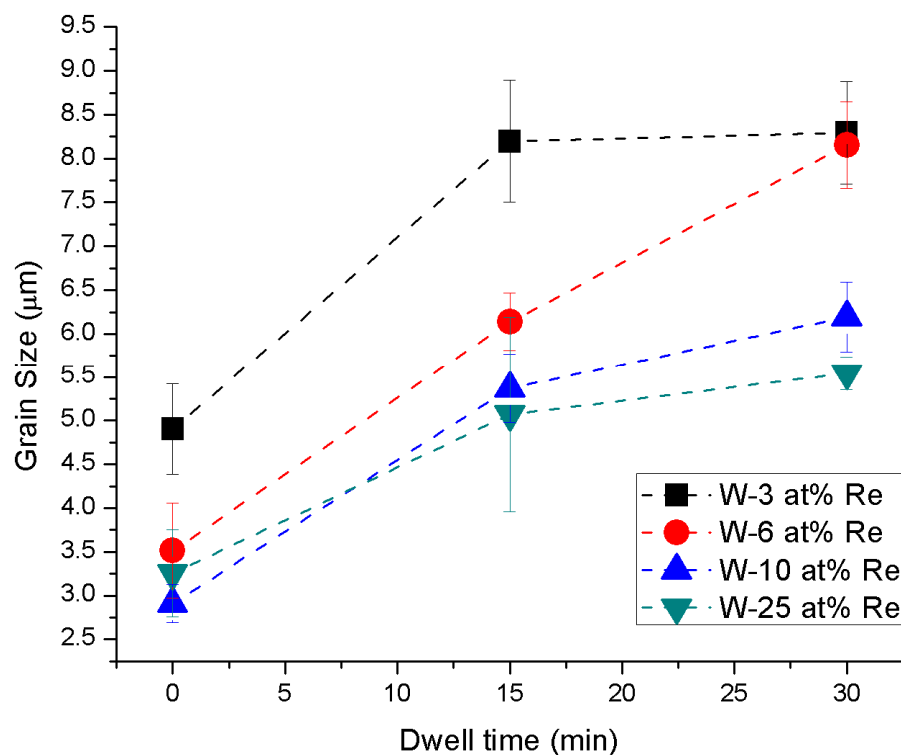
Figure 72. **Grain size as a function of SPS dwell time for optimized W-xRe samples**

For the optimized samples, it is evident that the addition of rhenium restricts the grain size of tungsten. This decrease agrees with other work in the literature, as Ramalingam and Jacobson found that the grain size dropped from 62 μm to 32 μm for pure annealed tungsten and W-25 at% Re, respectively.[48] Research by Garfinkle *et al.* also showed that the addition of rhenium would yield a substantial drop in the average grain size of tungsten.[17] The grain size of tungsten as a function of rhenium concentration for this work is shown in Figure 73 and the values found by Garfinkle in Figure 74.[17]
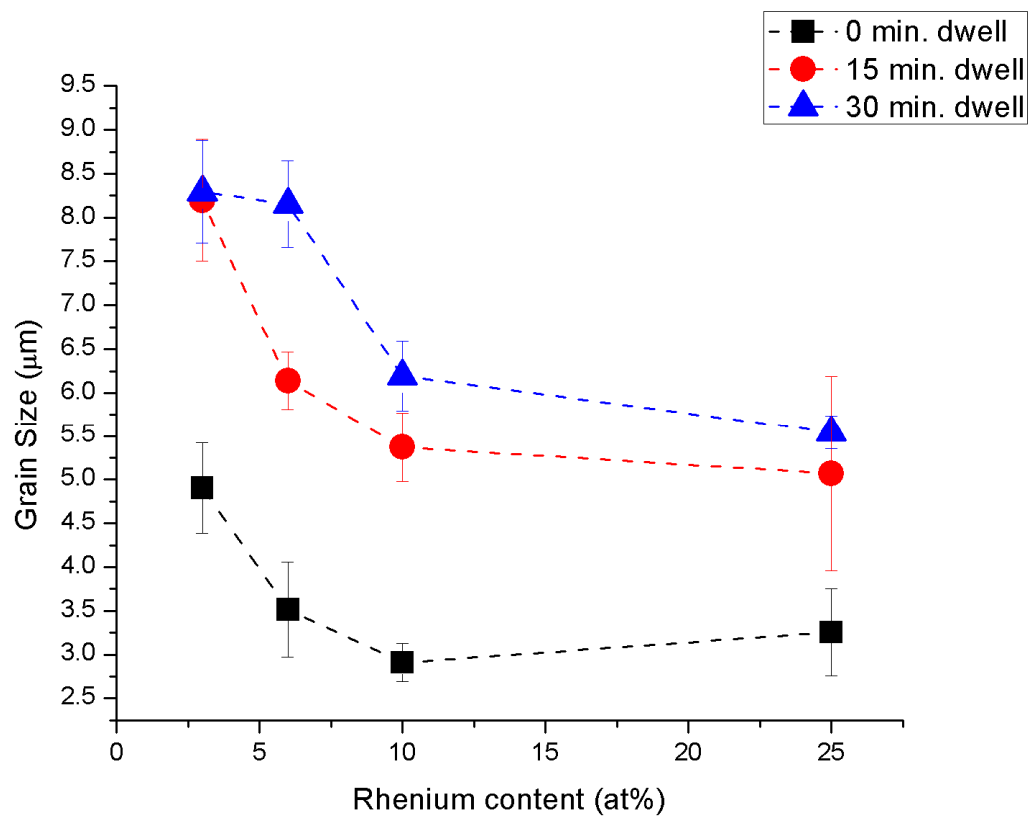
Figure 73. **Grain size as a function of rhenium content for optimized W-xRe samples**
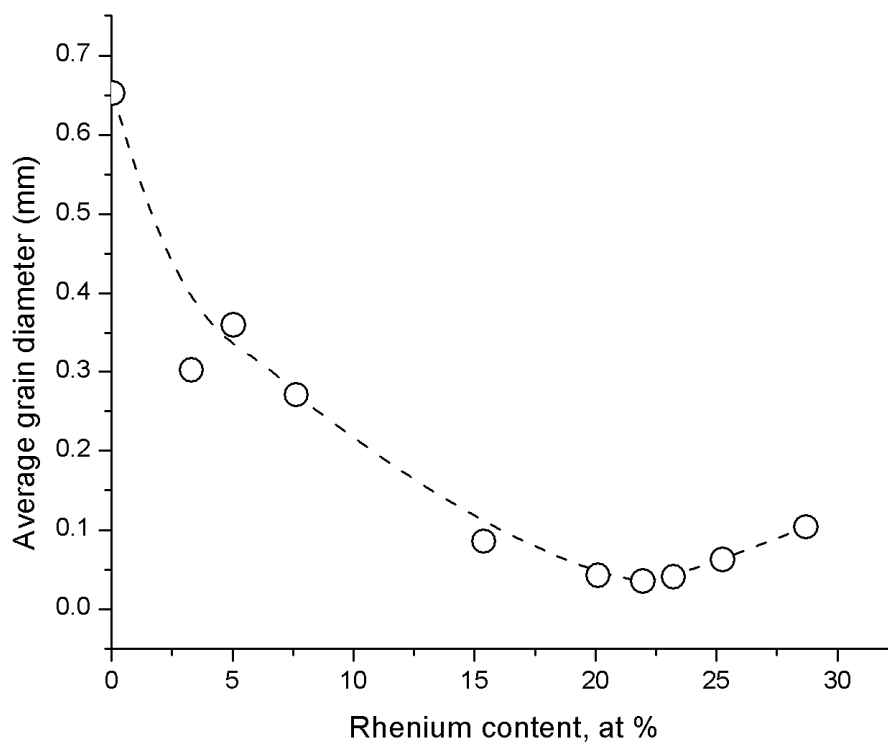
Figure 74. **Average grain diameter in fracture zone of W-Re alloys. Test temperature 3630°F (2000°C). Adapted from Garfinkle et al.[17]**

4.2.13 - Hardness Values

The micro-indentation of the optimized samples showed a direct correlation between rhenium concentration and resulting hardness. The Vicker's hardness values substantially increases with higher rhenium content (Figure 75 (left plot)) and slightly decreases with longer SPS dwell time. This difference in hardness values between the compositional sets is purely due to the rhenium content in the tungsten grains and not a Hall-Petch increase in hardness due to the rhenium effect of restricting tungsten grain growth. This distinction can be seen in Figure 75 (right plot) where the hardness values

for each compositional set was plotted as a function of grain size. It can be seen that there is an increase in hardness with higher rhenium content regardless of grain size, specifically for the W-25 at% Re samples.
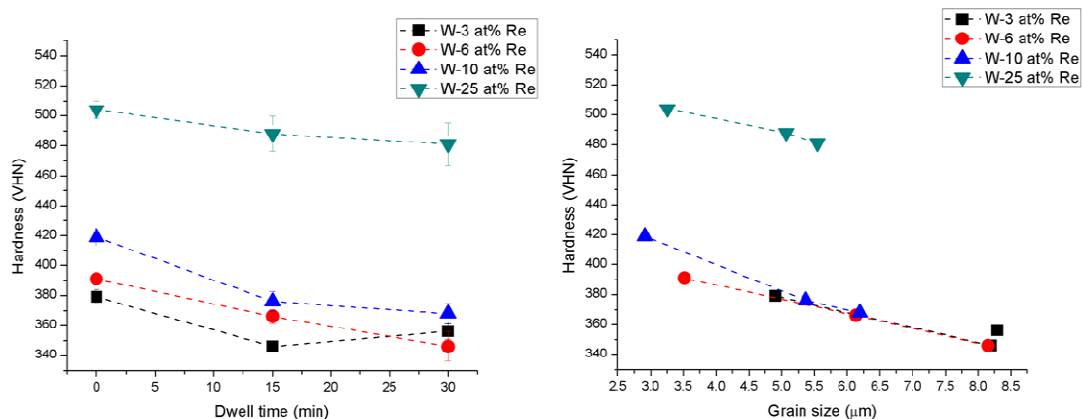
Figure 75.   Hardness (HVN) for the optimized W-xRe samples as a function of SPS dwell time (left) and grain size (right)

The hardness values agreed, to a large degree, with experimental results compiled by Klopp.[30] The plot seen in Figure 76 shows that the increase in hardness as a function of rhenium content correlates with the trend determined by Klopp. The values for this work are significantly higher than Klopp's data very likely due to Hall-Petch relationship. Klopp's samples were fabricated using arc-melted and electron beam zone melted samples, which have substantially higher grain sizes than the P/M samples made during these experiments.
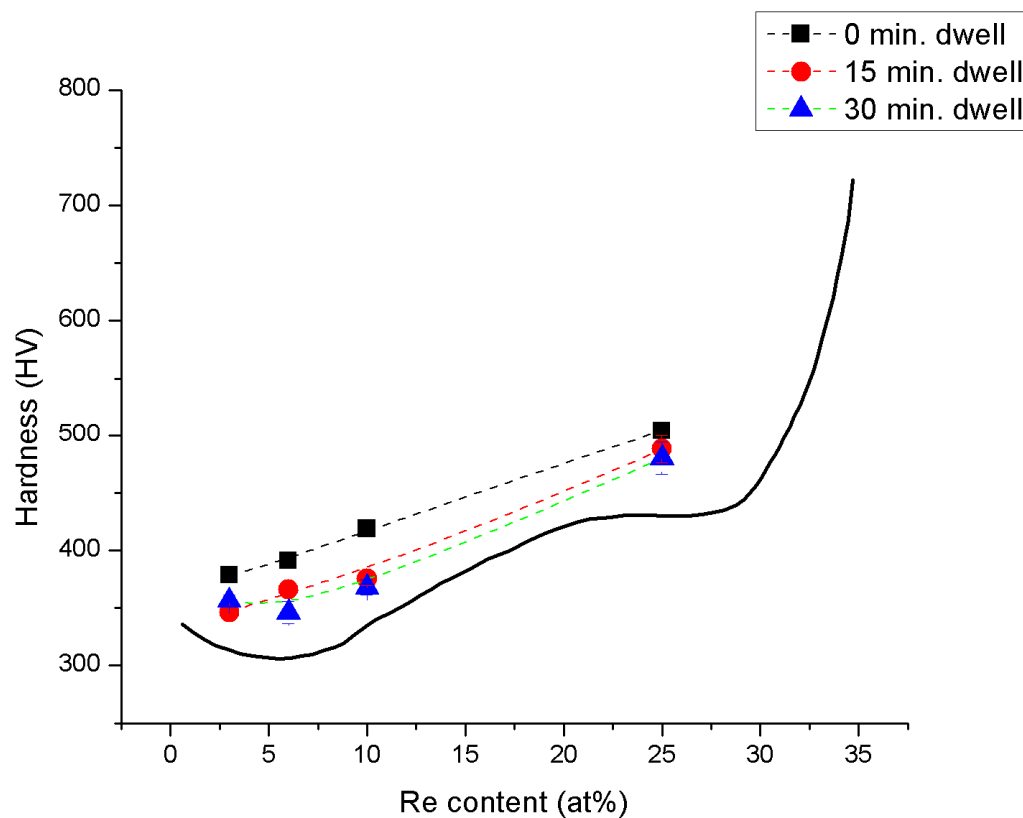
Figure 76.   Hardness (HVN) as a function of rhenium concentration with comparison to data compiled by Klopp.[30]

It should also be noted that the variation in hardness values for the optimized

samples is much less those found in the blended and milled samples from the first

experimental set (Figure 49). The larger standard deviation for the first set is likely due to

a higher inclusion of the much harder σ phase and the hardness variations at the indents at

the edges of the samples, which were affected by carbon contamination.

4.2.14 - TEM and STEM/EDS

TEM characterization of multiple grains consistently showed a BCC crystal structure. This was determined from the SAD patterns, which, when indexed, showed a BCC structure with an average of 3.15 Å lattice parameter, which corresponds quite closely with the lattice parameter for W-25 at% Re.[9] A typical bright field TEM image with associated diffraction pattern is shown in Figure 77.
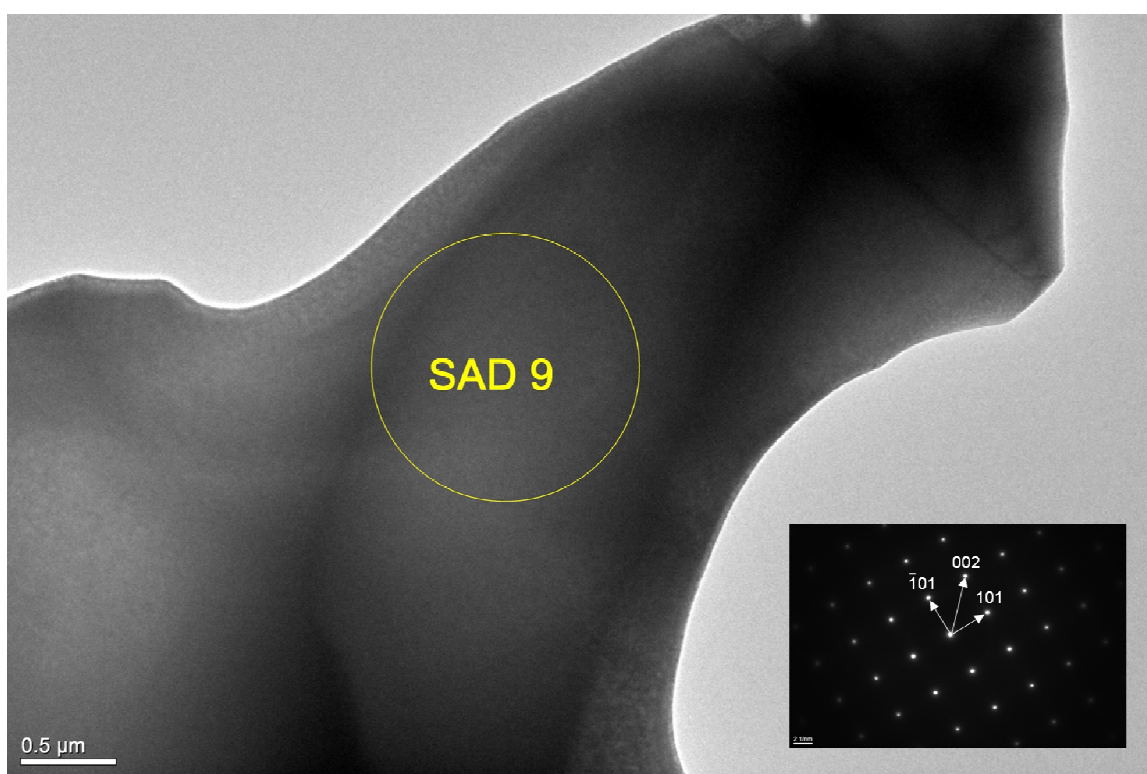
Figure 77.   Bright field TEM image with SAD insert of optimized W-25 at% Re sample (zone axis = [010])

The σ-phase characterization using SEM/BSE characterization suggested that the alloys were homogeneous within a 15 to 30 minute dwell time. For a higher magnification analysis, the grain boundaries of a W-25 at% Re sample consolidated for 30 minutes was examined for intermetallic precipitates using TEM imaging. Across the

area prepared by the FIB, there were no noticeable precipitates. Figure 78 shows two

typical grain boundaries similar to those seen in the prepared membrane.
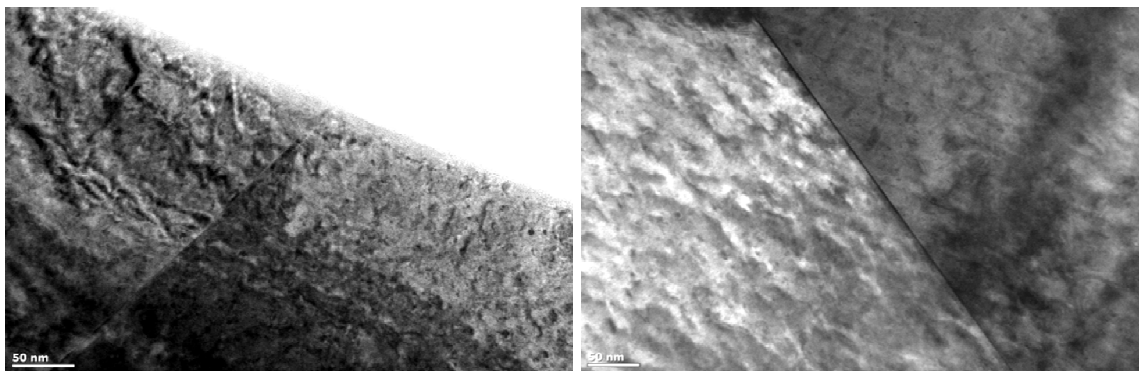
Figure 78.   TEM bright field images of optimized W-25 at% Re sample consolidated with 30 minute dwell time

STEM/EDS results showed a uniform rhenium distribution across each indexed

grain (Figure 79). The elemental analysis indicated that the rhenium concentration was

16.6 at%. The analysis also showed a Zn concentration of 8.4 at%, and, after viewing the

x-ray spectrum from the scan, it was determined that it is likely the software confused the

Re and Zn peaks, which share a degree of overlap. The combination of the concentrations

is 25.0 at%, which lends further credence to that theory. The elemental concentrations

and x-ray spectrum can be seen in Table 10 and Figure 80, respectively.
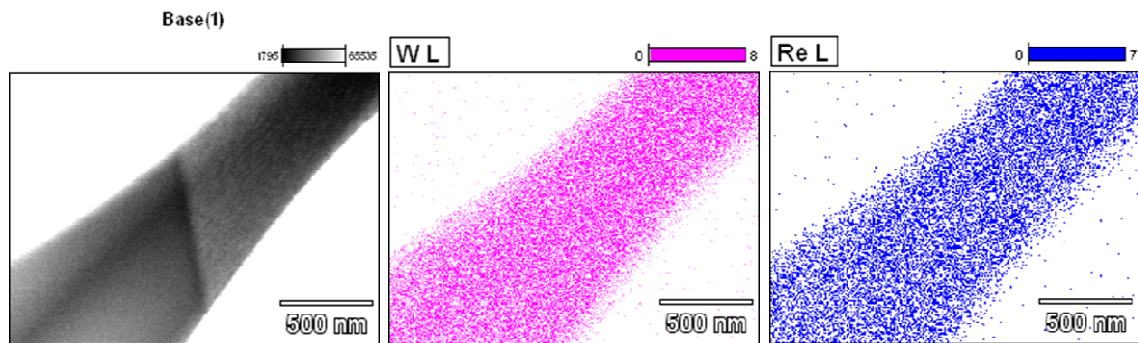
Figure 79. STEM/EDS area scans showing image, tungsten, and rhenium distributions (left to right)

Table 10. Elements found in STEM/EDS area scan

Element Line	Net Counts	Weight %	Atom %	Atom % Error
Co K	344	0.31	0.92	+/- 0.23
Zn K	3649	3.18	8.42	+/- 1.50
W L	65878	78.69	74.1	+/- 1.14
Re L	14499	17.81	16.56	+/- 1.27
Total		100	100	
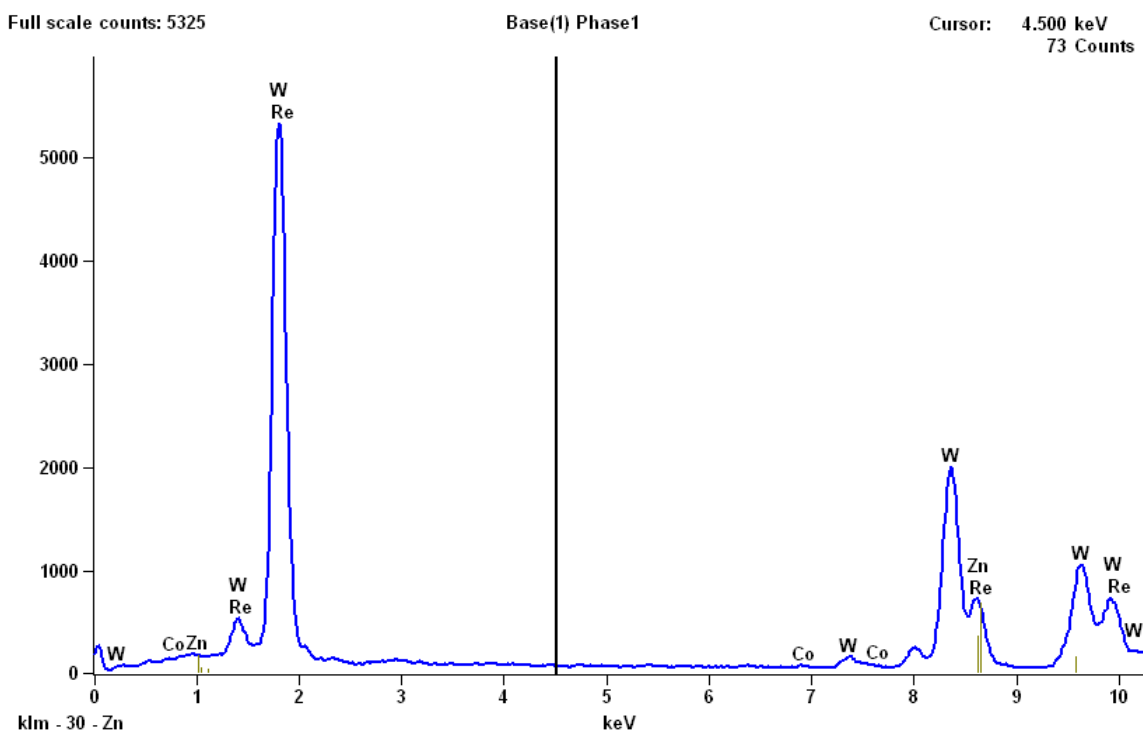
Figure 80. **X-Ray spectrum found during STEM/EDS area scan**

The scan also showed trace amounts of Co, which was also uniformly distributed throughout each grain. This contamination was initially believed to be from the binder phase in the WC-6Co milling media and vessel. However, area scans were performed on the same sample using a higher resolution EDS system than the ISIS system used to scan the optimized samples. The 191 μm x 255 μm area scan showed no Co or Zn contamination so the values measured in the TEM /EDS are likely erroneous.
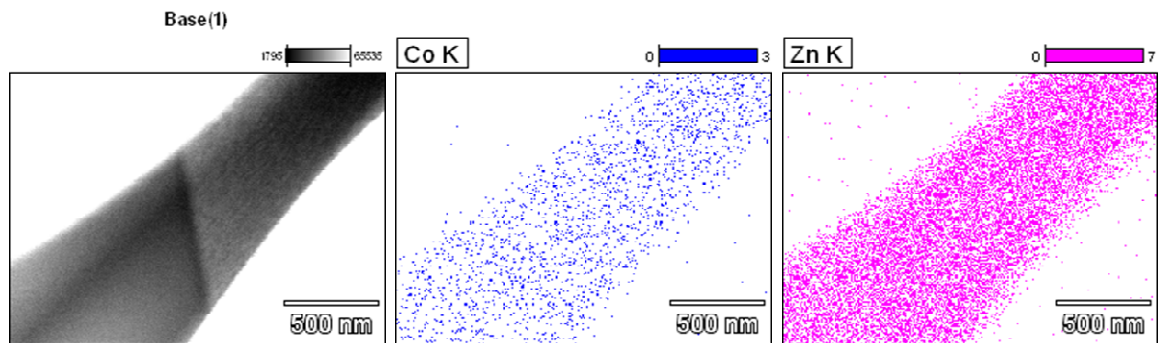
Figure 81. **STEM/EDS area scans showing image, cobalt, and zinc distributions (left to right)**

CHAPTER FIVE: CONCLUSIONS

Tungsten-rhenium alloys were successfully milled and consolidated using spark plasma sintering (SPS) with little to no intermetallic content (σ-phase), minimal grain growth, and near theoretical densities. Previous work has demonstrated that σ-phase in tungsten-rhenium alloys leads to undesirable mechanical properties.[8] This work established the relative effects of milling energy, SPS consolidation temperatures, and dwell times on the percentage of σ-phase and microstructure in alloys with rhenium contents varying from 3 to 25 at%. Processing parameters were optimized in order to yield aforementioned ideal microstructural characteristics. Detailed microstructural characterization of the powders and the sintered products lead to the following conclusions:

1. It was demonstrated that SPS can rapidly fabricate W-Re alloys with high densities and desirable microstructural features. The W-Re alloys were consolidated to near theoretical density during the ramps to the hold temperatures and consequently minimal dwell times were required to achieve full density. During the hold, the density drops and this is believed to be predominately due to the diffusional influx of carbon from the graphite paper surrounding the test coupons. This contamination can be avoided by using a refractory metal foil such as molybdenum, tantalum, or niobium, which have much smaller diffusivities in tungsten.

2. The relative effects of SPS temperature and ball milling energy on alloy characteristics, specifically σ-phase content, were determined. Both milling at higher energies and sintering at higher temperatures were found to be effective means to reduce the percentage of σ-phase content. Parameters ideal to removing σ-phase while keeping other alloy characteristics acceptable were found to be milling at 400 rpm for 30 hrs and sintering at 1800°C for 0 to 30 minutes. The optimized parameters for both milling and sintering were determined by balancing the target of having no σ-phase and minimizing grain growth, and minimizing contamination associated with milling and reactions with dies and punches. An additional consideration is maximizing the life of the SPS sintering system, which includes the graphite punches and dies, consequently low temperatures are desirable.

3. Under optimized milling and SPS conditions, as summarized in Table 7 and Table 8, tungsten-rhenium alloys were produced with no σ-phase, for all compositions investigated. In addition, all samples were produced at near theoretical density, with relatively small grain size (approximately 3-8 μm) and correspondingly with high values of hardness, yielding a superior tungsten-rhenium alloy.

4. It is suggested that heterogeneities, namely regions of high rhenium content, lead to the formation of the undesirable σ-phase. Microstructural characterization of the morphology of the tungsten-rhenium powders used in this study by SEM/BSE demonstrated that during high-energy planetary ball milling individual tungsten and rhenium crystallites both reduce the particle size and deformed and embedded crystallites into one another, often producing a fine-grained, layered powder microstructure. This powder morphology helped to lower the diffusional pathway distance for rhenium atoms,

which assisted in both sintering and homogenization of the alloys, thus enabling the ability to fabricate σ-phase free alloys. In addition, the uniquely rapid thermal ramp rates achievable in SPS restricted grain growth while high densities were achieved, leading to superior mechanical properties.

REFERENCES

[1]B. C. Allen, D. J. Maykuth, and R. I. Jaffee, "The Recrystallization and Ductile-Brittle Transition Behaviour of Tungsten," *J. Inst. Metals*, **90** [4] 120-28 (1961).

[2]K. R. Anderson, J. R. Groza, M. Fendorf, and C. J. Echer, "Surface oxide debonding in field assisted powder sintering," *Materials Science and Engineering: A*, **270** [2] 278-82 (1999).

[3]F. G. Arcella, "Interdiffusion behavior of tungsten or rhenium and Group V and VI elements and alloys of the Periodic Table," NASA Lewis Research Center report NASA CR-134526 (1974).

[4]J. S. Benjamin and T. E. Volin, "The mechanism of mechanical alloying," *MT Metallurgical Transactions,* **5** [8] 1929-34 (1974).

[5]C. Berne, M. Sluiter, Y. Kawazoe, and A. Pasturel, "Ordering effects in the Re–W and Re–Ta sigma phases," *Journal of Physics: Condensed Matter*, **13** [42] 9433 (2001).

[6]C. Berne, M. Sluiter, Y. Kawazoe, T. Hansen, and A. Pasturel, "Site occupancy in the Re-W sigma phase," *Physical Review B*, **64** [14] 144103 (2001).

[7]M. S. Boldrick, E. Yang, and C. N. J. Wagner, "The structure of amorphous and nanocrystalline W-Fe alloys prepared by high-energy ball milling," *Journal of Noncrystalline Solids*, **150** [1/3] 478 (1992).

[8]B. Bryskin, "Sigma Phase in Tungsten-Rhenium Alloys. I," *Materials and Manufacturing Processes*, **11** [1] 15 (1996).

[9]S. S. Budagovskiy, V. N. Bykov, M. I. Gavrilyuk, andV. N. Pod"yachev, "Some electron structure characteristics of W-Re solid solutions," NASA technical translation report NASA TT F-15, 214 (1973).

[10]Suryanarayana. C, "Mechanical alloying and milling," *Progress in Materials Science*, **46** [1-2] 1-184 (2001).

[11]Y. A. Chen, C. R. M. Silva, and D. M. Rowe, "Synthesis of PbTe Intermetalic Compound by Mechanical Alloying," *Materials science forum.*, **1048** [660] 347 (2010).

[12]R. L. Coble, "Initial Sintering of Alumina and Hematite," *Journal of the American Ceramic Society*, **41** [2] 55-62 (1958).

[13]V. Didoukh, A. Seifter, G. Pottlacher, and H. Jäger, "Thermophysical Properties of W–Re Alloys Above the Melting Region," *International Journal of Thermophysics*, **19** [3] 969-81 (1998).

[14]J. I. Federer and R. M. Steele, "Identification of a Beta-Tungsten Phase in Tungsten-Rhenium Alloys," *Nature*, **205** [4971] 587-88 (1965).

[15]F. H. Froes, C. R. Clark, C. Suryanarayana, E. G. Baburaj, and B. D. Bryskin, "Formation of W-Re Solid Solution by Mechanical Alloying," *Materials and Manufacturing Processes*, **13** [5] 657-70 (1998).

[16]H. P. Gao and R. H. Zee, "Effects of rhenium on creep resistance in tungsten alloys," *Journal of Materials Science Letters*, **20** [10] 885-87 (2001).

[17]M. Garfinkle, W. R. Witzke, and W. D. Klopp, "Superplasticity in tungsten-rhenium alloys," Transactions of the Metallurgical Society of AIME Vol. 245, pp. 303-308 (1969).

[18]G. A. Geach and J. E. Hughes, "The alloys of rhenium and molybdenum or with tungsten and having good high-temperature properties," Plansee Proceedings, pp. 245-253 (1955)

[19]R. M. German, "Sintering Theory and Practice." John Wiley & Sons, Inc: New York, (1996).

[20]R. M. German, "Powder metallurgy and particulate materials processing : the processes, materials, products, properties and applications." Metal Powder Industries Federation: Princeton, New Jersey, (2005).

[21]B. Gludovatz, S. Wurster, A. Hoffmann, andR. Pippan, "Fracture toughness of polycrystalline tungsten alloys," *International Journal of Refractory Metals and Hard Materials*, **28** [6] 674-78 (2010).

[22]E. Hellstern and L. Schultz, "Amorphization of transition metal Zr alloys by mechanical alloying," *Applied Physics Letters*, **48** [2] 124-26 (1986).

[23]B. Huang, L. D. Chen, andS. Q. Bai, "Bulk ultrafine binderless WC prepared by spark plasma sintering," *Scripta Materialia*, **54** [3] 441-45 (2006).

[24]D. M. Hulbert, A. Anders, J. Andersson, E. J. Lavernia, and A. K. Mukherjee, "A discussion on the absence of plasma in spark plasma sintering," *Scripta Materialia*, **60** [10] 835-38 (2009).

[25]E. Y. Ivanov, C. Suryanarayana, and B. D. Bryskin, "Synthesis of a nanocrystalline W–25 wt.% Re alloy by mechanical alloying," *Materials Science and Engineering: A*, **251** [1-2] 255-61 (1998).

[26]D. L. Johnson, "A General Model for the Intermediate Stage of Sintering," *Journal of the American Ceramic Society*, **53** [10] 574-77 (1970).

[27]D. L. Johnson and I. B. Cutler, "Diffusion Sintering: I, Initial Stage Sintering Models and Their Application to Shrinkage of Powder Compacts*," Journal of the American Ceramic Society*, **46** [11] 541-45 (1963).

[28]M. S. Kim and C. C. Koch, "Structural development during mechanical alloying of crystalline niobium and tin powders," *Journal of Applied Physics*, **62** [8] 3450-53 (1987).

[29]W. D. Kingery and M. Berg, "Study of the Initial Stages of Sintering Solids by Viscous Flow, Evaporation-Condensation, and Self-Diffusion," *Journal of Applied Physics*, **26** [10] 1205-12 (1955).

[30]W. D. Klopp, "Review of ductilizing of Group VIA elements by rhenium and other solutes," Lewis Research Center report NASA TN D-4955 (1968).

[31]W. D. Klopp and P. L. Raffo, "Effects of purity and structure on recrystallization, grain growth, ductility, tensile, and creep properties of arc-melted tungsten," Lewis Research Center report NASA TN D-2503 (1964).

[32]W. D. Klopp and W. R. Witzke, "Mechanical properties and recrystallization behavior of electron-beam-melted tungsten compared with arc-melted tungsten," Lewis Research Center report NASA TN D-3232 (1966).

[33]W. D. Klopp, W. R. Witzke, and P. L. Raffo, "Mechanical properties of dilute tungsten-rhenium alloys,"Lewis Research center report NASA TN D-3483 (1966).

[34]C. C. Koch, "Materials Synthesis by Mechanical Alloying," *Annual Review of Materials Science,* **19** [1] 121-43 (1989).

[35]E. Lassner and W. D. Schubert, "Tungsten: Properties, Chemistry, Technology of the Element, Alloys and Chemical Compounds.*"* Kluwer Academic/Plenum Publishers: New York, (1999).

[36]T. Leonhardt, "Properties of tungsten-rhenium and tungsten-rhenium with hafnium carbide," *JOM Journal of the Minerals, Metals and Materials Society,* **61** [7] 68-71 (2009).

[37]L.-G. Liu, T. Takahashi, and W. A. Bassett, "Effect of pressure and temperature on the lattice parameters of rhenium," *Journal of Physics and Chemistry of Solids,* **31**[6] 1345-51 (1970).

[38]L. Lu and M. O. Lai, "Mechanical Alloying.*"* Kluwer Academic Publishers: Boston, (1998).

[39]S. Luidold and H. Antrekowitsch, "Hydrogen as a reducing agent: State-of-the-art science and technology," *JOM Journal of the Minerals, Metals and Materials Society,* **59** [6] 20-26 (2007).

[40]S. Luidold and H. Antrekowitsch, "Hydrogen as a reducing agent: Thermodynamic possibilities," *JOM Journal of the Minerals, Metals and Materials Society,* **59** [10] 58-62 (2007).

[41]A. Luo, D. L. Jacobson, and K. S. Shin, "Solution softening mechanism of iridium and rhenium in tungsten at room temperature," *International Journal of Refractory Metals and Hard Materials,* **10** [2] 107-14 (1991).

[42]Z. Munir, U. Anselmi-Tamburini, and M. Ohyanagi, "The effect of electric field and pressure on the synthesis and consolidation of materials: A review of the spark plasma sintering method," *Journal of Materials Science,* **41** [3] 763-77 (2006).

[43]E. Oda, T. Ohtaki, A. Kuroda, H. Fujiware, K. Ameyama, and K. Yoshida, "Thermal Stability of Nano Grain Structure Tungsten Prepared by SPD-PM Process," *Advanced Materials Research,* **15-17** 564-69 (2007).

[44]E. A. Olevsky, S. Kandukuri, and L. Froyen, "Consolidation enhancement in spark-plasma sintering: Impact of high heating rates," *Journal of Applied Physics,* **102** [11] 114913-13-12 (2007).

[45]R. Orrù, R. Licheri, A. M. Locci, A. Cincotti, and G. Cao, "Consolidation/synthesis of materials by electric current activated/assisted sintering," *Materials Science and Engineering: R: Reports,* **63** [4-6] 127-287 (2009).

[46]S. R.L, "Comparative creep-rupture properties of tungsten-25% rhenium consolidated by arc-melting and powder-metallurgy techniques," *Journal of the Less Common Metals,* **24** [2] 173-82 (1971).

[47]P. L. Raffo and W. R. Witzke, "Creep of powder metallurgy rhenium at 0.43 to 0.72 T_m," *Transactions of the Metallurgical Society of AIME,* Vol. 245:pp. 889-90 (1969).

[48]M. L. Ramalingam and D. L. Jacobson, "Elevated temperature softening of progressively annealed and sintered W-Re alloys," *Journal of the Less Common Metals,* **123** [1-2] 153-67 (1986).

[49]J. L. Ratliff, D. J. Maykuth, H. R. Ogden, and R. I. Jaffee, "Tungsten sheet alloys with improved low-temperature ductility," *Transactions of the Metallurgical Society of AIME,* Vol: 230, pp: 490-500 (1964).

[50]P. Schade, "100 years of doped tungsten wire," *International Journal of Refractory Metals and Hard Materials,* **28** [6] 648-60 (2010).

[51]L. Schultz, J. Wecker, and E. Hellstern, "Formation and properties of NdFeB prepared by mechanical alloying and solid-state reaction," *Journal of Applied Physics,* **61** [8] 3583-85 (1987).

[52]D. W. Smith and R. F. Hehemann, "Kinetics of alloy formation in sintered tungsten-rhenium powder compacts," *Transactions of the Metallurgical Society of AIME*, Vol: 236, pp: 506-12 (1966).

[53]E. Sutherland and W. Klopp, "Observations of properties of sintered wrought tungsten sheet at very high temperatures ," Lewis Research Center report NASA D-1310, (1963).

[54]G. Wang, S. Campbell, A. Calka, and W. Kaczmarek, "Synthesis and structural evolution of tungsten carbide prepared by ball milling," *Journal of Materials Science,* **32** [6] 1461-67 (1997).

[55]J. Webb (2011).

[56]J. E. White and M. M. Jurkowitz, "Hot pressing of tungsten powder," *Met. Soc. Conf.,*Vol. 30: pp: 291-4, (1966)

[57]C. Wilson, "Order in binary sigma-phases," *Acta Crystallographica,* **16** [8] 724-30 (1963).

[58]W. R. Witzke, E. C. Sutherland, G. K. Watson, "Preliminary investigation of melting, extruding, and mechanical properties of electron-beam-melted tungsten." Lewis Research Center report NASA TN D-1707 (1963).

[59]R. H. Zee and M. F. Rose, "High temperature materials technology research for advanced thermionic systems. Space Powder Institute report DE-FG03-93SF19645-94 (1998).